Arbeitsbericht NAB 19-25

Dating Quaternary Terraces in Northern Switzerland with Cosmogenic Nuclides

February 2020

National Cooperative
for the Disposal of
Radioactive Waste

Hardstrasse 73
P.O. Box 280
5430 Wettingen
Switzerland
Tel. +41 56 437 11 11

www.nagra.ch

nagra.

Arbeitsbericht NAB 19-25

Dating Quaternary Terraces in Northern Switzerland with Cosmogenic Nuclides

February 2020

R. Grischott[1], F. Kober[2], S. Ivy-Ochs[1], K. Hippe[1], M. Lupker[3], E. Bros[1], C. Maden[3], M. Christl[1] & Ch. Vockenhuber[1]

1) Labor für Ionenstrahlphysik, ETH Zürich
2) Nagra
3) Departement für Erdwissenschaften, ETH Zürich

KEYWORDS

Quaternary, dating, Deckenschotter, gravel units, cosmogenic nuclides, isochron burial dating

National Cooperative for the Disposal of Radioactive Waste

Hardstrasse 73
P.O. Box 280
5430 Wettingen
Switzerland
Tel. +41 56 437 11 11

www.nagra.ch

Nagra Arbeitsberichte ("Working Reports") present the results of work in progress that have not necessarily been subject to a comprehensive review. They are intended to provide rapid dissemination of current information.

Abstract

This report consists of three main parts. The first part introduces the topic of dating the Deckenschotter in Northern Switzerland, particularly using cosmogenic nuclides, and addresses the related motivation and research questions. In short, the aim is to better constrain the existing, poorly developed chronologies of the Deckenschotter and to improve the understanding of landscape evolution during the Quaternary.

The second part contains an assessment of depth profile dating of the Deckenschotter using Terrestrial Cosmogenic Nuclides (TCN). An in-depth literature review provides the required background to the depth profile dating method. A recently introduced modelling algorithm, the Hidy code, was used for systematic tests of ^{10}Be depth profiles, tracking their evolution over time. For this purpose, crucial parameters such as profile erosion rates were taken from a recently published paper which investigated the Deckenschotter from the Stadlerberg site in the Swiss foreland. Additionally, the Stadlerberg data from the paper itself were thoroughly tested using the algorithm and other tools. Altogether, these tests show that ^{10}Be depth profiles quickly achieve steady state within 0.2 – 0.3 Myr for erosion rates of 5 cm/kyr. Without using a constraint such as total erosion or independent age, absolute ages cannot be modelled, and only minimum depositional ages can be obtained. Consequently, it is not possible to determine a depositional age with any degree of confidence using the published ^{10}Be data for the Stadlerberg site.

The third part consists of a study of dating the Deckenschotter using the ^{26}Al/^{10}Be TCN burial method approach. Two methods were used for this report: true/simple and isochron burial dating. Methodological as well as technical aspects are described, explaining the challenges of measuring low nuclide concentrations, particularly ^{26}Al, in Alpine samples. Available codes for age modelling of ^{26}Al/^{10}Be data are then described and discussed.

The sampling sites were selected on the basis of an outcrop catalogue map and applied selection criteria. Two sites belonging to the Höhere Deckenschotter, Tromsberg (Dürn-Gländ) and Feusi (Egg) and one site related to the Tiefere Deckenschotter, Iberig, were sampled. Two sites related to the Hochterrasse, namely Beringen and the Glatt Valley, were additionally sampled. In total, 41 ^{26}Al/^{10}Be data are presented. Modelled ages yield the most likely reliable ages ranging from 0.95 – 1.3 Myr for the Höhere Deckenschotter at the Feusi site. The dataset for Tromsberg (HDS) indicates a presumed age range of ~ 1.25 – 1.55 Myr, whereas the TDS site at Iberig yielded an age of ~ 0.65 – 0.95 Myr. However, both datasets require more data to consolidate the regression analysis. The datasets for the Hochterrasse sites Beringen and Glatt Valley cannot be used to determine an age due to data scatter. Relevant challenges in terms of methodology, measuring techniques and parameters used for age calculation are discussed. Finally, a landscape evolution model based on the cosmogenic data is presented. In this, the measured ^{26}Al/^{10}Be concentrations at the Feusi site (HDS) that are relatively and significantly higher than at the Tromsberg and Iberig sites are explained as having originated from one of the first advances of Alpine glaciers into the Swiss foreland at the beginning of the Mid-Pleistocene Transition around 1 – 1.3 Myr. Several glaciations that followed caused a drop in the ^{26}Al/^{10}Be concentrations as observed at the Tromsberg and Iberig sites. However, the dataset needs to be expanded to further constrain this model.

Besides the established chronologies, the working principles of the method as well the weaknesses and challenges are widely discussed. Applying ^{26}Al/^{10}Be isochron burial to samples originating from a glacial landscape will require more systematic tests and improved measuring techniques. Nonetheless, geomorphic processes such as glacial erosion representing the source of the Deckenschotter sediments are the cause of the low nuclide concentrations measured. Thus, achieving a solid database with a representative spread in the data and a well-defined regression analysis can only be obtained through the analysis of additional samples.

Table of Contents

List of Tables

List of Figures

1 Introduction

1.1 Motivation

During the Quaternary period, the Northern Alpine foreland was glaciated several times and underwent a multi-stage landscape development through various stages of incision, erosion and deposition of glaciofluvial sediments (Ivy-Ochs et al. 2004, Penck & Brückner 1909, Preusser et al. 2011, Preusser & Schlüchter 2004, Schlüchter 1989). While the Last Glacial Maximum (LGM) is well documented (Ivy-Ochs 2015, Ivy-Ochs et al. 2008), earlier glaciations, and especially early Quaternary glaciations prior to the Mid-Pleistocene Transition (MPT, 0.7 – 1.2 Myr, cf. Ruddiman et al. (1989) and references therein) are only poorly dated. Furthermore, the correlation of the landscape elements such as gravel terraces across the Alpine foreland remains controversial (Doppler et al. 2011, Ellwanger et al. 2011, Kuhlemann & Rahn 2013). Currently, no consistent model exists for the temporal relationship with potentially similar deposits in Switzerland, Germany and Austria.

The accurate quantification of the landscape evolution, particularly for the Swiss Alpine foreland, is not only of scientific interest for the Quaternary community but is also helpful in assessing the long-term safety of deep geological repositories for radioactive waste planned by the Swiss National Cooperative for the Disposal of Radioactive Waste (Nagra). Accordingly, the depositional ages of these spatially extensive sediment bodies and paleosurfaces and the subsequent incision are crucial for establishing incision and erosion scenarios, river drainage patterns and related base-level reconstructions (Nagra 2014).

1.2 Characteristics of the Swiss Deckenschotter

The Deckenschotter units (Höhere and Tiefere Deckenschotter, HDS/TDS) as well as the terrace units (Hoch- and Niederterrasse, HT/NT) have been investigated since the early stages of the modern Alpine Quaternary geomorphology (Penck & Brückner 1909) in order to understand past glaciations of the Alps. They have been linked genetically to glaciations by field evidence such as interbedded tills, far-travelled erratic boulders and secondary cements (derived from glacier milk precipitation) (Graf 1993 and references therein). The sedimentary stratigraphy of the Swiss Deckenschotter and terrace units has been described as consisting of massive to stratified, often cross-bedded, sandy glaciofluvial gravels with prominent block layers. Interbedded sand and silt lenses are typical whereas diamicts are scarce (Fig. 1). The lithology of the components, such as crystalline and sedimentary rocks, is typical for the Central Alps. Clasts reworked from the Molasse such as sandstones, red granites and various other crystalline rocks from the Central Alps are rather rare. The glaciofluvial and diamictic layers found in the Deckenschotter have commonly been interpreted to be indirectly or directly influenced by the presence of glaciers in the foreland. Deckenschotter are spatially extensive sediment bodies and represent paleosurfaces in the form of high elevated terraces and plateaus in the Northern Swiss foreland. These hills are explained as an inverse topography where the oldest units are the highest and the younger units are relatively lower. The Höhere Deckenschotter, Tiefere Deckenschotter and Hoch- and Niederterrasse units were found to cluster along similar elevations (Graf 1993) and were thus defined based on their topographical position and morphostratigraphy (Fig. 1 and 2). The difference in elevation suggests that the Deckenschotter and terrace units are separated from each other by distinct periods of significant incision. The mechanisms causing these major incision events in the Northern Alpine foreland are not yet entirely clear. The incision can mainly be explained by fluvial incision related to uplift and/or base level fall, with glaciations reaching the foreland as an additional factor.

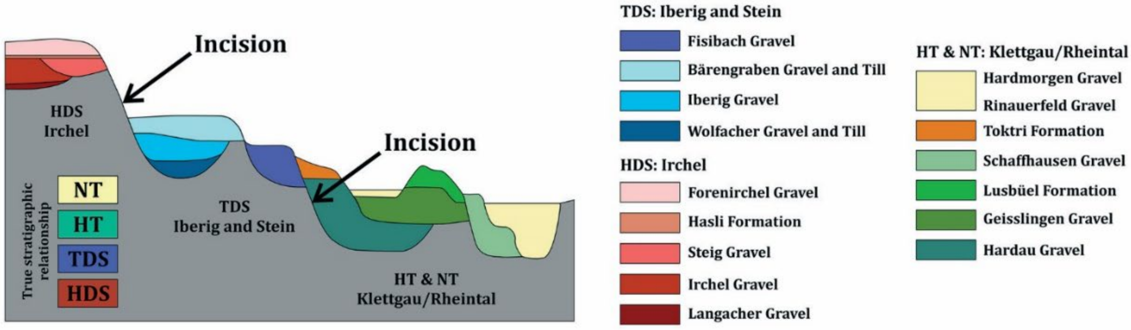

Fig. 1: Schematic stratigraphy of the Quaternary deposits of the Northern Alpine foreland

After Graf & Müller (1999). Figure taken from Akçar et al. (2014). The sketch illustrates the multiple phases of incision and deposition and the complex stratigraphic depositional sediment bodies.

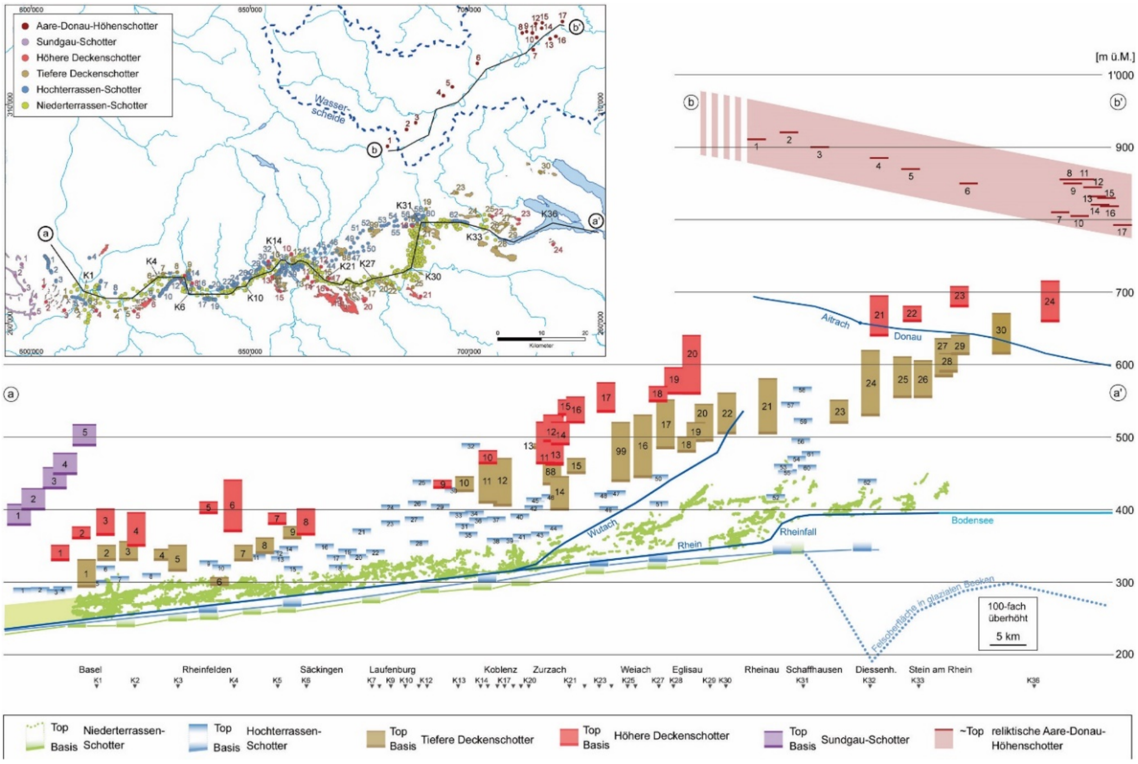

Fig. 2: Distribution and genetic relationship of the terrace units of HDS, TDS, HT and NT in Northern Switzerland along the present-day Rhine river

Schnellmann et al. (2014)

1.3 Previous dating approaches

Understanding the timing of gravel accumulation and terrace formation is crucial to understanding the extents and occurrences of past glaciations, fluvial incision events and landscape evolution in general. Therefore, absolute dating of these sediments recording the Quaternary history has been a goal for more than the last 25 years (cf. Graf 1993). However, their absolute dating has been hampered due to the lack of appropriate dating material and/or the availability and range of existing dating methods. Inference from their landscape positions and climatic reconstructions (Fig. 3) suggest that the HT, TDS and HDS are older than Marine Isotope Stage 6 (MIS) where most absolute dating techniques are at their limits (radiocarbon < 50 ka, luminescence techniques, such as OSL mostly < 200 ka; Lowick et al. (2015).

For a long time, dating the Deckenschotter units was limited to paleomagnetic (Bolliger et al. 1996, Graf & Müller 1999) and biostratigraphic (Bolliger et al. 1996) methods at very limited sites (e.g. Irchel), with the former delivering results of only limited use. These investigations reported mostly inversely polarised Matuyama epoch magnetic signals (suggesting > 780 ka) or yielded a biostratigraphic age of 2.6 – 1.8 Ma (mammalian zone 17, MN17; Bolliger et al. 1996), respectively, for the HDS. TDS or HT are still correlated only by relative means and by inferred correlation to MIS or stratigraphic interpretations (Fig. 3; Kuhlemann & Rahn 2013 and references therein). Recently, the cosmogenic nuclide dating technique expanded to terrace deposits and has been applied to Deckenschotter units in Germany (Häuselmann et al. 2007) and Northern Switzerland (Akçar et al. 2014, Akçar et al. 2017, Claude et al. 2017). In these cases, the depth-profile dating technique was applied (Hidy et al. 2010). In Section 2.1 "Assessment of ^{10}Be depth profiles for dating Deckenschotter", the development and limits of the method are explained in detail. In short, for fast eroding surfaces, e.g. in the Swiss foreland, the rapid achievement of a steady state in the depth profiles results in minimum age for terrace abandonment of a few 100 kyr for supposedly old sediments. Thus, the depth profile ages presented in those papers are not considered to be representative and are not listed here (for details see Section 2.1 and following).

Simultaneously, the isochron burial dating technique (using the ^{10}Be/^{26}Al pair, Balco & Rovey 2008) has been applied to the Deckenschotter units at the Siglistorf (Akçar et al. 2017) and Irchel sites (Claude et al. 2019). The presented age range of 1.5 ± 0.2 Myr for Höhere Deckenschotter at the Siglistorf site and 0.9 ± 0.4 Myr for the Höhere Deckenschotter at the Irchel site is promising but awaits confirmation from other sites. Furthermore, the choice of the right parameters for the age calculation (the initial production ratio) is very sensitive for the calculated deposition ages and therefore requires careful consideration. Apart from this, dating terrace units such as the TDS or HT is awaiting the test of being dated using cosmogenic nuclides. This information would substantially broaden the understanding of the timing and dynamics of the Quaternary landscape of Northern Switzerland.

In this study, working with depth profiles was abandoned due to the methodological problems listed (see Section 2.1). Instead, isochron burial dating was selected to date the Deckenschotter as well as the Hochterrasse (see Section 3.2). This report documents the full methodology of isochron burial dating with sampling, extraction and measurement of nuclides, age modelling and interpretation of obtained ages (Section 3.3). Sampling was performed at five sites (Chapter 4) and the data (Chapter 5) were analysed and interpreted in terms of chronostratigraphy and landscape evolution (Chapter 6).

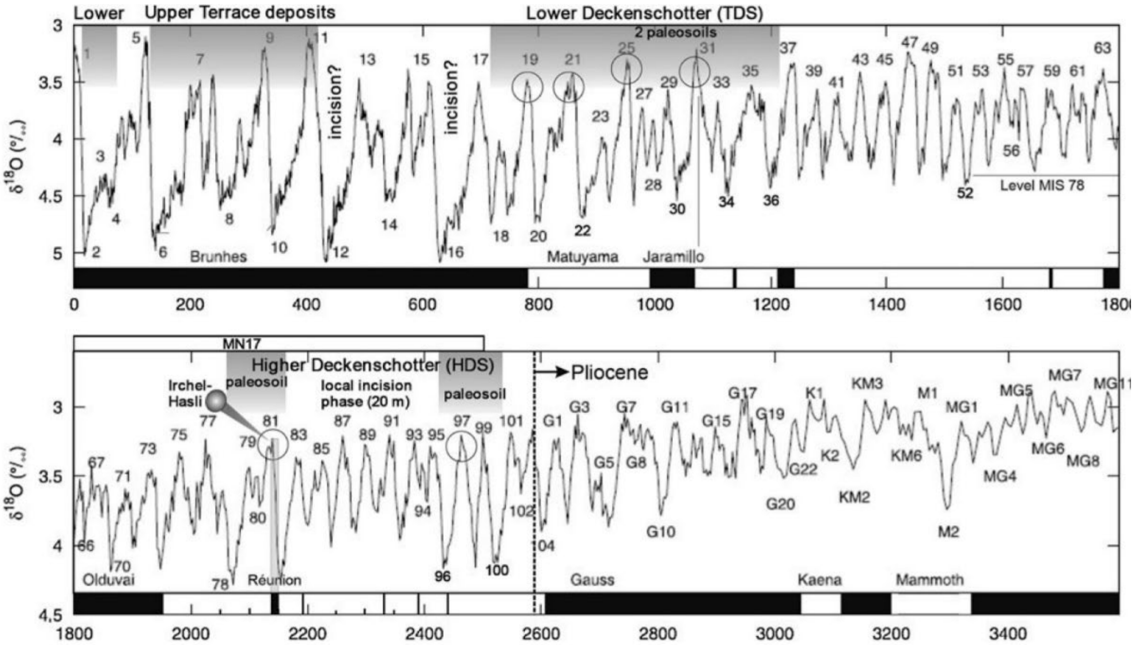

Fig. 3: Global marine oxygen isotope record of the last 3.5 Ma and tentative age assignments of Höhere Deckenschotter (HDS), Tiefere Deckenschotter (TDS), and Hochterrasse (HT) and Niederterrasse (NT) deposits in Northern Switzerland

Kuhlemann & Rahn (2013)

2 Assessment of Terrestrial Cosmogenic Nuclide (TCN) depth profiles for dating Deckenschotter

In this sub-section, the potential for dating glaciofluvial terraces (beyond the reach of OSL dating methods for sediments from Northern Switzerland, > 200 kyr) with cosmogenic depth profiles (in particular ^{10}Be) is evaluated and assessed using both synthetic and publicly accessible data. First, a brief introduction to cosmogenic nuclides and their production at or near the Earth's surface is given, followed by a short literature review of field and methodological studies taking those most relevant to our setting, i.e. similar climatic, morphological and geological conditions and various methodological variations. This selection of papers represents only a minority of all published material dealing with depth profiles. However, they represent major advances in the method which are required to demonstrate the state of the art. The most important modelling codes for depth profiles are also presented in the review. Second, the evolution of cosmogenic depth profiles through time is illustrated using synthetic profiles, followed by a detailed discussion of field data from a recently published study in the area of interest. Finally, lessons learned from this assessment are presented.

2.1 Overview of Terrestrial Cosmogenic Nuclides (TCN)

Terrestrial Cosmogenic Nuclides (TCN, e.g. ^{10}Be and ^{26}Al) are produced through spallation reactions and muon capture (Fig. 4) in minerals of rocks and sediment at or near the Earth's surface (Gosse & Phillips 2001). ^{10}Be and ^{26}Al can be applied to determine the deposition age of a geological layer using either their accumulation (depth-profile dating) or their radioactive decay (burial dating) (Dehnert & Schlüchter 2008, Granger & Muzikar 2001, Granger & Smith 2000).

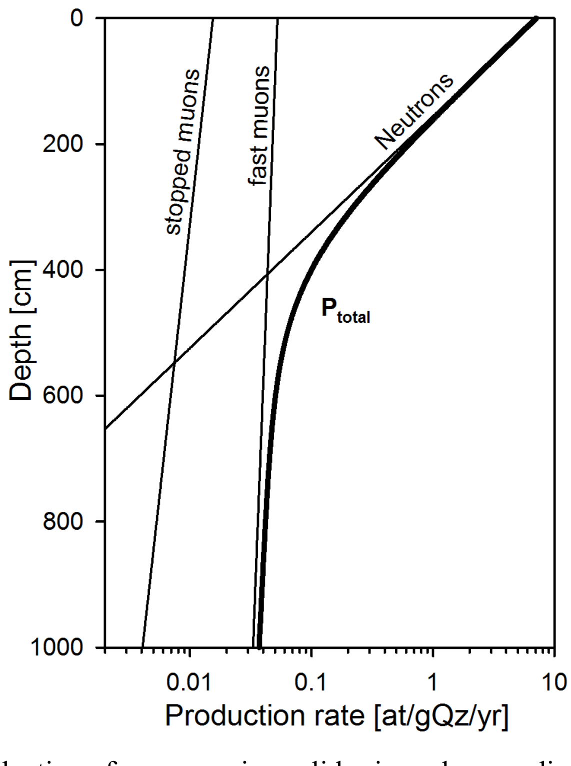

Fig. 4: In-situ production of cosmogenic nuclides in rocks or sediments along depth

The nuclide concentration of depth profiles at a certain time, depth and under a specific erosion rate can be mathematically described by the following equation:

$$N_{x,\varepsilon,t} = \frac{P_{sp} \cdot exp\,(-\frac{x}{L_n})\,(1 - exp(-\,t(\frac{\varepsilon}{L_n} + \lambda)}{\frac{\varepsilon}{L_n} + \lambda}$$

$$+ \frac{P_{\mu slow} \cdot exp\,(-\frac{x}{L_{\mu slow}})\,(1 - exp(-\,t(\frac{\varepsilon}{L_{\mu slow}} + \lambda)}{\frac{\varepsilon}{L_{\mu slow}} + \lambda}$$

$$+ \frac{P_{\mu fast} \cdot exp\,(-\frac{x}{L_{\mu fast}})\,(1 - exp(-\,t(\frac{\varepsilon}{L_{\mu fast}} + \lambda)}{\frac{\varepsilon}{L_{\mu fast}} + \lambda}$$

$$+ N_0 \cdot exp(-\lambda \cdot t) \qquad \text{Eq. (1)}$$

Where N(x,ε,t) is the nuclide concentration of depth x (g/cm^2), erosion rate ε (g/cm^2/y) and exposure time (y). P_{sp}, $P_{\mu slow}$ and $P_{\mu fast}$ and L_{sp}, $L_{\mu slow}$ and $L_{\mu fast}$ are the production rates and attenuation lengths of neutrons, slow muons and fast muons, respectively.

2.2 Literature review on TCN depth profiles for dating of terraces

Terraces in a fluvial environment can bear two different types of age information; the first from deposition of sediments during aggradation and the second from the abandonment of the terrace when the river starts to incise. The abandonment of terraces has traditionally been dated by sampling large amounts of clasts lying on the surface of the terrace body (e.g. Cerling & Craig 1994). However, nuclides in the clasts are not only produced after deposition on the terrace itself but are also inherited from the accumulation of nuclides in the sampled clasts prior to deposition. Therefore, at best, only maximum age estimates were possible. Anderson et al. (1996) presented a new method for estimating the inheritance of the sediments in the terrace. The authors proposed to take a sample of amalgamated clasts (n = 30) from the subsurface of the terrace and to compare this significantly lower – due to being partly shielded – concentration with the higher sample concentration at the surface. By accounting for the depth and density of the soil, it is possible to estimate the mean inheritance. Knowing the mean inheritance is crucial for calculating the effective exposure age of the terrace surface. Closely related to the study of Anderson et al. (1996), Repka et al. (1997) supplemented the newly introduced method of depth profiling with a set of numerical simulations. The latter mathematically traced the nuclide concentration of a sample starting with the production of nuclides on a hillslope (build-up of inheritance), followed by fluvial transport to its final deposition area and subsequent production since then.

In 2004, Siame et al. (2004) proposed a depth profile approach where the ^{10}Be concentrations exponentially decrease due to spallogenic production down to a shallow depth and muogenic production at greater depths (slow and fast muons). The expected decrease with depth of the measured ^{10}Be concentrations has been modelled using a chi-squared inversion method in order to constrain the exposure history of the alluvial sediments. Through this data-fitting method, the difference between the measured concentration and the computed concentrations was minimised and the corresponding best-fit values for exposure age and erosion rate were reported. In other words, the chi-squared method provides a quantitative estimation of the model's "goodness of fit". The closer chi-squared is to zero, the better the data fit the model. The minimum chi-squared value represents a minimum for a given pair of depositional age and erosion rate solution.

In order to work with cosmogenic depth profiles, the following assumptions were required: a simple cosmogenic exposure history, constant inheritance along depth, constant erosion of the top surface (no episodic events), no aggradation (e.g. by aeolian processes), exponential decrease of nuclide concentrations along depth (no vertical mixing) and constant production (e.g. no changes in the Earth's magnetic field). Siame et al. (2004) correctly recognised that, for the constant maximum erosion rate, an interval from a minimum age to infinite ages is plotted. They concluded that this pattern should be interpreted as a visualisation of the so-called steady state equilibrium where the production of nuclides is equal to the loss of nuclides due to erosion and decay. Consequently, the measured ^{10}Be concentrations of saturated profiles can only be related to a constant, maximum erosion rate and a minimum age.

In the proposed model of Siame et al. (2004), the analytical uncertainties were not accounted for, which was also the case for the improved chi-squared Monte Carlo modelling approach of Braucher et al. (2009). The latter additionally reported a mathematical proof for the unique determination of both exposure age and erosion rate by a single nuclide depth profile by accounting for both spallogenic and muogenic production pathways. The most important requirement is therefore that there is only a convergence of the profile to a unique solution of exposure age, erosion rate and inheritance when the profile is not yet in equilibrium with the landscape, which means that the profile is not saturated for a constant, maximum erosion rate of the profile. Furthermore, the uniqueness comes from the ability to characterise both production pathways at the so-called "knee" of the profile (Fig. 4) which however is often impossible to do when working with real geological data due to practical or technical problems such as low measurement uncertainties, negligible scatter in the dataset, detailed knowledge of the evolution of density (for accurate characterisation of the production pathways), constant erosion, etc. Furthermore, model and measurement errors together with a scarcity of measured data introduce considerable uncertainty in the optimised model parameters.

Hidy et al. (2010) provide an easily understandable and freely accessible depth profile simulator with a user-friendly graphical interface based on a Matlab code (Fig. 5). To assess model parameter uncertainty, Hidy et al. (2010) performed plain Monte Carlo sampling from the pre-specified prior parameter distributions (Tab. 1), ranking the resulting solutions according to fitting performance (chi-squared inversion) and retaining a certain percentage (typically 1 or 5 %) of the best performing solutions to compute parameter uncertainty estimates. The programme allows the incorporation of site-specific knowledge to approximate the most probable values for the exposure age of a depth profile, (constant) erosion rate and inheritance, while providing a rigorous treatment of their uncertainties based on a set of samples (Fig. 5A to H). After running the programme, several plots and tables were created to visualise the model output such as the plot concentration vs. depth (Fig. 6), age-erosion plot (Fig. 7), several plots visualising the solution space of the output parameters (Fig. 8) and the output statistics (Tab. 2). The simulator was demonstrated using the ^{10}Be data from a fluvial terrace at Lees Ferry (Hidy et al. 2005). For this example, the optimisation did not converge to a single solution. The results show a wide range of ages with chi-squared values essentially identical to the minimum chi-squared value (Fig. 7). Therefore, the resulting age does not approach a unique value when the chi-squared value decreases to the minimum value allowed by this data set. In case no convergence exists in the solution space, a constraint has to be applied on the net erosion or erosion rate. However, the code forces the modelled age to be equal to the modelled value of total erosion divided by the modelled value of the erosion rate. According to Hidy et al. such a constraint can only be applied if independent geological information is available to justify the assumption made. In the case of Lees Ferry, the authors selected a net erosion constraint of 30 cm based on the comparison with an eroded terrace nearby (Hidy, pers. comm.). Consequently, the solution space converges, and an age and erosion rate can be determined (Fig. 7 and 8). Hidy et al. (2010) suggested taking the "Mode" and the "Minimum" and "Maximum" ages for the upper 2σ bound (Tab. 2). Unfortunately, there are no hints or remarks in the paper that indicate when the profile is in steady state and how the analysis should then be treated. Implicitly, the authors refer in the case of steady state to application of some constraint in the model parameters (in the case where there are some independent geological constraints). However, if geological constraints are absent, the user might be confused as to why the code does not give unique solutions.

Tab. 1: Relevant input variables for the simulation of a profile

Hidy et al. (2010)

Relevant input variables	**Unit**	**Description**
Location data	°	Altitude, latitude/longitude of profile site
Shielding data	-	Shielding data for the site
Sample data	at/g	Sample concentrations, error in measurement
Density data	g/cm^3	Constant density of the profile, or densities of the corresponding sample horizons
Spallogenic production	at/g/yr	Manual entry (calculated from another source, or internally using the reference production rate (scaling Lal 1991/Stone 2000)
Neutron attenuation	g/cm^2	Neutron attenuation length is constant or varies
Parameter for muon production	m	Depth of curve fit to muon production after Heisinger et al. (2002c) or Braucher et al. (2013)
Age	yr	Constant age, random variation between two end-member values, normal distribution around a mean value
Net erosion, total erosion threshold	cm	Maximum/minimum erosion estimated from site (can be negative for aggradation)
Erosion rate	cm/kyr	Constant erosion rate, random variation between two end-member values, normal distribution around a mean value
Inheritance	at/g	Constant inheritance, random variation between two end-member values, normal distribution around a mean value
Chi-squared cut-off	-	Accepted profile solutions must be lower than reduced chi-squared value

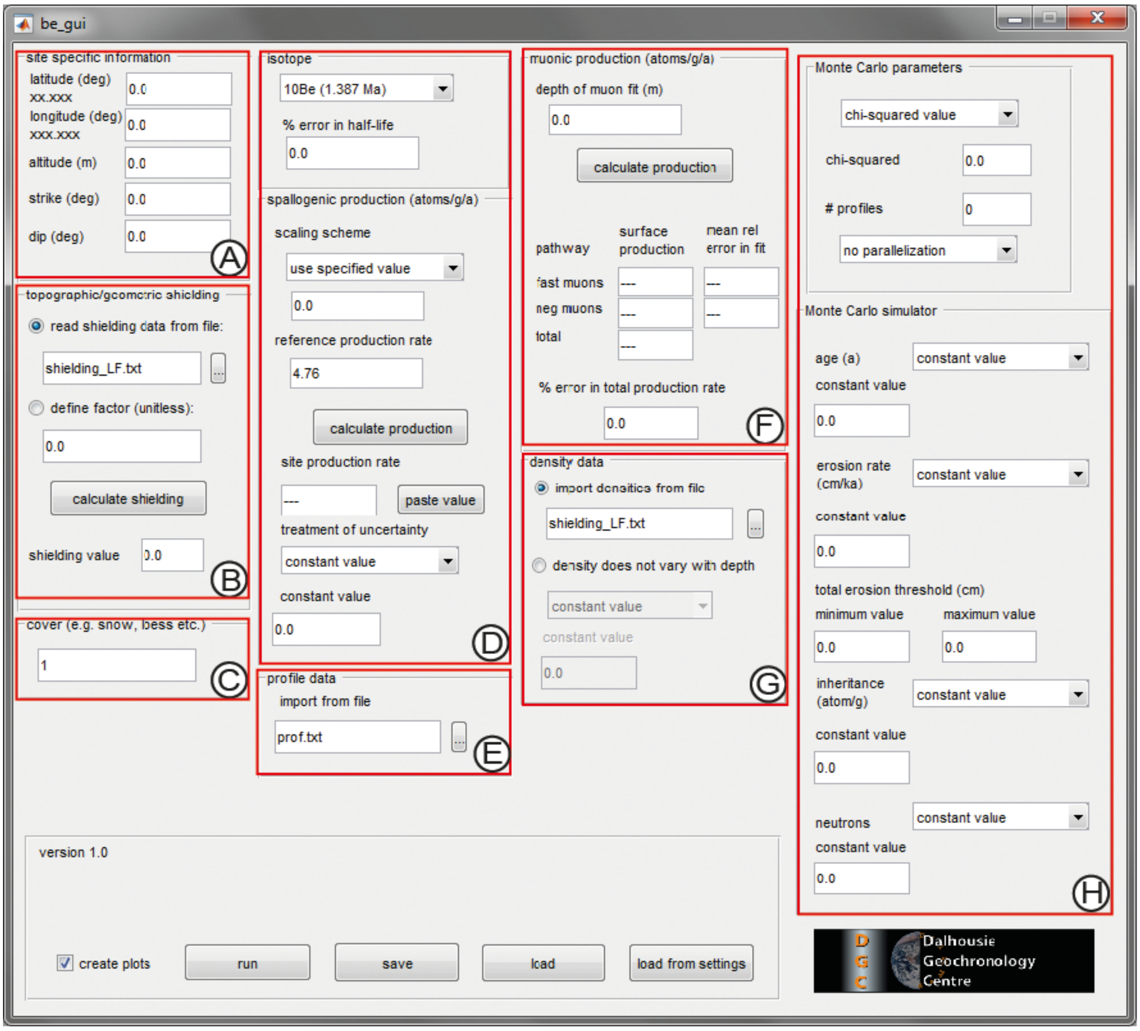

Fig. 5: Snapshot of the graphical user interface for the Matlab™ version of the programme Hidy et al. (2010). Input boxes for A) site-specific geographical information, B) shielding from cosmic rays, C) shielding at the profile through snow/loess, D) scaling the spallogenic production pathway, E) 10Be data, F) scaling of the muogenic production pathways, G) density of the sediment along the profile or assumed density (interval or value with different uncertainty distributions), H) parameters for the Monte Carlo routine such as chi-squared (cut-off value), age, erosion rate, net erosion or total erosion threshold, inheritance and neutron attenuation length.

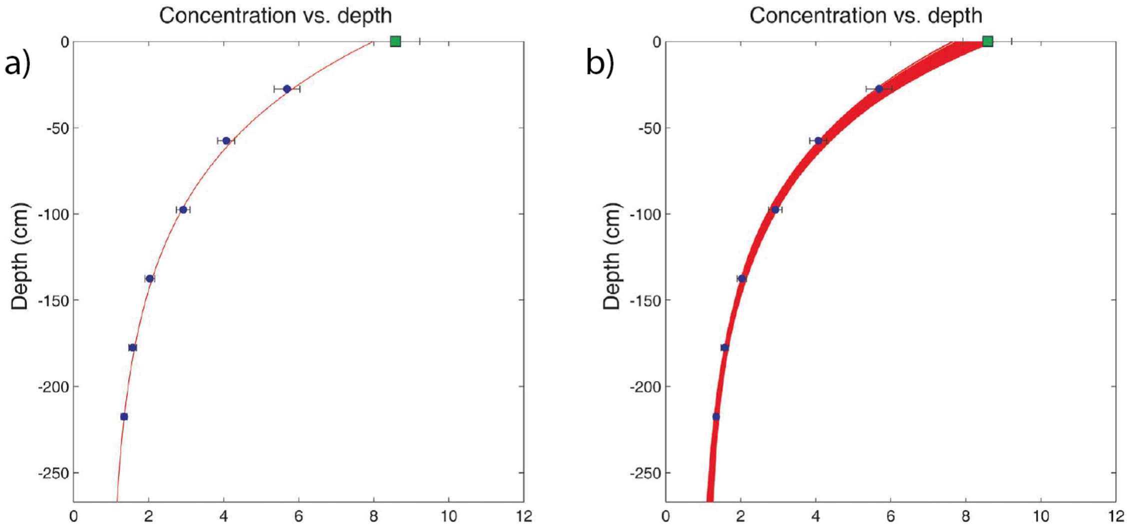

Fig. 6: Concentration versus depth plot profiles consisting of sand samples from Lees Ferry Hidy et al. (2010). a) The best fits to equation (1). b) the 2σ profile solution space

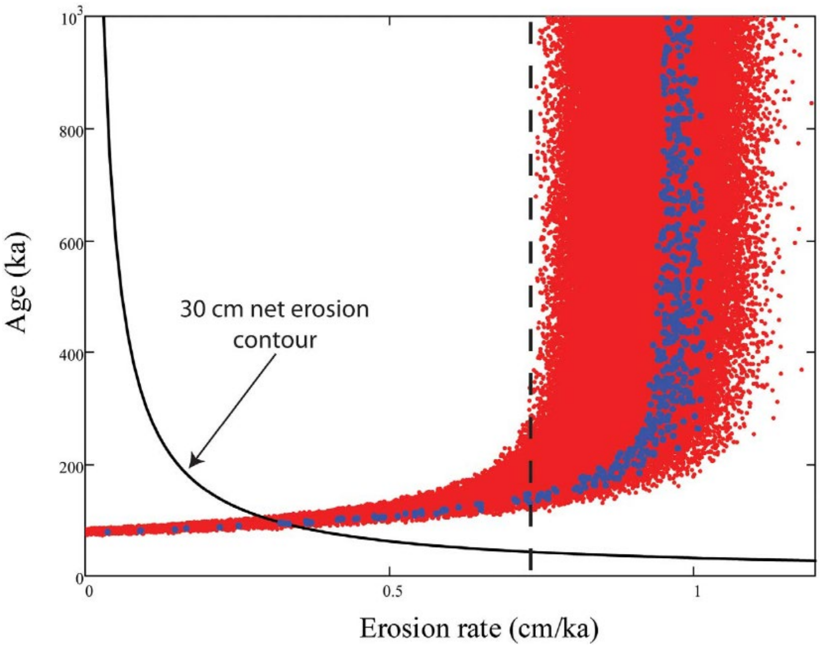

Fig. 7: Age-erosion rate plot for the simulation of the profile consisting of sand samples showing the solution space (red dots) with no erosion constraint

The 500 best (lowest chi-squared) solution pairs (out of 100'000 runs) are broadly scattered and clearly show that no convergence exists (blue dots). The 30 cm net erosion contour (solid black line) and the erosion rate cutoff (dashed black line) are possible constraints the user can apply to obtain convergence and a finite age. Without the constraint, only a lower age limit (zero erosion limit) can be determined for this dataset.

Tab. 2: Statistics for the simulation of a profile

Hidy et al. (2010)

	Age (ka)	**Inheritance** (10^4 at/g)	**Erosion rate** (cm/kyr)
Mean	86.0	9.35	0.17
Median	85.7	9.40	0.18
Mode	83.9	9.49	0.28
Lowest χ^2	76.8	8.21	0.06
Maximum	103.8	10.7	0.35
Minimum	69.8	6.97	0.00

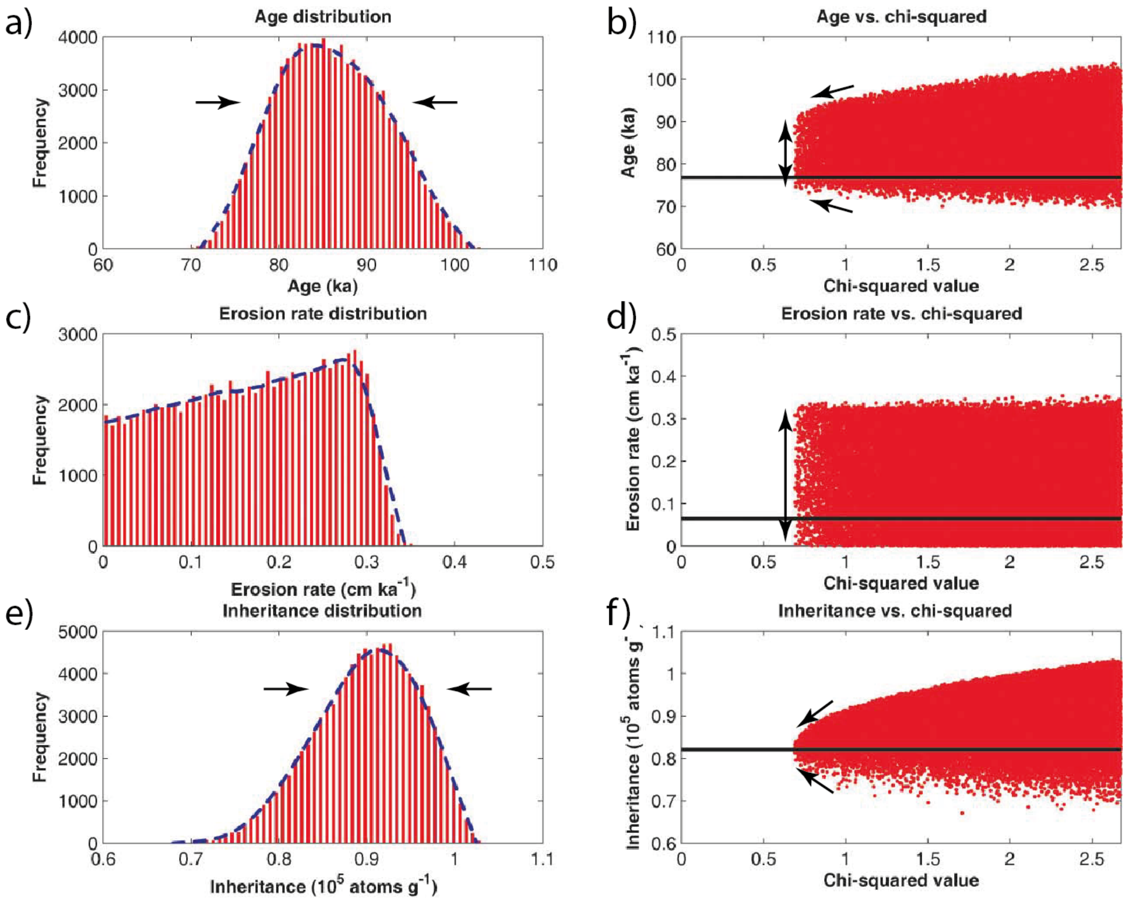

Fig. 8: Results for age, inheritance, and erosion rate solution spaces for a profile at Lees Ferry

Hidy et al. (2010). Solid black lines indicate the lowest chi-squared value. The output statistics for this simulation are shown in Tab. 2. The black arrows indicate the convergence of the solution space to a narrower solution interval forced by applying the net erosion threshold. For the parameters age and erosion rate, the convergence is less complete i.e. for lowest chi-squared values multiple solutions are possible for the parameter "inheritance".

Soon after the paper of Hidy et al. (2010) was published, an update of the ^{10}Be profile simulator version 1.2 was provided. The major difference to version 1.0 was the implementation of the sampling of simulations to create Bayesian probability distribution curves and estimates of the most probable values as well as errors. The Bayesian solutions are a more accurate representation of the most probable values for age, erosion rate and inheritance solutions considering the entire solution space. Furthermore, the Bayesian approach is helpful for estimating the reliability and likelihood of the output results. Additionally, the best 100 chi-squared values (before, 500) are now plotted on the age-erosion solution space plot.

In similar depth profile studies, Siame et al. (2004) and Braucher et al. (2009) always recognised steady state (if it existed) in analysed profiles by interpreting the age-erosion plot and modelling results. A similar approach was taken by Viveen et al. (2012). The latter systematically modelled their data from terraces of the Miño River (NW Iberian Atlantic Margin) with open parameter ranges (exposure age, erosion, inheritance or density). Unrealistically high ages (e.g. > 5 Ma) suggested that steady state may have been reached at this site. A finite age range could not be constrained because no additional geological constraints were applied but were also not available. Therefore, for the given erosion rate, only a minimum exposure age can be calculated (Eq. (2). This is the "integration time" of Lal et al. (1991) that corresponds to the time needed to accumulate the maximum concentration possible for a given erosion rate. For profiles in steady state, this is the most conservative estimate of the minimum age; nevertheless, this approach does not consider inherited amounts of cosmogenic nuclides from previous exposure.

$$T_{eff} = \frac{1}{\lambda + (\frac{\rho}{\Lambda}) \cdot \varepsilon} \qquad \text{Eq. (2)}$$

Where T_{eff} is the mean, effective time needed to reach steady state within the uppermost surface.

To determine whether a depth profile has reached equilibrium, the time in Eq. (1) is set to infinity and the concentration at each depth is modelled as a function of the erosion rate. This yields maximum erosion rates for the profile that are equal to the modelled erosion rate from the output of the Hidy code (for a saturated depth profile).

^{10}Be depth profiles of young fluvial terraces from the Crau Plain, SE France (Molliex et al. 2013) and Ardennes, Belgium (Rixhon et al. 2014) were modelled using the chi-squared Monte Carlo modelling approach developed by Braucher et al. (2009). Due to rather low-profile erosion rates of a few cm/kyr to mm/kyr, the profiles were not yet at steady state and it was possible to estimate an age.

In the Swiss foreland, the Mandach (Akçar et al. 2014) and Stadlerberg sites (Claude et al. 2017), both suggested as belonging to the Höhere Deckenschotter units, have been investigated using ^{10}Be depth profiles. The Mandach profile consists of only four data points, which is the absolute minimum for modelling with the Hidy code (Hidy et al. 2010). Both profiles show a clear exponential trend but with some scatter in the data. For example, the lowest point in the Mandach profile is slightly higher but still overlaps within 1σ uncertainty with the next higher sample. The maximum profile erosion rates for Mandach were reported to be 11 to 22 cm/kyr or 110 to 220 m/Myr, and 4 to 6 cm/kyr or 40 to 60 m/Myr for Stadlerberg. As the optimisation did not converge to a single solution with unconstrained parameters for both profiles, the authors applied a total net erosion threshold interval of 125 – 200 m and 75 – 110 m for Mandach and Stadlerberg, respectively. In both papers, the reasoning for the chosen net erosion threshold is missing. Therefore, the proof of independent geological constraints is missing and remains speculative. Consequently, the reported model ages of 1 Ma and 1.8 Ma rely on this speculative net erosion threshold because the modelled age multiplied by the modelled erosion rate has to be equal to the net erosion.

From the Ariège river in the Eastern Pyrenees, Delmas et al. (2015) report ^{10}Be depth profiles from young fluvial terraces. The profile data were modelled with a Monte Carlo routing and the chi-squared statistical test to simulate a multitude of statistically acceptable best-fit solutions. In contrast to Hidy et al. (2010), who considered the most probable quadruplets of solutions (age, erosion rate, inheritance and density) as those matching the 100 lowest chi-squared values, Delmas et al. (2015) graded as acceptable any model with a chi-squared value situated between the lowest chi-squared (χ^2min) and [χ^2min + 1]. The latter range of solution is considered as a mathematical substitute for the 1σ confidence interval. Most of the profiles presented in this paper are typical examples of profiles being far from steady state: a narrow and well-defined interval within 1σ and a large range of erosion rates (gently increasing left part of the solution space in the age-erosion rate plot of depth profiles).

Ruszkiczay-Rüdiger et al. (2016) published ^{10}Be data from Hungarian Danube terraces and estimated the ages with the help of an updated Hidy depth profile simulator. The updated version takes the newer muogenic production pathways following Braucher et al. (2011) into account instead of the equations of Heisinger et al. (2002a, 2002b). Ruszkiczay-Rüdiger et al. (2016) presented an easy and clear procedure to test whether a profile has reached steady state or not (similarly to Viveen et al. 2012). Thus, depth profiles should be tested for steady state by assuming an infinite exposure age for all samples along the depth profile and calculating the maximum erosion rates using Eq. (1). If the erosion rates are increasing from top to bottom, then steady state has not been reached and an exposure age can be determined. If the erosion rate remains constant along depth, steady state has been achieved and a first minimum deposition age T_{eff} can be estimated using Eq. (2) (cf. Lal et al. 1991, Viveen et al. 2012 for example). Additionally, Ruszkiczay-Rüdiger et al. (2016) suggest undertaking chi-squared minimisations using the updated ^{10}Be depth profile similar to the already noted incorporation of the Bayesian statistics. The Bayesian 2σ lower ages are taken as minimum ages when ^{10}Be concentrations are in secular equilibrium. For profiles where ^{10}Be concentrations have not yet reached a secular equilibrium, the reported uncertainties for the age are Bayesian 1σ lower and upper values (cf. Ruszkiczay-Rüdiger et al. 2016). For three terraces, a net erosion threshold of a few metres was applied in order to constrain the age and the most probable minimum ages. The net erosion thresholds also applied to a few other terraces for which ^{10}Be profiles were measured are mostly in the order of ~ 5 – 15 m. Geological evidence such as local stratigraphy and geology for the choice of the net erosion constraints are provided in the paper.

A more comprehensive quantification of parameter and prediction uncertainty than with the Hidy code is provided by the Bayesian framework (Laloy et al. 2017). Laloy et al. (2017) modelled ^{10}Be depth profiles from fluvial terraces in Belgium and the Netherlands by using Bayes' theorem to represent parameter uncertainty and quantify model errors. The authors used the depth profiles as robust estimates for profile erosion rates but not for exposure ages. Although they do not explicitly mention it, their profiles are in steady state as there are a wide range of age estimates equally likely for the same erosion rate.

Recently, Delmas et al. (2018) presented ^{10}Be depth profiles from the Têt River in the Eastern Pyrenees. The authors follow Delmas et al. (2015) by reporting age estimates within the 1σ range. Visualisation of the accepted best-fit solution within the 1σ range as well as 100 lowest chi-squared values in the age-erosion rate plot help to identify once more whether steady state in the profile has been achieved. Indeed, for some of the profiles, secular equilibrium has been reached and therefore only minimum age were reported. Model runs with unconstrained variables then clearly show an intractably broad band of exposure ages (a few 100 ka to several 100 ka to Ma), but a narrow band of profile erosion rates. As noted before, such a distribution of age and erosion rate pairs indicates that ^{10}Be concentrations throughout the vertical profile satisfy the conditions of a nuclide steady state. Delmas et al. also note that the data modelling thus provides an excellent estimate of the post-depositional mean erosion of the terrace but only a minimum exposure age for the terrace tread.

Ruszkiczay-Rudiger et al. (2018) presented depth profiles from the Danube basin and introduced a new method for defining the maximum age estimate possible determined using depth profiles. For this purpose, the evolution of the ^{10}Be concentration for the lowermost sample (= maximum depth of the sampled profile) is calculated. The linear increase (on a logarithmic axis) during the production of ^{10}Be intersects with the steady state concentration for the maximum profile erosion rate (Fig. 9). The intersection point gives the maximum reasonable determinable age. In other words, beyond the intersection point the profile has reached steady state at the maximum sampled depth and only a minimum age can be obtained. In a second step, simulations with the Hidy code are performed using the entire profile data. If the most probable Bayesian value is above the previously calculated maximum age and the output plots suggest the profile being in steady state, then the Bayesian 1σ lower age is taken as the minimum age for terrace abandonment.

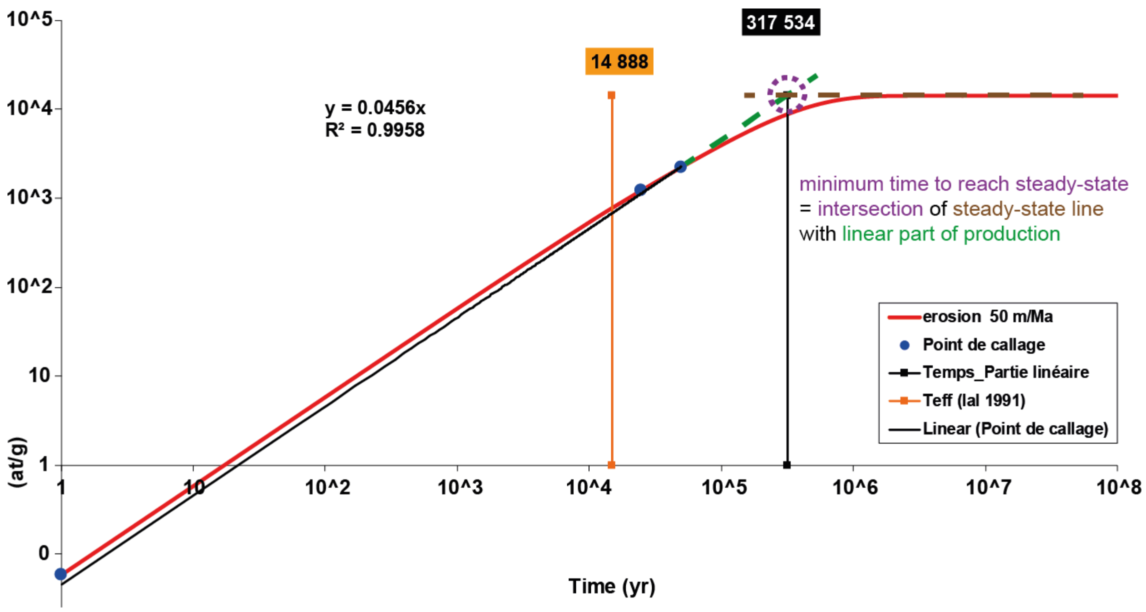

Fig. 9: Double-logarithmic plot of time vs. ^{10}Be concentration showing the linear increase of ^{10}Be during production and ending up at the plateau of steady state concentration depending on the (constant) profile erosion rate

This plot graphically illustrates the maximum age at which depth profiles can potentially deliver age constraints. The maximum age is obtained by the intersection of the maximum ^{10}Be concentration divided by the linear production part. The mean integration timescale for the lowermost sample which is represented in the maximum age is much larger than the most conservative integration timescale calculated for the surface, as it is represented by T_{eff} from Lal et al. (1991).

The most recent contribution to depth profiles is provided by Claude et al. (2019) presenting depth profile data from the Irchel plateau mountain located in the Northern Swiss foreland. For example, for the Wilemer Irchel site the results are reviewed in detail: for the depth-profile modelling, three different net erosion scenarios were applied using 0 – 150 m (total erosion from 0 to 150 m maximum), -10 – 150 m (aggradation of 10 m maximum, e.g. loess, and erosion 150 m maximum) and 100 – 150 m (total erosion of 100 m minimum to 150 m maximum). In the results chapter of the paper, the results from the third scenario of 100 to 150 m net erosion were selected without explaining why. The resulting modal age is $2.8^{+1.8}_{-1.0}$ Myr and the erosion rate $4.5^{+1.3}_{-1.4}$ cm/kyr. No explanation of the chosen net erosion scenario can be found later in the discussion or in the Appendix. In this paper, previously published depth profiles were re-calculated, such as the ones from Mandach (Akçar et al. 2014) and Stadlerberg (Claude et al. 2017), resulting in significantly larger error bars of the reported ages with $0.8^{+1.3}_{-0.4}$ Myr and $2.4^{+2.4}_{-1.2}$ Myr, respectively, with 100 – 150 m net erosion constraints. Again, the independent evidence of total net erosion constraint which is required to support the chosen scenarios for the age modelling is not documented in the paper. Therefore, it is difficult to judge whether the arbitrarily assumed net erosion scenario holds true and, consequently, the reported ages are subject to further discussion.

2.3 Synthetic depth profiles and steady state

To explore the evolution of ^{10}Be depth profiles theoretically, we tracked synthetic profiles along specific time steps. The ^{10}Be depth profile of Stadlerberg (Claude et al. 2017) serves as an example which we wish to compare with a synthetic profile. Prior to the comparison, synthetic depth profiles with selected exposure times are created using Eq. (1) and site-specific parameters of Stadlerberg (e.g. geographical information, density and erosion rate from Claude et al. (2017). These exposure times feed into the depth profile equation and are labelled as synthetic exposure times. Six different synthetic exposure times for the same erosion rate of 5 cm/kyr (converted to mass erosion rate) were used (see Tab. 3 for an overview of the parameters). Inheritance was set to zero in order to reduce a variable that results in two known parameters exposure time and erosion rate only. The impact of inheritance on the results of modelled ages will be discussed below.

Tab. 3: Input variables for Eq. (1) that quantify the ^{10}Be concentration of a depth profile

Relevant input variables	**Value**	**Unit**	**Description**
Mass erosion rate, ε	0.0025	$g/cm^2/y$	Constant along depth, represents an erosion rate of 5 cm/kyr for a profile density of 2 g/cm^3
Exposure time, t	0.01, 0.1, 0.2, 0.3, 1, 10	Myr	6 different "model" exposure times
Total profile depth, x	10	m	Representative total profile depth
Virtual sampling depths	0, 0.5, 1, 1.5, 2., 4, 6, 8, 10	m	Similar sampling scheme as for real profiles
Spallogenic production, P_{sp}	7.18 ± 0.5	at/g/yr	Lal (1991)/Stone (2000) scaling for the site (610 m a.s.l, 47.5° N/8.5° E) using the sea level-high latitude spallogenic production rate of 4.01 at/g/yr (Phillips et al. 2016)
Muogenic production, $P_{\mu slow}$, $P_{\mu fast}$	0.039, 0.012	at/g/yr	Braucher et al. (2011)
Attenuation lengths, L_{sp}, $L_{\mu slow}$ and $L_{\mu fast}$	160, 1'500, 4'320	g/cm^2	Attenuation length for neutron, slow and fast muons

In Fig. 10, the synthetic depth profiles with the synthetic exposure times are plotted.

The evolution of the depth profile shows a fast approach to secular equilibrium for the surface soon after 10 kyr. For the uppermost 1 m of the profile, steady state is achieved within 300 kyr. The cross-over zone – the so-called exponential knee – i.e. the transition from spallogenic to muonic production, is well visible within a depth range of 1.5 to ~ 2.5 m. The profile part below the cross-over zone is controlled by the much slower muogenic production pathways and thus steady state is approached much later at 1 Myr. In the classical plot of ^{10}Be concentration versus exposure time (Fig. 11), the approach to steady state for the uppermost 2 m of the profile is again clearly visible. Steady state is also reached at greater depths, but much later at ~ 1 Myr.

The synthetic profiles combined with a generic 1σ uncertainty of 8 % (based on AMS measurement) were taken as input profiles for the depth profile simulator of the Hidy code version 1.2 (Hidy et al. 2010). The goal was to track the evolution of the output parameters age, erosion rate and inheritance modelled by the Hidy-code. As the synthetic profiles are scaled to the Stadlerberg site, the same site-specific parameters were used as in the paper of Claude et al. (2017) (Tab. 4). The synthetic profiles were calculated without an inheritance prior to exposure. In order to give the model a certain freedom, an interval of 0 – 5'000 at/g was allowed. To avoid constraining any solution space, we left the input range for the age, erosion rate and net erosion threshold wide open in order to avoid cutting any solutions, i.e. age range of 0 – 5 Myr, erosion rate of 0 – 10 cm/kyr, inheritance of 0 – 5'000 at/g. The inheritance was explicitly not set to zero in order to check the simulator for model errors and allow some freedom for the calculation. The density was set constant to 2 g/cm^3 and the chi-squared value to 2, which is close to 1, which would be the lowest possible value in any case. The entire solution space was written to a separate text file and out of this a 3D plot of age, erosion rate and inheritance was created (Fig. 12). For a better visualisation of the results, the hundred best-fit results were coloured in blue. Age intervals were reported with Bayesian most probable and lower- and upper 2σ values (Tab. 5).

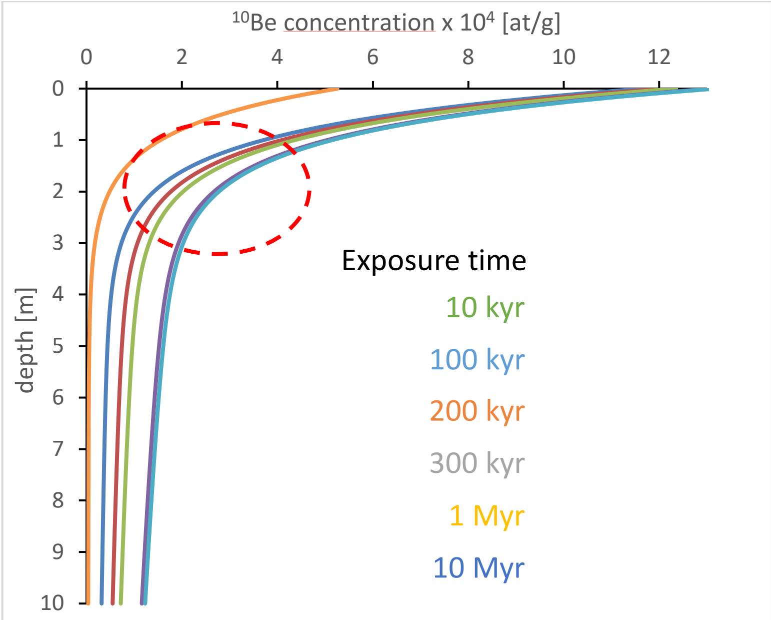

Fig. 10: Plot of ^{10}Be concentration versus depth with different exposure times for a profile erosion rate of 5 cm/kyr and zero inheritance

The red-dashed circle indicates the cross-over zone from predominantly spallogenic to muogenic production.

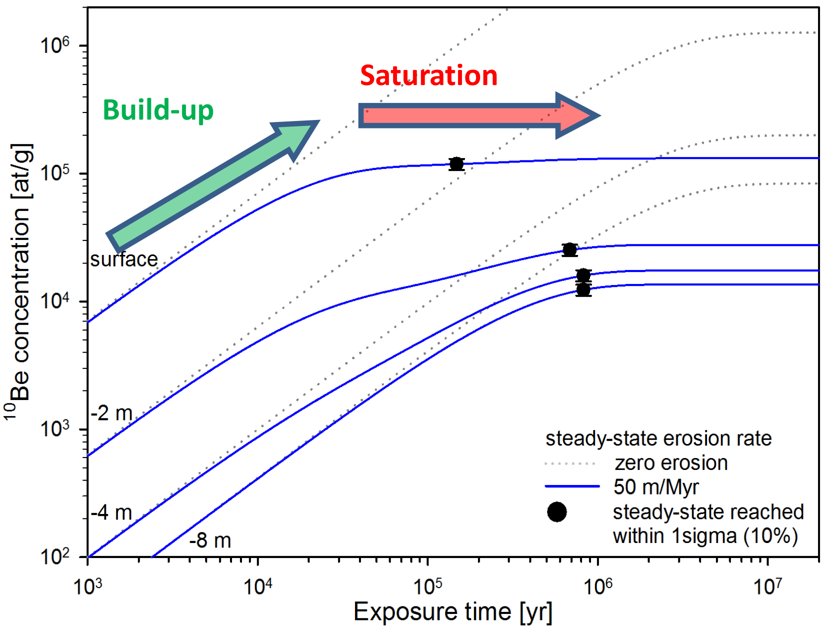

Fig. 11: Plot of ^{10}Be concentration versus exposure time (log-scale) with no erosion and an erosion rate of 50 m/Myr (5 cm/kyr) for the profile depths of 0, 2, 4 and 8 m

The black point indicates the exposure time when the corresponding ^{10}Be concentration is within a typical 1σ uncertainty of 10 % to the ^{10}Be concentration at steady state. The little "hump" for the profile depth of 2 m at exposure times of 80 to 300 kyr is due to the combination of a tendency towards lower spallogenic production and increasingly higher muonic production (cross-over zone).

Tab. 4: Input parameters for the Hidy code

Relevant input variables	Value	Unit	Description
Location data	610, 47.5/8.5	m, °	Altitude; latitude/longitude of profile site
Shielding data	1.0	-	Shielding data for the site
Sample data	synthetic	at/g	Sample concentrations, 8 % 1σ error in measurement
Density data	2	g/cm^3	Constant density of the profile
Spallogenic production	7.18 ± 0.5	at/g/yr	Internally calculated using the reference production rate sea-level-high latitude spallogenic production rate of 4.01 at/g/yr (Phillips et al. 2016, scaling Lal 1991/Stone 2000
Neutron attenuation	160	g/cm^2	Constant neutron attenuation length
Muon production	8	m	Depth of curve fit to muon production Braucher et al. (2011)
Age	0 – 5	Myr	Age with random variation between two endmembers
Net erosion, total erosion	-	cm	Maximum/minimum erosion estimated from site
Erosion rate	3 – 8	cm/kyr	Erosion rate with random variation between two endmembers
Inheritance	0 – 5'000	at/g	Inheritance with random variation between two endmembers
Chi-squared cut-off		-	Accepted profile solutions must be lower than the reduced chi-squared value (normalised for the available degrees of freedom)

The solution space presented in the age-erosion rate plot obtained from the Hidy code by having a synthetic profile with a synthetic exposure time of 200 kyr shows (Fig. 12a) that, for ages from 0 to 5 Myr, a corresponding erosion rate and inheritance can be found. However, the top 100 best-fits plot around a single spot at an erosion rate of around 5 cm/kyr and an age of ~ 200 – 400 kyr. Visually, the solution space converges to a single solution, but the output statistics already likely indicate a steady state profile as the two-σ interval extends from 27 kyr to 4.8 Myr, with the most probable age of 217 kyr being close to the model age of 200 kyr. The erosion rate interval is within 3.7 to 9.2 cm/kyr and a most probable value of 7.3 cm/kyr.

A synthetic profile with the slightly higher exposure time of 300 kyr yields results similar to those mentioned above (Fig. 12b). The modelled age interval lies at 190 kyr to 4.9 Myr, with the most probable value around 326 kyr, thus again indicating that steady state might have been reached already (indicated in the figure as "divergence"). The top 100 best-fit points plot now in a bit more extended interval, indicating that the solutions have the tendency to spread more. The erosion rate interval lies within 4.3 to 7.7 cm/kyr and a most probable value of 5.9 cm/kyr.

1 Myr was the exposure time of the third synthetic profile whose solution space from the Hidy code was investigated (Fig. 12c). In the age-erosion rate plot, it can clearly be seen that only the vertical branch with a very wide age range for a narrow range of erosion rates is visible. Likewise, the top 100 best-fits plot from 1 to 4 Myr age and profile erosion rates between 4 – 5 cm/kyr and a clear divergence of the blue points occurs. The reported age interval ranges from 0.5 to 4.9 Myr, with a most probable value of 1.4 Myr. The erosion rate indicates an interval of 3.5 to 5.6 with a most probable value around 4.2 cm/kyr.

Tab. 5: Output statistics for the simulation of the synthetic profiles with different exposure times from the Hidy code

	Age (kyr)	**Erosion rate** (cm/kyr)
Profile of 200 kyr synthetic exposure time		
Bayesian most probable	217.4	7.17
Bayesian 2σ-upper	4'882.8	9.07
Bayesian 2σ-lower	26.9	3.74
Profile of 300 kyr synthetic exposure time		
Bayesian most probable	326.1	5.87
Bayesian 2σ-upper	4'893.8	7.64
Bayesian 2σ-lower	188.6	4.27
Profile of 1 Myr synthetic exposure time		
Bayesian most probable	1'413.0	4.24
Bayesian 2σ-upper	4'856.4	5.57
Bayesian 2σ-lower	521.1	3.48
Profile of 1 Myr synthetic exposure time net erosion constraint (75 – 110 m)		
Bayesian most probable	2'010.9	4.35
Bayesian 2σ-upper	2'813.6	5.61
Bayesian 2σ-lower	1'442.0	3.49

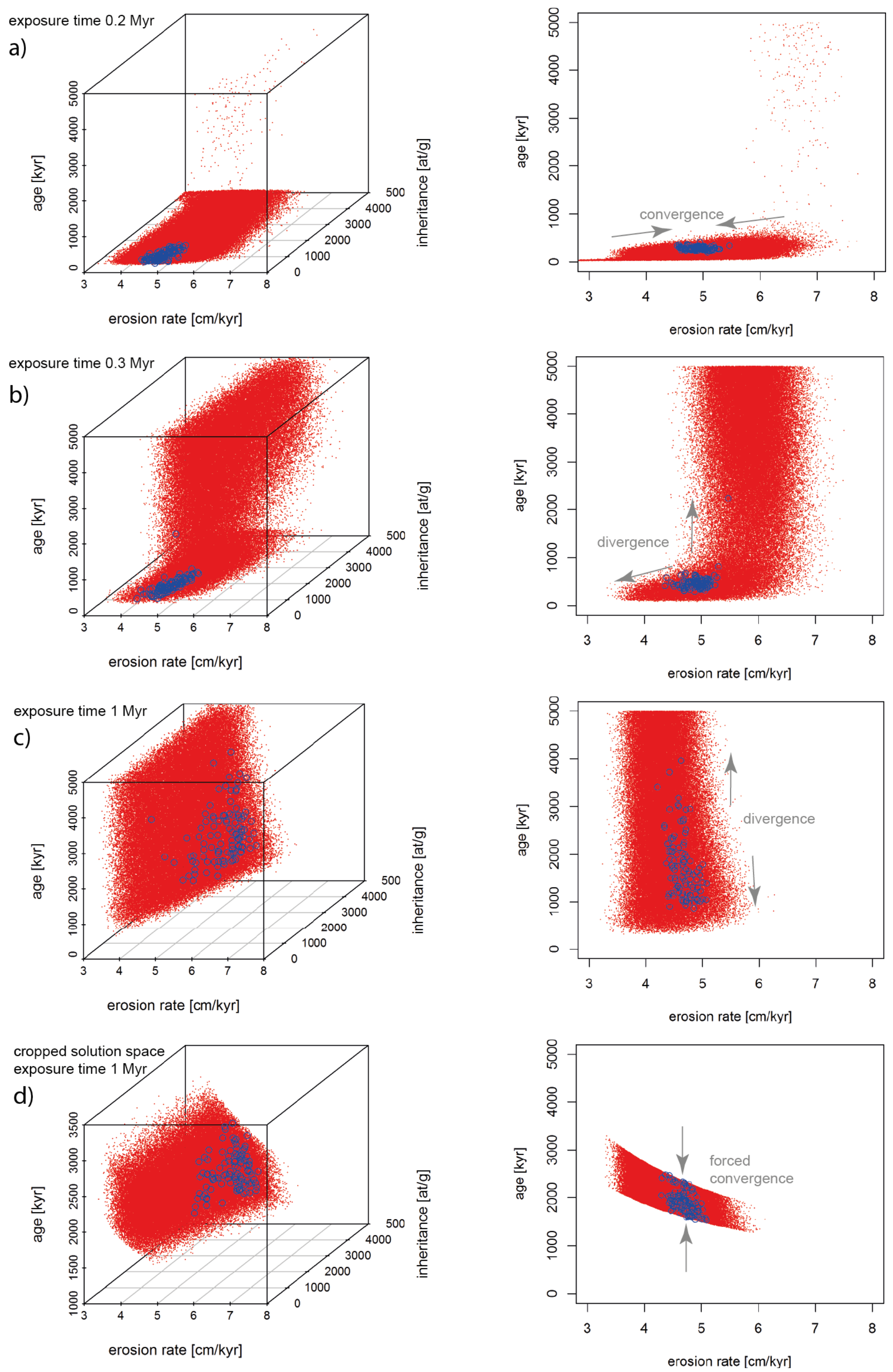

Fig. 12: Plot of the entire solution space (red points) and top 100 best-fit solutions (100 lowest chi-squared values, blue points) modelled by the Hidy code (in 3D and 2D)

The synthetic profile underlying this solution space had synthetically created depth profiles with exposure times of a) 0.2, b) 0.3, c) and d) 1 Myr and an erosion rate of 5 cm/kyr.

The assessment of the results from the Hidy code based on the three different profiles confirms initial observations made from the 3D and 2D plots. The probability density function (pdf) and cumulative distribution function (cdf) for the age and erosion rate are plotted regarding the entire solution space and for the minimum chi-squared values (Fig. 13). For the profile with an exposure time of 200 kyr, the pdf of both the entire solution space and the minimum chi-squared values in the age-erosion plot follow each other and form a Gaussian curve, indicating a convergence (Fig. 13A). However, the cdf suggests that the possibility of an age interval of 0 –400 kyr lies at less than 50 % and, therefore, the remaining 50 % probability is valid for an age interval from 400 kyr to 5 Myr. A clear pattern can be observed for the profiles with synthetic exposure times of 300 kyr and 1 Myr (Fig. 13B-C), where the pdf of both the entire solution space and the minimum chi-squared values show a plateau-like curve, indicating that there is a similar, low probability for ages between 0 to 5 Myr. The cdf confirms this divergence in the solution space and that multiple solutions for a wide interval are possible. For all exposure times of 200, 300 kyr and 1 Myr, the erosion rate shows a rather nice Gaussian shape, indicating that there is consensus about the erosion rate. Indeed, the model clearly shows solutions around 5 cm/kyr as predefined for the synthetic depth profiles. Investigating the profile with an exposure time of 1 Myr and a cropped solution space (due to an arbitrarily chosen net erosion threshold of 75 – 110 m), the pdf of both the entire solution space and minimum chi-squared values are similar and indicate a well-defined, narrow age interval (Fig. 13D). The shape of the cdf in the plot is much steeper, again implying a narrow age interval.

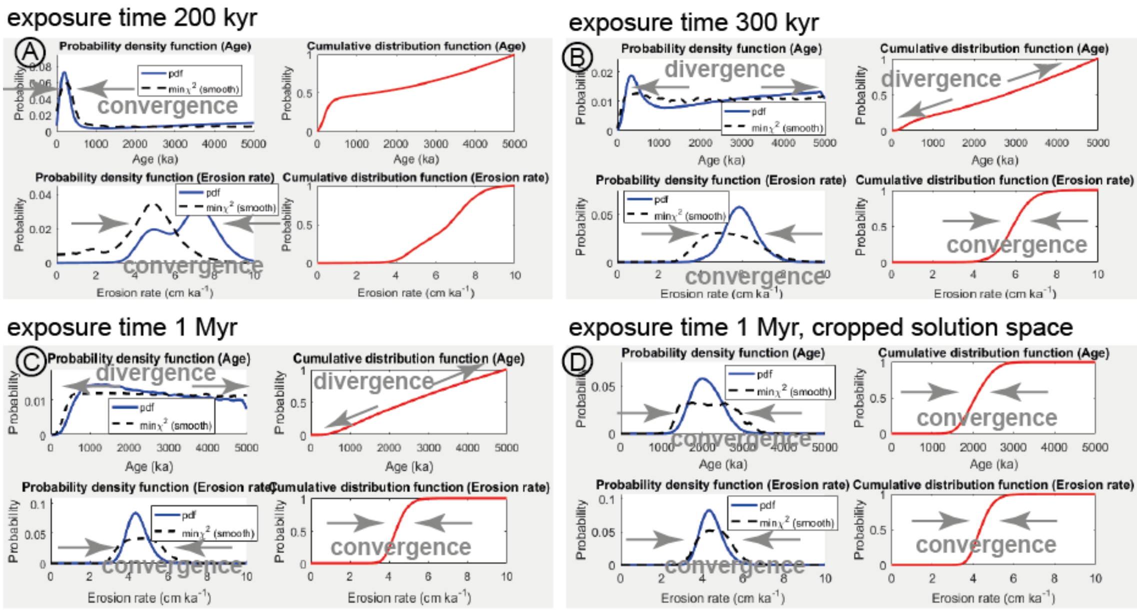

Fig. 13: Plot of the output statistics for the profile with an erosion rate of 5 cm/kyr and four different exposure times a) 200 kyr, b) 400 kyr, c) 1 Myr and d) 1 Myr with cropped solution space (net erosion threshold of 75 – 110 m)

The indications of convergence and divergence in calculated age solutions for a specific erosion rate should highlight the evolution from a single solution to steady state (in grey with arrows). See text for more details.

For another simulation with the Hidy code, the 1-Myr-old synthetic profile was taken and a much lower net erosion threshold of 50 – 75 m and 25 – 50 m was applied (Fig. 14A and B, Tab. 6). The modelled age interval for the case 50 – 75 m of total erosion was 0.9 to 1.9 Myr with 1.4 Myr being the most probable. For the case with less total erosion of 25 to 50 m, the result was an age interval of 0.5 to 1.2 Myr, with 0.9 Myr being the most probable. Accordingly, the modelled age strongly depends on the values taken for the net erosion threshold. Regardless of the chosen net erosion threshold, the solution space is constrained and forced to convergence. Therefore, the net erosion threshold should come from an independent geological record or database. However, the older the sediment deposit to be dated the more difficult it will be.

Tab. 6: Statistics for the simulation of the synthetic profiles with different exposure times from the Hidy code

Profile of 1 Myr synthetic exposure time net erosion constraint (50 – 75 m)		
Bayesian most probable	1'358.7	4.35
Bayesian 2σ-upper	1'898.8	5.71
Bayesian 2σ-lower	944.4	3.50
Profile of 1 Myr synthetic exposure time net erosion constraint (25 – 50 m)		
Bayesian most probable	869.6	4.24
Bayesian 2σ-upper	1'249.8	5.64
Bayesian 2σ-lower	507.3	3.42

Additionally, the synthetic profiles are now checked for steady state using the approach of Viveen et al. (2012) and Ruszkiczay-Rüdiger et al. (2016). As already mentioned, for each data point, the maximum erosion rate is calculated assuming infinite exposure time. Of course, the maximum erosion rates calculated by these approaches agree well with the predefined value of 5 cm/kyr. By plotting the maximum erosion rate along the profile, there are three possible trends: increasing rate from top to bottom, constant rate along depth or constant rate along the topmost metres and increasing further down (cf. Ruszkiczay-Rüdiger et al. 2016). In Fig. 15, the maximum erosion rates of our synthetic profiles (0.1, 0.3 and 1 Myr) are plotted together with the calculated rates from the ^{10}Be depth profiles presented in Claude et al. (2017) (will be discussed in the next section). According to the classification scheme, the first two profiles do not yet seem to be in steady state, as is clearly the case for the 1 Myr profile.

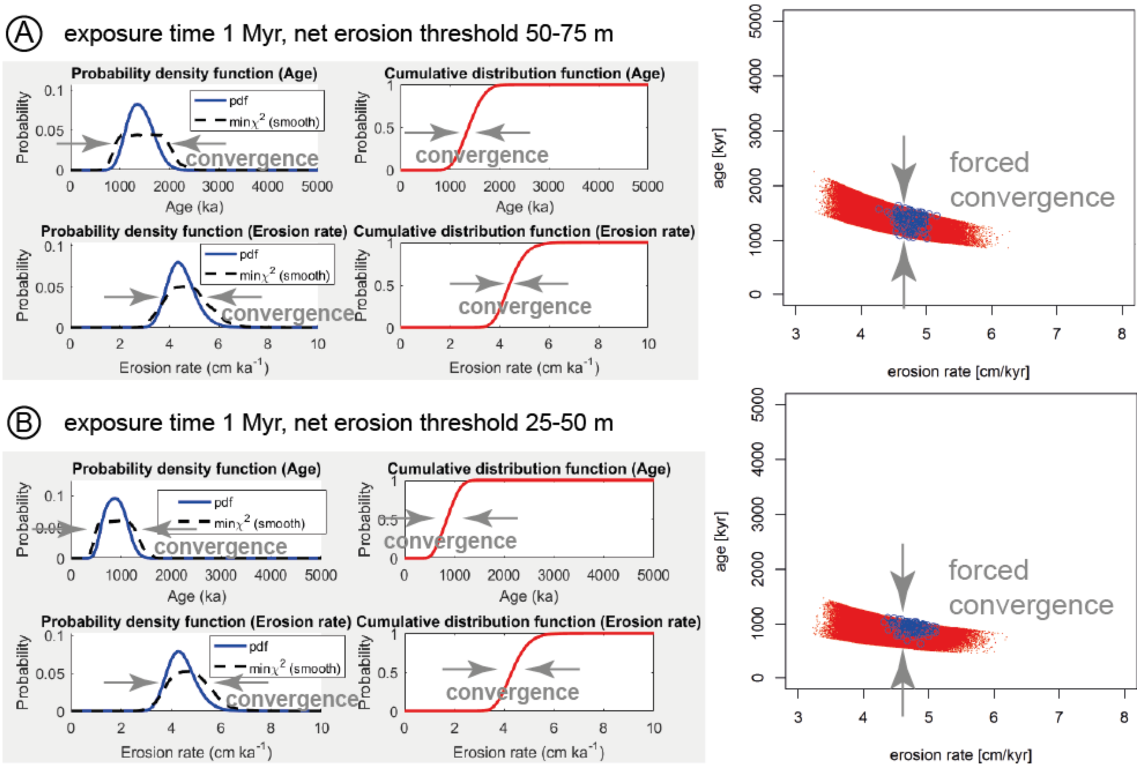

Fig. 14: Plot of the output statistics and the cropped solution space (red points) modelled by the Hidy code

The synthetic profile underlying this solution space had a model age of 1 Myr and an erosion rate of 5 cm/kyr. The total net erosion threshold was 50 – 75 m (A) and 25 – 50 m (B)

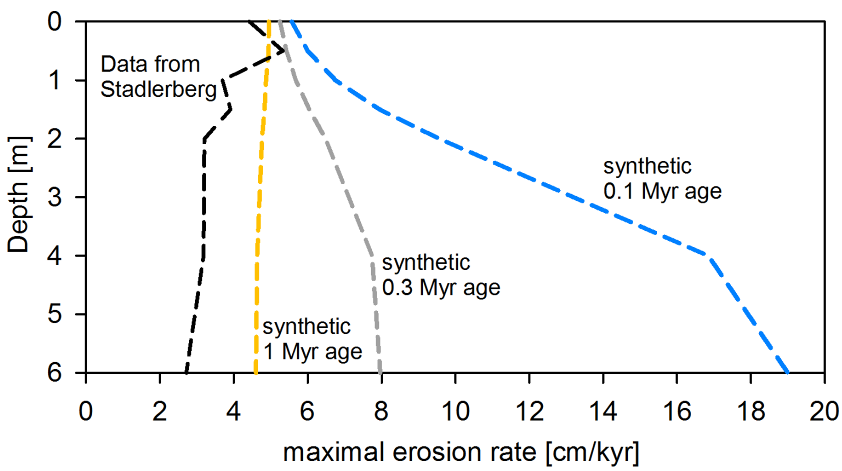

Fig. 15: Trend of the calculated maximum erosion rate along depth based on the three synthetic depth profiles with model ages of 0.1, 0.3 and 1 Myr (with a predefined erosion rate of 5 cm/kyr)

The rates for the Stadlerberg profile are calculated using data from Claude et al. (2017).

2.4 The Stadlerberg depth profile revisited

In this section, the Stadlerberg depth profile published in Claude et al. (2017) is critically assessed. First, the data, a check for steady state, their analysis and original interpretation are presented. Second, the original dataset will be re-calculated using the Hidy code and from the effects of changes in the initially chosen parameters will be shown. Finally, a brief conclusion is reached.

The Stadlerberg depth profile in Claude et al. (2017) is based on the ^{10}Be concentrations of seven sand samples. The concentrations range from $2.26 \pm 0.15 \times 10^4$ atoms/g for the lowermost sample to $10.34 \pm 0.43 \times 10^4$ atoms/g for the uppermost sample (Fig. 16). The data show an exponential decrease with depth. Furthermore, in the upper, shallow part of the profile at 1 m depth, a certain scatter, i.e. a deviation from an exponential profile shape, can be observed.

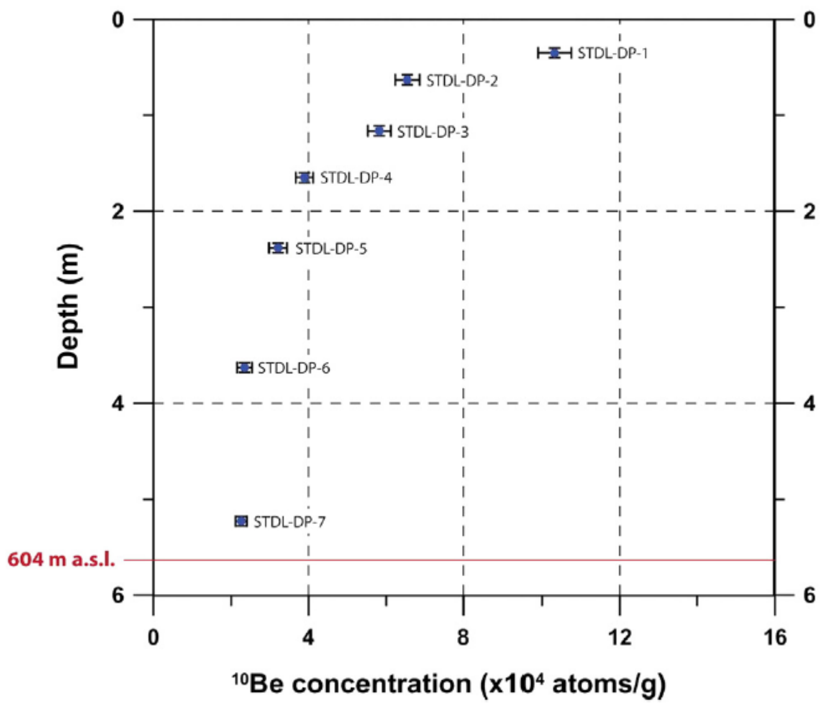

Fig. 16: ^{10}Be concentrations measured at the Stadlerberg site including the 1σ uncertainties plotted against depth

Claude et al. (2017)

Following the routines of Ruszkiczay-Rüdiger et al. (2016) and Viveen et al. (2012), the Stadlerberg depth profile is first checked for steady state by the trend of maximum erosion rate along depth. As explained above (Section 2.1.1), an infinite exposure time is set for each data point and Eq. (1) is solved for the erosion rate which is then at its maximum. As a result, the Stadlerberg depth profile shows a fairly constant maximum erosion rate of 3 cm/kyr for depths exceeding 2 m and some scatter of 3 to 4 cm/kyr for the uppermost 2 m (Fig. 15). According to Viveen et al. (2012) and Ruszkiczay-Rüdiger et al. (2016), the profile is in steady state as it is fully adjusted to its maximum erosion rate shown by its constant trend along depth.

Related to the first check of the profile for steady state is the approach of Ruszkiczay-Rudiger et al. (2018) to calculate the maximum age estimate possible determined by the depth profile approach. In other words, this obtained age can be straightforwardly interpreted as the minimum age for a saturated depth profile. For repetition, the approach of the ^{10}Be concentration for the lowermost sample in the profile towards the plateau, i.e. the production of ^{10}Be towards secular equilibrium, is modelled with increasing time (Fig. 17). The site-specific production of spallogenic and muogenic contributions scaled to the depth of 5 m (7.2, 0.015 and 0.045 at/g/yr and a density of 2 g/cm^3) was used. In accordance with Claude et al. (2017), the calculated maximum profile erosion rate of 50 m/Myr was used. The intersection of the steady-state concentration under the given maximum profile erosion rate with the linear part of the increasing production limb provides the maximum age up to which an age estimate can be meaningfully obtained (Fig. 17). The linear part of the increasing production limb is approximated by a line of 3 points, which can be manually adjusted for a better fit, resulting in different R^2 values for the regression (Fig. 18). A better approximation of the linear part of production results in a better R^2 value (closer to 1 which would be best possible). It also results in a lower maximum age for potentially successful age estimates based on depth profiles. According to Régis Braucher, who created this simple approximation and estimation of maximum ages, an R^2 value above 0.98 should be achieved. Following this rule of thumb, for the Stadlerberg site an age of 464 kyr could be successfully determined for a corresponding depth profile (given that the profile would not be saturated as the data clearly show). Therefore, the maximum reasonable minimum age is 0.45 Myr. However, this simple assessment of maximum ages does not consider the data quality (scatter, exponential trend, etc.) of the profile. Therefore, for profiles with a certain scatter such as that of Stadlerberg, one could also select the most conservative maximum age represented by the R^2 value of 1, which is 245 kyr. Consequently, a minimum age of 0.25 Myr considering the data scatter is more reliable than 0.45 Myr.

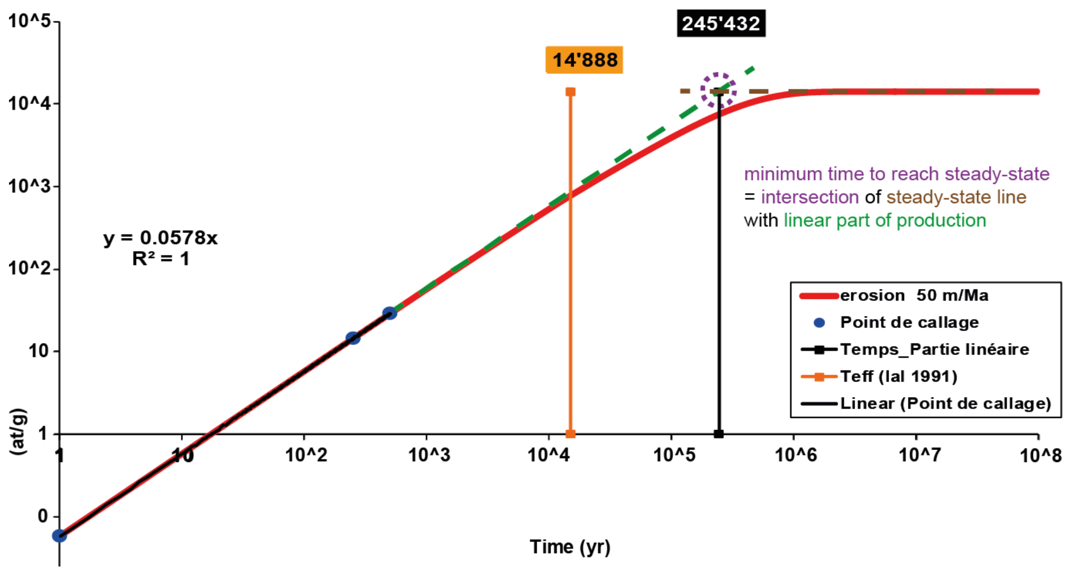

Fig. 17: Accumulation of ^{10}Be for the Stadlerberg site at a depth of 5 m and for an erosion rate of 50 m/Myr

Plot and analysis based on Régis Braucher, pers. comm. The double-logarithmic plot shows a fairly linear part – the production – followed by the constant concentration – the plateau – representing steady state. The maximum integration timescale for the lowermost sample can be approximated by the intersection of the fitted linear part with the plateau line. The intersection occurs slightly before steady state is reached.

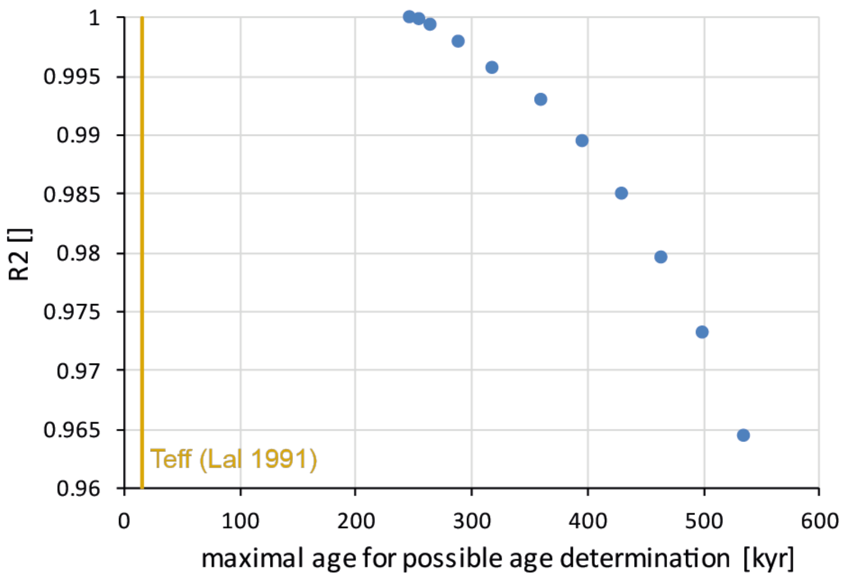

Fig. 18: Maximum age for possible age determination vs. R^2 value for the approximated linear part of production at a depth of 5 m for the profile of the Stadlerberg site (see Fig. 16)

The better the approximation (R^2 value closer to 1), the lower the maximum age where age estimates can potentially be resolved. It is up to the user to define the relevant R^2 value (Régis Braucher pers. comm.). By comparison, the effective integration timescale of Lal (1991) is reported which represents the integration timescale for surface samples.

In a next step, the profile presented from Stadlerberg is modelled by the Hidy code. The input parameters used for the Monte Carlo simulation are listed in Tab. 7. The most important input parameters are the constrained age interval of 1 – 3 Myr, the total erosion threshold of 75 – 110 m and the inheritance of 0 to 40'000 at/g (according to Claude et al. 2017). The version of the Hidy code used was 1.0, which was the first version of the code as presented in the paper of Hidy et al. (2010).

The authors of the paper reported age estimates of 1.86 Ma with 2.05 and 1.68 Ma as maximum and minimum ages representing the 2σ upper and lower boundaries (Tab. 8). The corresponding output figures from the Hidy code are shown as a screenshot from the paper (Fig. 19). The Gaussian-like shapes of the probability curves for the age seem to indicate a convergence of the solution space due to the forcing of the net erosion constraints. However, ages within the 1.65 to 2.05 Myr interval occur equally frequently. This observation is in line with the chi-squared age plot and similarly indicates that there is divergence in the solution space rather than convergence (as would be expected due to the application of the constraints in age and total erosion threshold). Furthermore, the simulations with the minimum chi-squared value of 4.6 (see Fig. 19) indicate a certain scatter in the data and deviations from a real exponential trend of the profile with depth.

Tab. 7: Table from Claude et al. (2017) showing the input parameters for the Monte Carlo simulation of Hidy et al. (2010)

Parameter	**Value**
Latitude (degree)	47.533
Longitude (degree)	8.446
Altitude (m)	610
Strike (degree)	0
Dip (degree)	0
Shielding correction factor	1
Cover correction factor	1
Uncertainty of ^{10}Be Half-life (%)	1
Local spallogenic production rate (at g^{-1} a^{-1})	7.18
Error in local spallogenic production rate (at g^{-1} a^{-1})	± 0.15
Depth of muon fit (m)	6
Error in total production rate (%)	5
Density (g cm^{-3})	1.8 – 2.3
χ^2 value	5
Number of profiles	100'000
Age (a)	1'000'000 – 3'000'000
Erosion rate (cm ka^{-1})	3 – 7
Total erosion threshold (cm)	7'500 – 11'000
Inheritance (at g^{-1})	0 – 40'000
Attenuation length (g cm^{-2})	160 ± 5

For our own calculations, the latest Hidy code version 1.2 with significant updates from Ruszkiczay-Rüdiger et al. (2016) in terms of i) updated muon production parameters of Braucher et al. (2011) and ii) incorporation of the Bayesian statistics was used. The updated muon production parameters do not significantly shift resulting age estimates. The Bayesian statistics are represented by the Bayesian most probable and 1σ/2σ lower and upper values. Using the same dataset and identical parameters, a re-calculation yielded a slightly younger age estimate of 1.78 Myr, but with a much larger 2σ range of 2.57 and 1.27 Myr. In Fig. 19, the 2σ confidence interval reported from the paper (green) and from our re-calculation (purple) are marked and illustrate the huge discrepancy between the two age intervals.

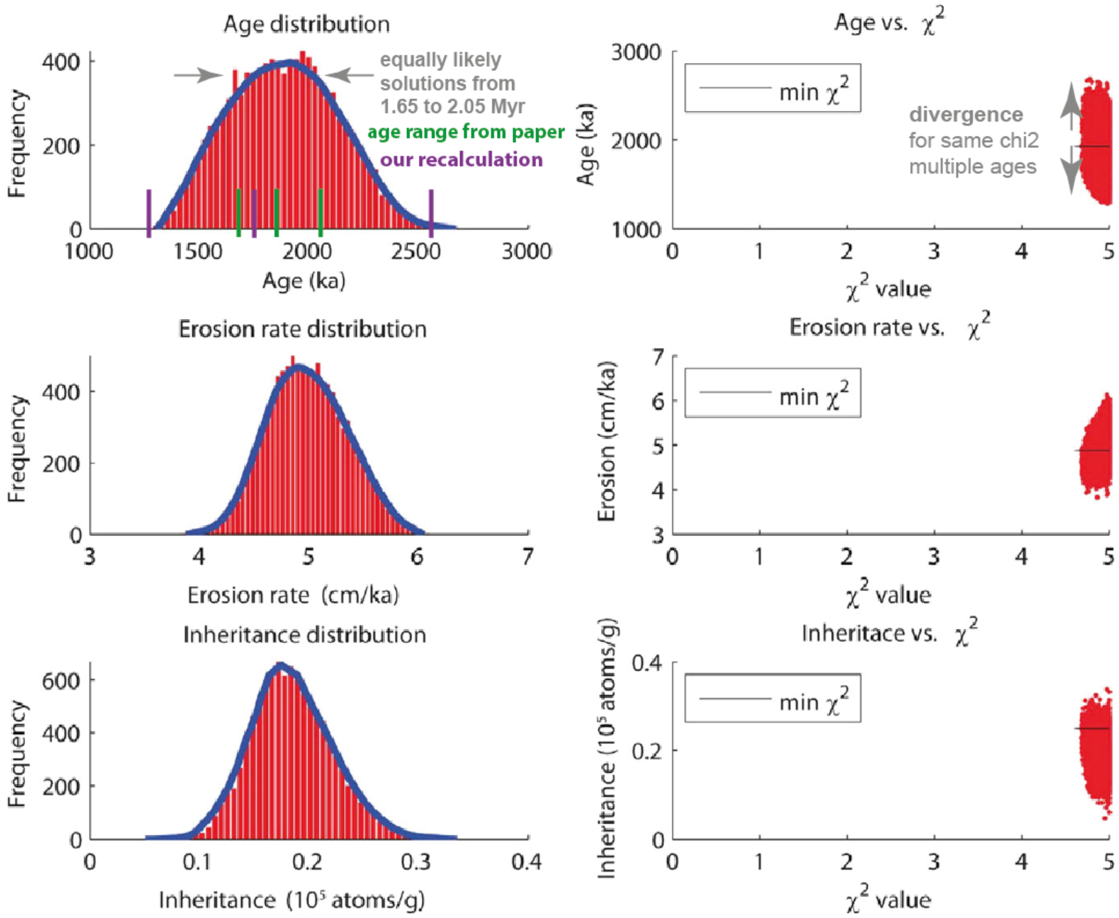

Fig. 19: Output plots from the Hidy code for the Stadlerberg dataset with applied net erosion constraints of 75 to 110 m

Claude et al. (2017). The figure indicates the output results in terms of age arefrom the paper and from our own calculations (see corresponding Tab. 6 for comparison). The minimum chi-squared value is 4.6 (see right panels).

A further re-calculation using a larger age interval of 0 – 5 Myr and no net erosion constraints yields an even larger age (2σ) interval of 3.12 and 0.08 Myr, but with a rather similar Bayesian most probable value of 1.79 Myr. As outlined by Ruszkiczay-Rüdiger et al. (2016), the Bayesian 2σ lower value can be taken as a minimum age in the case where the profile is in secular equilibrium. Given that several arguments for the Stadlerberg profile exist in favour of this, e.g. constant maximum denudation rates along depth, a comparison with synthetic profiles of similar erosion rates and the observed divergence in the solution space for unconstrained age modelling performed with the Hidy code, we conclude that the profile is in steady state.

Tab. 8: Output statistics for the simulation with the Hidy code of the dataset from the Stadlerberg profile

Claude et al. (2017). Our own re-calculation using identical parameters and another re-calculation but with a larger input age interval and no net erosion constraints.

	Age (kyr)	**Erosion rate** (cm/kyr)	**Inheritance** [10^4 at/g]
Results from Claude et al. (2017)			
Mode	1'857	5.0	1.9
Maximum	2'050	6.2	3.1
Minimum	1'680	3.9	0.5
Re-calculation using identical parameters			
Bayesian most probable	1'782.6	5.00	3.13
Bayesian 2σ-upper	2'573.7	6.58	3.94
Bayesian 2σ-lower	1'270.2	3.71	1.83
Re-calculation using same parameters, age interval 0 – 5 Myr, no net erosion constraints			
Bayesian most probable	1'793.5	4.89	2.09
Bayesian 2σ-upper	3'124.3	6.62	3.94
Bayesian 2σ-lower	85.4	3.70	1.40

Knowing now that the profile of the Stadlerberg data is in steady state, only minimum exposure ages (or maximum integration timescales under a specific profile erosion rate) should be presented. The relevant results from the synthetic profile, calculations of the maximum integration timescales and simulations of the measured profile with the Hidy code are summarised in Tab. 9. The interval of the different approaches for the minimum exposure ranges from 85 kyr for output of the Hidy code for the measured profile to 521 kyr for the synthetic profile. The observed pattern for low minimum ages for real profile data can be explained by the natural scatter in the dataset such as geological uncertainties including variability in the production (changing density of the sediment) and inheritance. Accordingly, the different minimum exposure age estimates are regarded as ranging from optimistic or rather unrealistic for synthetic, unscattered profiles towards realistic (maximum integration timescale) and even conservative for the measured data (no constraints in age and net erosion).

Further tests were performed to study the influence of constrained inheritance intervals for the simulations and the solution space. Tab. 10 and Fig. 20 show the results for different constrained inheritance intervals with the upper boundary ranging from 20'000 to 60'000 at/g. The lower range is represented by measured, recent river sands in Alpine catchments (Wittmann et al. 2007) and the upper range by catchments in the foreland (Norton et al. 2008). The different calculations show a clear trend towards higher age values with larger inheritance intervals. This behaviour can easily be explained by more decay time being available at higher ages and that in order to match the measured concentrations, a larger initial inheritance is provided (to allow decay over longer times). The plateau of equally frequently found ages with minimum chi-squared values extends with larger inheritance intervals. Because the entire solution space is also extended, the 2σ age interval becomes larger than the 95.4 % of all solution samples (corresponding to 2σ ranges) over a larger solution distribution.

Tab. 9: Summary of the previously discussed estimates for minimum exposure age for a depth profile scaled to Stadlerberg and site-specific profile erosion rate of 50 m/Myr

Method to estimate minimum exposure age for the depth profile at Stadlerberg site	**Age** (kyr)	**Comment**
Synthetic profile (1 Myr synthetic exposure time) Bayesian lower 2σ value, output of Hidy code	521	Optimistic/unrealistic (non-scattered data)
Mean integration timescale at depth of 5 m for an erosion rate of 50 m/Myr (R. Braucher, pers. comm.)	245 464	Realistic (when scatter in data) Optimistic (synthetic data, no scatter)
Re-calculation of the data from Claude et al. (2017) without constraints in age and net erosion	85	Conservative (relatively low due to scatter in data)

Tab. 10: Output statistics of the simulations with the Hidy code using the same dataset as above from Stadlerberg but with a larger age interval, no net erosion constraints and different inheritance interval

Re-calculation using the same parameters, age interval 0 – 6 Myr, no net erosion constraints	**Age** (kyr)	**Erosion rate** (cm/kyr)	**Inheritance** [10^4 at/g]
Inheritance interval of 0 – 20'000 at/g			
Bayesian most probable	571.4	4.76	2.00
Bayesian 2σ-upper	2'035.6	6.18	1.99
Bayesian 2σ-lower	22.7	3.37	1.15
Inheritance interval of 0 – 30'000 at/g			
Bayesian most probable	1'142.9	4.76	2.07
Bayesian 2σ-upper	2'563.0	6.47	2.96
Bayesian 2σ-lower	NaN	3.35	1.31
Inheritance interval of 0 – 40'000 at/g			
Bayesian most probable	1'857.1	4.76	2.19
Bayesian 2σ-upper	3'089.4	6.51	3.93
Bayesian 2σ-lower	NaN	3.41	1.39
Inheritance interval of 0 – 60'000 at/g			
Bayesian most probable	2'771.7	5.00	2.09
Bayesian 2σ-upper	4'068.7	6.73	5.88
Bayesian 2σ-lower	185.8	3.64	1.44

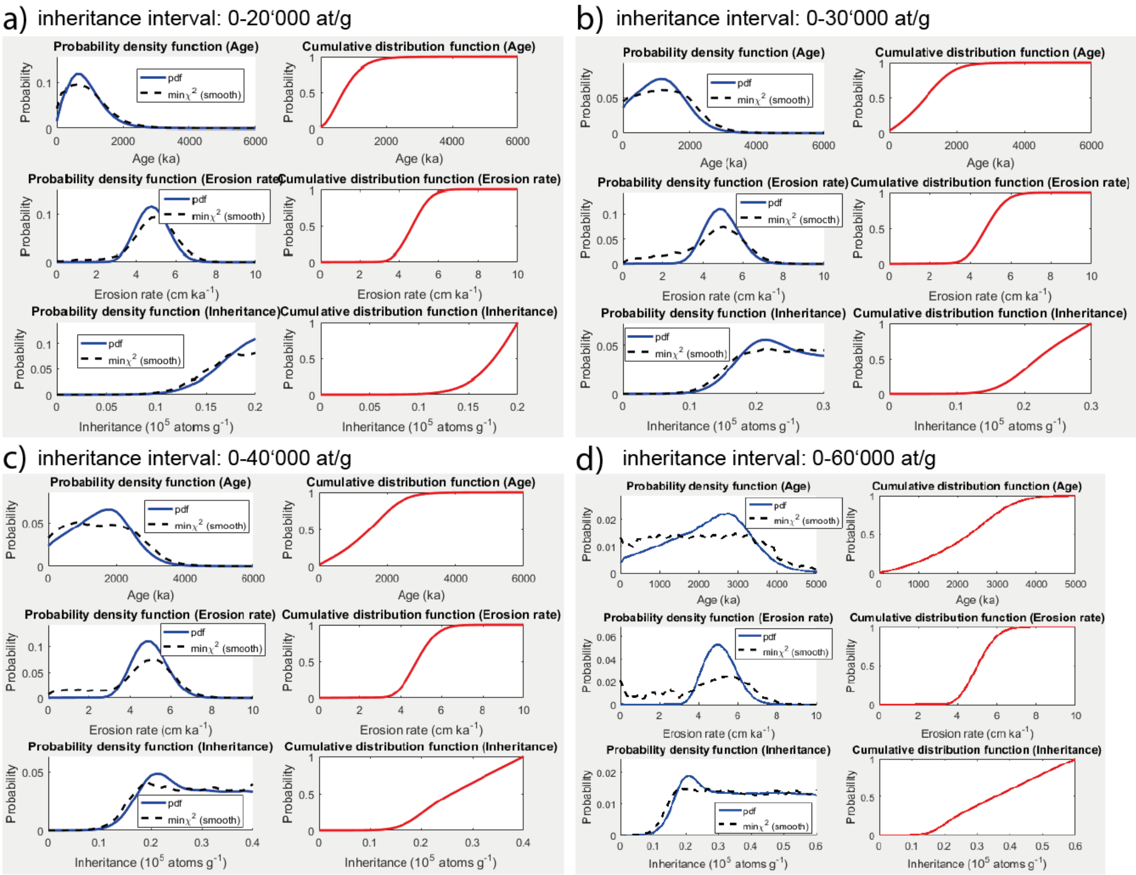

Fig. 20: Output plots for the Stadlerberg profile (see Tab. 8 for details of the chosen parameters) with different inheritances

For increasing inheritance constraints, the resulting age interval also becomes larger (see cumulative distribution function for comparison).

Therefore, the relationship between inheritance and resulting ages is straightforward: the higher the initial inheritance constraints (for the code) provided for the simulation are, the higher the inferred age will be in order to match the same measured concentrations. In Fig. 21, the measured data and the synthetic profile scaled to Stadlerberg and assuming a profile erosion rate of 5 cm/kyr (and no inheritance) are compared. The clear offset of the synthetic profile (no inheritance incorporated) to the measured data can be explained by the remaining or not-yet-decayed inheritance. Comparing the concentrations of both synthetic and measured profile at an equal depth of 5.2 m (Fig. 21), the remaining inheritance could be in the range of 8'000 at/g and is therefore significant for low concentrations at depths of 2 to 6 m but is rather insignificant for the uppermost 1 m of the profile (the production part is much more dominant). For the uppermost measured samples at a depth of 0.35 m, the 2σ error bar is roughly equal to the remaining inheritance. Assuming a simplified half-life of 1.4 Myr for the radioactive decay of ^{10}Be and based on exponential decay, the initial inheritance before deposition can be inferred (Tab. 11). Therefore, for depositional ages of 1.4 Myr and 2.8 Myr, initial ^{10}Be inheritances of 16'000 and 32'000 at/g, respectively, can be estimated. For example, the calculated initial inheritance of 32'000 at/g lies within the constrained inheritance interval of 0 to 40'000 at/g where the Monte Carlo simulation randomly selects values. Consequently, the resulting Bayesian 2σ-upper value is 3.089 Myr and again the assumed decay time of 2.8 Myr is part of this interval. To conclude, this simple quantification example explains why the choice of the initial inheritance interval (as code input) itself steers the direct age output of the Monte Carlo simulation. However, the entire discussion of inheritance is based on the fundamental assumption that inheritance is constant along depth (see Hidy et al. 2010). Knowing the initial inheritance before deposition is not possible using ^{10}Be alone as ^{10}Be decays over time and no other nuclide can be used to infer initial inheritance of ^{10}Be.

Finally, these considerations for evaluating the potential exposure durations of the depth profile reduce the depth profile from a 2D problem of the exponential curve to a 1D problem that simply deals with the radioactive decay of ^{10}Be for the bottom of the profile. As the Stadlerberg depth profile is in steady state and, with ^{10}Be, only one nuclide is available, no accurate age determination can be performed. A promising alternative might be measuring another nuclide, such as ^{26}Al, which would provide additional information about the decay time, i.e. burial dating (see later in this chapter).

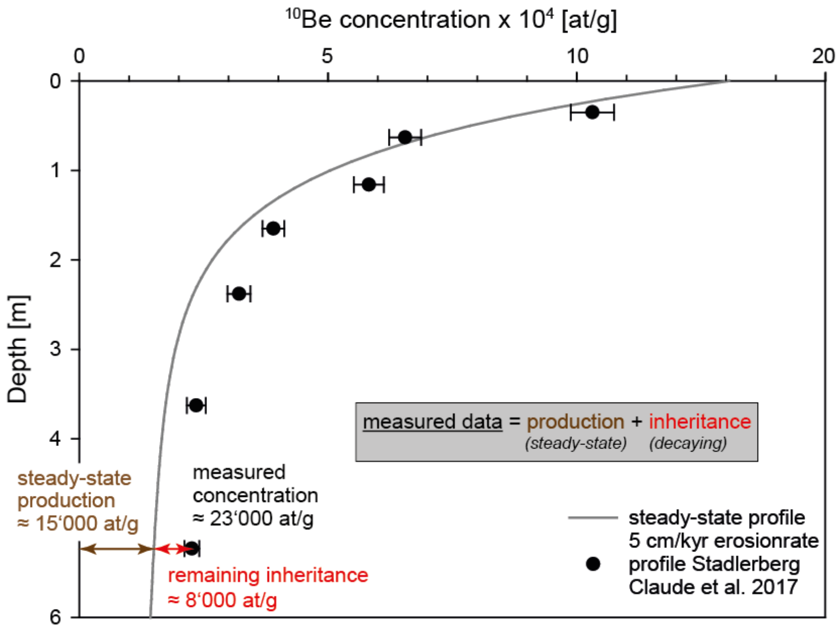

Fig. 21: ^{10}Be concentration plotted against depth with measured data from Stadlerberg and the synthetic profile scaled to the Stadlerberg site for an erosion rate of 5 cm/kyr, inheritance of 0 at/g and steady state

Claude et al. 2017. The clear offset between the synthetic profile and the data profile results from the inheritance which is not incorporated into the synthetic profiles. The offset cannot be explained by a higher erosion rate than 5 cm/kyr for the measured data. Comparing measured data and the synthetic profile allows the remaining inheritance to be roughly estimated as being close to 8'000 at/g.

Tab. 11: Back-calculation of today's inheritance compared to the initial inheritance with the (for the sake of simplicity) assumed half-life of 1.4 Myr for the radioactive decay of ^{10}Be

Note that present-day concentrations in river sands range from 10'000 to more than 40'000 at/g (cf. Wittmann et al. 2007).

Decay time [Myr]	**0.7**	**1.4**	**2.8**
Initial inheritance [at/g], before deposition	11'300	16'000	32'000
Decayed inheritance, measured	8'000	8'000	8'000

An additional test was performed again using the dataset of Claude et al. (2017) without any constraints in erosion rate and net erosion but age constraints of 0 – 3 Myr. Following Delmas et al. (2018), any model was graded acceptable with a chi-squared value situated between the smallest chi-squared values (chi-squared_minimun) and chi-squared_ minimun+1, because this range of solutions is considered as a mathematical substitute or proxy for the 1σ confidence interval (representing 68.3 % of all solutions). Note that the chi-squared value reported by the simulations is a reduced chi-squared value, i.e. normalised for the degrees of freedom. Thus, the solution space was illustrated sensu Delmas et al. (2018) by marking all solutions that had a chi-squared value within the interval of chi-squared_minimun and chi-squared_minimun+1 (Fig. 22). Checking the plots of age vs. probability reveals identical observations as seen above (Fig. 20) that minimum chi-squared values are equally frequent for multiple ages within 0 to 2.5 Myr, i.e. divergence in the solution space (Fig. 22A). This first observation is confirmed by the age-erosion plot in which the solutions of the 100 lowest chi-squared values (yellow points) stretch from 0.5 to ~ 3 Myr (Fig. 22B). Furthermore, almost the entire solution space is covered by blue points which are within the 1σ confidence interval. The latter observation is no surprise as the maximum chi-squared value allowed (input parameter) was set to 6 (in the mentioned paper '5') and the minimum chi-squared value found was 4.6.

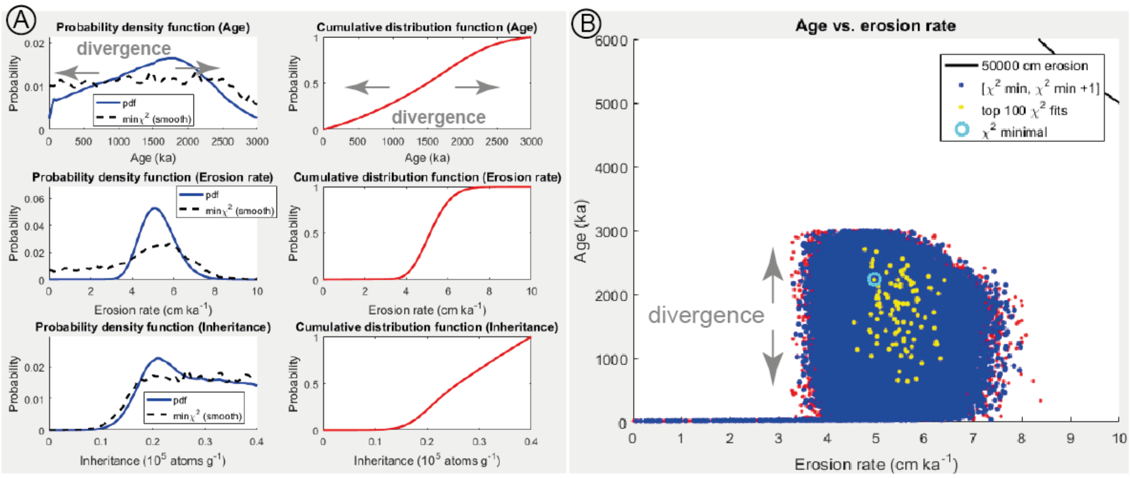

Fig. 22: Output plots from the Hidy code for the Stadlerberg dataset with no constraints in erosion rate and net erosion but constraints in age (0 – 3 Myr) which can be observed by the cut top of the solution space (at 3 Myr)

As it is not possible not to apply any net erosion at all, an extremely high value of 500 m net erosion was taken and thus does not constrain the solution space.

The comparison of all simulations for the Stadlerberg depth profile performed with or without constraints in age and total erosion threshold shows variable age values with wide 2σ confidence intervals within 0 and 4 Myr (Fig. 23). The only narrow 2σ confidence interval is reported by the authors of the paper itself but cannot be repeated as our own re-calculation showed. The re-calculation with applied total net erosion constraints suggests acceptable 2σ ranges, but the question remains how reliable the applied net erosion constraints are. Constraining the solution space by applying net erosion constraints strongly controls the final age and the corresponding 2σ confidence age interval. Unfortunately, the independent geological constraints for justifying the application of net erosion and age constraints are not provided by the authors.

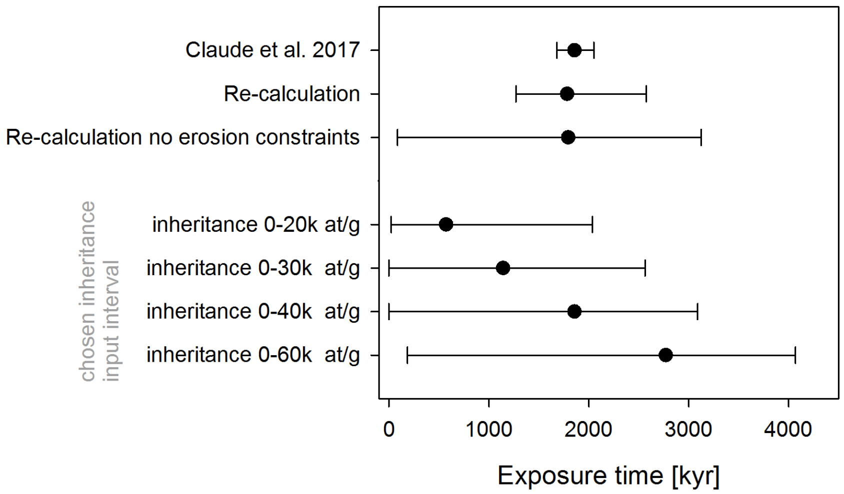

Fig. 23: Summary of the discussed age estimates and our own different re-calculations

Claude et al. (2017). The most striking observation is that the 2σ age intervals are much larger in all of our re-calculations than in the paper by Claude et al. (2017).

2.5 Conclusion for depth profiles, consequences and outlook

The literature review, comparison with synthetic depth profiles and thorough checking of the published depth profile from Claude et al. (2017) yield several findings or conclusions for the appropriate use of depth profiles. The lessons learned in the context of this chapter are presented in the following list.

- Depth profiles with cosmogenic nuclides are governed by production during exposure (age), the assumed constant erosion rate (surface lowering), radioactive decay (loss of nuclides) and density of the sediment (attenuation of the cosmic rays).
- An accurate age determination of depositional surfaces can be achieved as long as ^{10}Be concentrations have not yet reached steady state, with nuclide production and loss (decay + erosion) in equilibrium. Steady state is reached quickly at a high erosion rate (e.g. a few 100 kyr for 5 cm/kyr (50 m/Myr).
- If the profile has reached secular equilibrium, the long-term erosion rate and minimum exposure age (integration time) of the profile can be constrained. In the case where comprehensible, well-documented and independent geological constraints are available for erosion rate and total erosion threshold, they can be applied to the simulations and constrain the solution space. This might be an option for young profiles belonging to the Late Pleistocene but impossible for Middle and Early Pleistocene profiles.

Depth profiles can still be successfully applied when the measured data do not have a significant scatter and are carefully checked for steady state. Furthermore, in the absence of applicable geological constraints, the correct conclusions should be drawn, i.e. a robust profile erosion rate and minimum exposure age. However, the assumption of a constant erosion rate might be violated when erosion events or transient erosion rates are likely to have occurred, which is difficult to verify. If available geological constraints are applied, the proof and documentation of this independent evidence should be done rigorously so that it is possible to understand the constrained age intervals and resulting age interpretations.

As discussed above, high-profile erosion rates force the depth profile to steady state quite quickly. High profile erosion rates in Switzerland and in general throughout Middle Europe are common and probably due to climate. In particular, relatively high precipitation and temperatures provide ideal conditions for intense soil weathering and related erosion. Therefore, it is recommended to search for sites with a low profile erosion rate. If a high profile erosion rate has to be assumed, e.g. by attempting to date terraces in Middle Europe, relatively young, Late Pleistocene terraces should be selected. In Switzerland, Quaternary units that can potentially be dated successfully include the Niederterrasse and possibly also the youngest Hochterrasse deposits (younger than 0.2 Myr). However, the existing literature for relevant sites as well as findings from other dating methods should be carefully considered to check expected age ranges. Calculating the maximum possible definable age for reliable age estimates (method from Ruszkiczay-Rudiger et al. (2018) and R. Braucher, pers. comm.) should give useful insight.

For the reasons described in this chapter, it was decided in the present study not to apply depth-profile dating to any Northern Swiss foreland Deckenschotter sites. Consequently, sedimentary terraces from the Swiss Deckenschotter will be dated in the following using burial/isochron burial dating (see next chapter). Using a second nuclide allows more parameters to be constrained than is possible using a single nuclide.

3 Burial dating

3.1 True/simple burial dating

Dating buried sediments using cosmogenic nuclides relies on their time-dependent, differential decay in the subsurface, where samples are largely shielded from cosmic radiation (Klein et al. 1986, Nishiizumi et al. 1986). Burial dating requires the analysis of at least two nuclides, as there are two unknowns in the sample's history: first, the time of exposure and, second, the time of burial itself (Granger 2006, Granger & Muzikar 2001, Nishiizumi et al. 1986). ^{26}Al and ^{10}Be are a favoured combination pair for burial dating:

Both nuclides are produced in quartz, which is ubiquitous and highly resistant to weathering

- ^{26}Al and ^{10}Be show similar geochemical behaviour, which simplifies sample preparation.
- The surface production rates are linearly proportional in the range of regular attenuation lengths (Argento et al. 2013, Brown et al. 1992, Gosse & Phillips 2001).
- The isotope half-lives deviate by a factor of two (^{10}Be $\tau 1/2$ = 1.387 ± 0.012 Ma and ^{26}Al $\tau 1/2$ = 0.705 ± 0.024 Ma; Chmeleff et al. (2010), Korschinek et al. (2010), Nishiizumi (2004).

^{26}Al and ^{10}Be are built up at well-constrained production rates at the earth's surface. While local production rates vary depending on altitude, geomagnetic latitude and shielding (Nishiizumi et al. 1989, Stone 2000), the cosmogenic surface production ratio is assumed to be stable at a value of around 6.75 at/g_{Qz}/yr, regardless of the sample's geographic location and altitude (Balco & Rovey 2008, Kubik et al. 1998, Nishiizumi et al. 1989). The recently investigated production ratio at depth of 8.4 at/g_{Qz}/yr is suggested to be significantly higher (Akçar et al. 2017, Braucher et al. 2013). However, production ratios higher than 6.8 have been a matter of debate (see extended discussion in Section 6.1.3). When terrestrial rock is covered and therefore barely affected by cosmic ray bombardment, the nuclides begin to decay, with ^{26}Al decaying approximately twice as fast as ^{10}Be. The decay process leads to a gradual drop of the $^{26}Al/^{10}Be$ ratio, providing key information with respect to the sample's burial time. Nuclide ratios measured in buried samples and related to the initial surface production ratio via the law of decay allows burial ages to be calculated (Eq. (3). Equation (3) presented below only applies to deep burial, where post-burial production by muons is negligible. For all other situations, post-burial production has to be subtracted before calculating the burial ages.

$$t_b = \frac{-ln(\frac{R_M}{R_{init}})}{(\lambda_{26} - \lambda_{10})} \qquad \text{Eq. (3)}$$

Where t_b is the burial duration equal to the age of sediment deposition, $\lambda_{26,10\ are}$ the decay constants of ^{26}Al and ^{10}Be, and R_M, R_{init} the measured and initial ratio of ^{26}Al and ^{10}Be.

Traditionally, burial dating was applied to sediments that are shielded from production by cosmic rays by a thick layer of water covering sediments such as lakes (Kong et al. 2009) or rock as in caves (Dehnert & Schlüchter 2008, Granger 2014, Granger 2006, Granger & Muzikar 2001). The fundamental assumption behind this is that the sediment experienced a simple exposure history, which means that the nuclide concentration of the sediment derived from erosion in the sourcing landscape was at steady state prior to burial. Further, the sample from such a setting is then buried rapidly and deeply, i.e. by several tens of metres depending on the local erosion rate, where post-burial production by muons can be ignored (Fig. 24). However, when there is a significant post-burial production due to a shallow burial depth, the nuclide ratios are raised. Shallowly buried samples will always appear younger than their true age. For samples with significant post-burial production, the simple burial dating method therefore indicates a minimum burial age. A burial age assumes one period of burial after exposure at the surface. In principle, the age of a deposit can be determined with a single sample (several hundred grams of sand or an amalgamated sample of > 50 clasts, cf. Granger (2006). Nonetheless, analysis of several samples would substantiate the underpinning of the determined age.

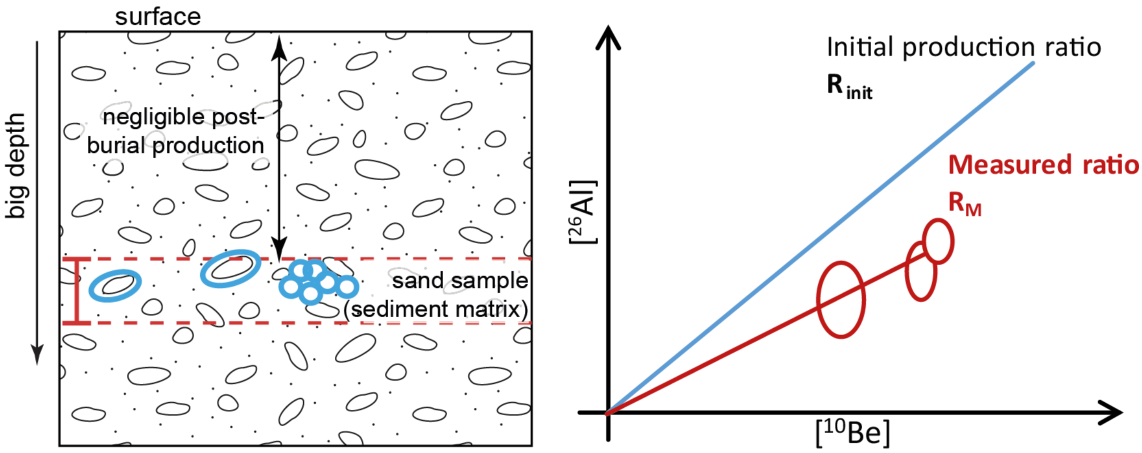

Fig. 24: Illustration of the principle of true burial dating at outcrop and on the ^{26}Al and ^{10}Be plot

A graphical solution for the age determination from burial dating is represented by the exposure-burial diagram or exposure-erosion plot, often referred to as a "banana" plot (Fig. 25). The latter attribute comes from the "steady-erosion island" (Lal 1991) enclosed by the two endmembers "steady erosion" (production and erosion > 0) and "constant exposure" (production, no erosion) resembling the shape of a banana. The exposure-erosion plot shows the ^{26}Al/^{10}Be ratio as a function of the ^{10}Be concentration normalised to sea-level-high latitude, i.e. the ^{10}Be concentration is divided by the source production rate. Due to this normalisation, samples from different altitudes and geographical positions can be compared. The two curves "constant exposure" and "steady erosion" define an upper limit to the ^{26}Al/^{10}Be ratio. The steady-erosion island is populated by samples that have a finite exposure age but are also eroding. Assuming that they have not been previously buried, all samples from the surface are expected to plot along one of the two curves or within the steady-erosion island. Once the samples from the surface are rapidly buried, they travel downwards, parallel to the dashed lines, i.e. towards smaller ratios and ^{10}Be concentrations resulting from the afore-mentioned differential decay of ^{26}Al and ^{10}Be (see Fig. 25).

The age range of burial dating for ^{26}Al and ^{10}Be is between 0.1 and 5 Myr (Granger & Muzikar 2001). The lower limit is mainly given by the experimental measurement error in the order of 2 – 4 % at the AMS. The upper limit is set because very old samples have very low nuclide concentrations which might be difficult to measure.

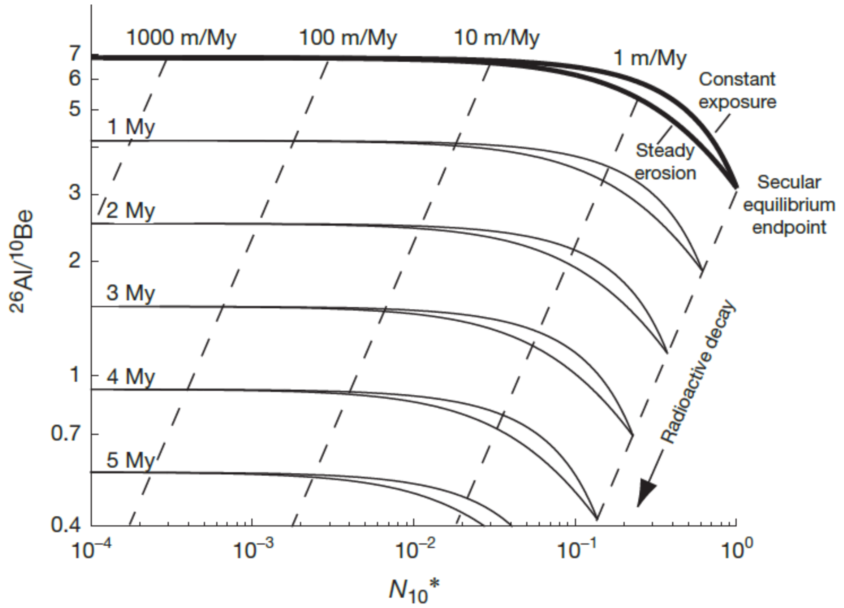

Fig. 25: Exposure-burial diagram

Modified from Dunai (2010). The so-called banana plot (see Section 5.3), showing $^{26}Al/^{10}Be$ against ^{10}Be expressed as N10* (normalised to the saturation concentration, i.e. local production rate times the mean half-life). Rocks at the surface will plot on the steady erosion or constant exposure lines. The position on the line depends on the erosion rate at the source, calculated here for rocks with a density of 2.6 g/cm^3 and labeled in units of m/Myr. ^{26}Al and ^{10}Be in rocks that have been deeply buried will undergo radioactive decay parallel to the dashed diagonal lines. Samples from the same sediment deposit should plot along the same burial line.

As mentioned earlier, simple burial dating requires deep burial, i.e. post-burial production can be ignored. Depending on the local erosion rate, samples buried within less than ~ 30 m beneath a surface or slope (Granger & Muzikar 2001) are affected by cosmogenic production due to muons with effective attenuation lengths of 1'500 and 4'320 g/cm^2 (Braucher et al. 2003). Due to their weak attenuation at depth, muon production adds only a minor component to the nuclide concentrations. The spallogenic production with effective attenuation lengths of 160 g/cm^2 working in the uppermost 3 – 4 m represents a much stronger production pathway and thus adds a major component to the nuclide concentration. Nevertheless, post-burial production due to muons at greater depths (a few tens of metres) and a low erosion rate could likewise increase the nuclide concentration of the sample. Because post-burial production increases the $^{26}Al/^{10}Be$ sample ratio higher than it would otherwise be, the calculated age of shallowly buried samples will always appear younger than their true age. Samples with a significant post-burial production therefore provide only a minimum burial age.

A maximum burial age can be calculated by quantifying the highest amount of post-burial production the samples could have experienced in an erosional setting. Post-burial production reaches a maximum based on the assumption that the samples have remained buried at the same depth, thus the local erosion rate has remained zero. However, this approach assumes that no sediment was added after burial.

3.2 Isochron burial dating

An elegant way to overcome the problem of unknown, unquantifiable post-burial production in shallowly buried sediments is isochron burial dating (Erlanger et al. 2012). Isochron-burial dating is a variation of traditional or true burial dating because the elapsed time, as reflected in the measured nuclide concentrations, is determined by the difference between the two half-lives. Isochron burial dating further differs from true burial dating by explicitly allowing a certain post-burial production because the history is the same for both nuclides and can be corrected for (Fig. 26). Because the exact value of the post-burial component is not important, shallower burial depths, e.g. a few metres, are possible. Furthermore, it also removes the requirement for density determination in the field and considerations of how density in the sampled profile changes over time. The latter is a crucial requisite that is necessary for depth profiles.

In contrast to true burial dating, several samples are required (Balco & Rovey 2008). The underlying principle behind an isochron is making use of samples that have had significantly different pre-burial histories, i.e. different quantities of inheritances (different source erosion rates in the landscape or different production rates reflected due to different altitudes). ^{26}Al and ^{10}Be are measured in a variety of samples from the same stratigraphic horizon no matter how complicated the burial history was (Erlanger et al. 2012). Consequently, the depositional age is identical for all samples and thus isochron. Typically, several individual fist-sized clasts (ideally of various quartz-bearing lithologies) or sediment samples (sand or ~ 30 – 50 amalgamated clasts) are collected along a single stratigraphic horizon. The measured nuclide concentrations will ideally plot along a line (Fig. 26). Samples that have experienced multiple episodes of burial will plot below the isochron and can be excluded from the following regression analysis. Samples that plot above the initial production ratio line can be excluded because ratios higher than present-day are likely to be a result of measurement errors (see Section 6.1.2). A lengthy discussion on this topic can be found in Braumann et al. (2018).

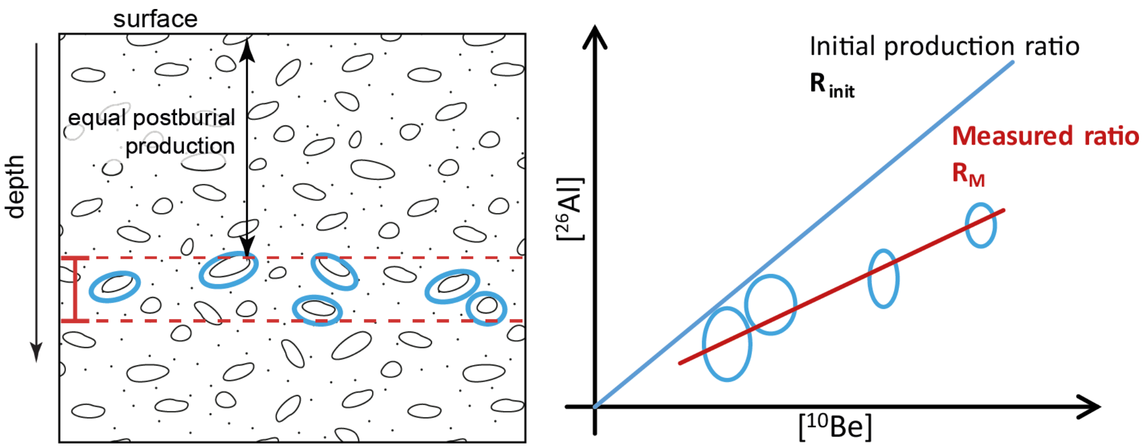

Fig. 26: Illustration of the principle of isochron burial dating for sampling and its consequences for the ^{26}Al-^{10}Be plot

The ^{26}Al/^{10}Be ratio at the time of burial (initial ratio) is assumed to be 6.78:1 at/g_{Qz}/yr at the surface, being constant for all latitudes and altitudes (Balco & Rovey 2008), or up to 8.4 at/g_{Qz}/yr at depth (Akçar et al. 2017). The latter value is results from the higher ^{26}Al production at depth than that of ^{10}Be (Braucher et al. 2013, Braucher et al. 2011). Akçar et al. (2017) postulate that glacial erosion removing rock from a depth of a few metres and thus sourcing clasts with a higher initial production rate could explain the measured higher nuclide ratios. However, this issue described in the quoted paper is not as clear as presented and will be further discussed in Section 6.1.3.

As pre-burial (inherited) nuclides accumulate according to the surface production rate ratio of 6.75, ^{26}Al concentrations vs. ^{10}Be concentrations for all samples should fall on a line. After burial, the concentrations again fall on a line whose slope is controlled by the difference in the decay rates. The difference between the two lines (isochrons) can be converted into the burial age (for details see Balco et al. 2013, Balco & Rovey 2008, Erlanger et al. 2012). A regression analysis of the measured ^{10}Be and ^{26}Al concentrations yields the slope of the regression line, which is the measured ratio. The isochron burial age cannot simply be calculated using Eq. (3). For this purpose, an iterative procedure is required to remove the post-burial production.

3.3 From geological samples to nuclide concentrations

The procedure for acquiring geological samples at outcrop of Quaternary deposits and their subsequent treatment in the laboratory to obtain a sand-sized sample is explained at the beginning of this section. The challenges of measuring low nuclide concentrations will be discussed afterwards. Because of these challenges, the cleaning routine of samples is of high importance, and systematic tests using two common procedures were carried out (see Appendix A). Based on these tests, the selected cleaning protocol is presented. The extraction of ^{26}Al and ^{10}Be from clean quartz and the determination of the corresponding nuclide concentrations is described at the end of this section.

3.3.1 Acquiring geological samples and quartz purification

Successful isochron burial dating depends on the chosen outcrop and the related samples. Qualification criteria for the selection of a specific outcrop are listed in Chapter 3 "Sampling sites". Typically, at the base of a 10 – 20 m high artificial outcrop wall consisting of an in-situ deposited, non-deformed outcrop, an accessible stratigraphic horizon is selected for sampling. The stratigraphic horizon should contain a variety of clasts and separate sand lenses or gravels with a sandy matrix. Geological samples should vary in terms of different parameters such as shape, lithology and grain-size fraction to increase the potential for a wide spread in the pre-burial nuclide data, which is required for a meaningful regression analysis (Akçar et al. 2017, Erlanger et al. 2012). The largest contribution to a sample's spectrum comes from several samples in pebble to small-block size. As shape is mostly similar in glaciofluvial sediments, i.e. sub-rounded to well-rounded, the shape parameter cannot be considered for a huge potential in terms of different erosion processes and hence nuclide concentrations. ^{26}Al and ^{10}Be are extracted from quartz and thus the sample lithology should be quartz-bearing. While sampling, the quartz content should be estimated and should not be lower than 10 %; otherwise the sample should be larger. Larger samples, however, complicate sample handling and increase the use of acids for quartz purification. For example, a typical pebble sample with dimensions of 10 × 7 × 7 cm (width, depth, height) has a simplified rectangular volume of 490 cm^3 and a mass of 1.3 kg (density 2.7 g/cm^3). Assuming a quartz content of 10 %, only 130 g of impure quartz is left. Due to subsequent cleaning, the quartz content can drop by 50 % and therefore only 65 g of quartz remains, which is sufficient for the analysis of low nuclide concentrations. Consequently, lithologies such as vein quartz, quartzites, granites, diorites, sandstones/conglomerates, and quartz-porphyry should be targeted for sampling.

Besides sampling single pebbles or blocks, the amalgamation of several small samples is preferred because the smaller grain-size fraction might inherit a different erosional signal than larger clasts such as pebbles (Puchol et al. 2014). The preferred lithology is vein quartz, which has a quartz content close to 100 %, but granites might also be an option. The minimum number of amalgamated small clasts is commonly thought to be 30 to 50 pieces (Repka et al. 1997). Besides pebbles, sands from a sand lens can also be amalgamated representing a single sample with an inheritance presumably different from that of clasts. Sands sampled from Quaternary deposits commonly consist of mainly carbonates in the Northern Alpine foreland, and therefore the sampled mass should consist of at least a few kg.

All samples are photographed with a scale in-situ in the outcrop wall. In the laboratory, the width, depth and height of the samples are measured, the lithology is determined, and the sample is photographed again. For the pebbly samples, determination of the lithology of the samples could deviate from the initial estimate in the field. Therefore, samples will be selected for further processing after the second lithology determination.

Selected samples are cut into 2 – 3 cm pieces by a rock saw. The cut pieces are put into a Teflon vessel for fragmentation by high voltage using SelFrag®. Starting with the lower high-voltage range, electric shocks reduce the pieces to coarse sand particles and further to medium-sized sands. In contrast to a hydraulic brake or disc mill, the major advantage of this fragmentation procedure is the large sample throughput and lack of dust distribution since the process takes place in water. The sand samples are then wet-sieved to a grain-size fraction of 630 to 250 µm.

The sand samples are transferred to bottles and subsequently cleaned of mineral phases other than quartz. First, a HCl treatment is performed to remove carbonates and oxides. Second, multiple (6 – 8) cycles with weakly concentrated HF (~ 5 %) are applied. Before the second-last HF cycle, two cycles of Hot Phosphoric Acid are applied. For details of this method, see Appendix A and Mifsud et al. (2013). After this routine, the sample should be clean and consist of pure quartz. Before selecting the samples for the extraction of ^{26}Al and ^{10}Be, a first estimate of the total Al content should be performed using an ICP-MS (see the Al Quick Test, Appendix A).

3.3.2 Challenges for measuring low nuclide concentrations in Alpine samples

The two nuclides of interest for isochron burial dating, ^{10}Be and ^{26}Al, are measured against their related stable isotopes ^{9}Be and ^{27}Al. Natural ^{9}Be is not commonly abundant in rocks sourced from the European Alps (but can be present in samples from the Himalaya, cf. Lupker et al. (2012). Therefore, the only source of ^{9}Be comes from a carrier material whose ^{9}Be content is very well-known (carrier material from GFZ Potsdam, H. Wittmann pers. comm.). By adding only a minimal amount of a very clean ^{9}Be carrier (with a negligible ^{10}Be concentration), very low ^{10}Be/^{9}Be ratios can be obtained. However, measuring ^{26}Al is different because ^{27}Al is the third most frequent element on earth and is also abundant in various mineral phases, e.g. feldspars, micas, amphiboles and in the related rocks, granites, gneisses and sandstones.

High ^{27}Al concentrations in the analysed quartz result in low ^{26}Al/^{27}Al ratios, which is challenging for the later AMS measurements. Depending on the actual ^{26}Al concentration, the ^{26}Al/^{27}Al ratios can be close to the detection limit. Furthermore, the few ^{26}Al atoms are inside a large amount of sample material which requires long measurement times. Previous studies (Akçar et al. 2017, Ruszkiczay-Rudiger et al. 2018) have shown that the ^{26}Al concentrations of Alpine pebbles and sands from the Pleistocene are very low both due to their high age (long decay time) and their low initial concentration (due to presumably poor initial exposure as a result of shielding by ice and/or fast erosion processes). Therefore, quartz samples have to be extensively cleaned in order to have a low ^{27}Al content; a recent study by Akçar et al. (2017) suggested less than 30 – 50 ppm. For tests of the most effective cleaning scheme, see Appendix A.

3.3.3 Cosmogenic nuclide extraction and measurements

This sub-section describes the transformation from a pure quartz sample low in ^{27}Al into a target ready to be measured by AMS. The purified quartz samples were processed following the protocol described in von Blanckenburg et al. (1996). An aliquot of 60 to 70 g of the sample with pure quartz is taken, spiked by a minimal amount of the ^{9}Be carrier (GFZ carrier, Hella Wittmann pers. comm.) and dissolved under a hood by concentrated HF. After fuming off the fluorides with HNO_3, aqua regia and HCl, the sample is centrifuged, and an aliquot is taken to measure the total aluminium content (Fig. 27). The sample is cleaned by a series of ion-exchange chromatography using a resin in columns and pH-sensitive reactions. Adding the sample to the anion column leads to the removal of anions such as iron, etc. The aluminium column separates aluminium from the rest of the sample. The following cation column (oxalic column) traps Be within the resin and is further eluted as pure Be. Ph-sensitive precipitations of the Al and Be samples formed as hydroxides and were transformed to AlO and BeO by heating them in an oven. The resulting powder is then mixed with copper (for AlO) and niobium (BeO) and pressed to Al and Be targets, respectively.

The ^{26}Al and ^{10}Be analysis were both performed at the 0.5 MV AMS TANDY facility at LIP ETHZ (Christl et al. 2013, Müller et al. 2015). The measured $^{10}Be/^{9}Be$ ratios were normalised using the ETH AMS standard S2007N ($^{10}Be/^{9}Be = 28.1 \times 10 - 12$ nominal, Christl et al. 2013), calibrated relative to standard 07KNSTD (Nishiizumi et al. 2007), which is consistent with a ^{10}Be half-life of 1.387 Ma (Chmeleff et al. 2010, Korschinek et al. 2010). All ^{10}Be samples were corrected for a procedural blank using the weighted mean of $(5.29 \pm 2.08) \times 10 - 15$ (2σ, n = 9), mainly representing the $^{10}Be/^{9}Be$ ratio of the carrier solution. The blank error and analytical uncertainties were propagated into the reported final ^{10}Be concentrations.

The measured $^{26}Al/^{27}Al$ ratios were normalised relative to the ETH AMS standard ZAl02 (nominal $^{26}Al/^{27}Al = 46.4 \times 10 - 12$) calibrated relative to standard KN01-4-1 (Nishiizumi 2004), which is consistent with a ^{26}Al half-life of $(0.705 \pm 0.024) \times 10^{6}$ yr. No procedural blanks were prepared. ^{26}Al contamination during sample preparation in the lab is assumed to be negligible. After each ^{26}Al AMS measurement, the measured $^{26}Al/^{27}Al$ ratios were background-corrected for a constant ^{26}Al background counting rate, which was determined independently (see Appendix D). The error of the background counting rate and analytical uncertainties were propagated into the final reported $^{26}Al/^{27}Al$ ratios. The uncertainty of the background correction is conservatively set to 25 % (incorporated in data analysis). For details of blank correction, see Appendix D.

To calculate the ^{26}Al concentrations in the samples (using the $^{26}Al/^{27}Al$ ratio determined by AMS), the ^{27}Al concentration must be determined. The ^{27}Al concentrations were determined using inductively coupled plasma mass spectrometry (quadrupole ICP-MS) at the Institute of Geochemistry and Petrology of the Earth Sciences Department, ETH Zürich. Initially, the Al concentration of each sample was determined by a standard-sample-bracketing method (see Appendix A), in which the ^{27}Al signal intensity of a diluted sample solution (~ 2 % HNO_3 matrix) is compared to intensities of standards with known Al concentrations and blank solutions. The accuracy of the Al concentrations determined by this method is insufficient for the purposes of the project (~ 30 % 1σ, the so-called Al Quick Test, see Appendix A.1). However, the measured concentrations are well suited for a more refined ^{27}Al concentration determination using a standard addition method. In this method, four aliquots of sample solution are taken, and varying amounts of standard solution are added to the aliquots before additional dilution with 2 % HNO_3. The concentrations determined by standard sample-bracketing allow the calculation of the ideal relative sample and standard amounts in the aliquots for the standard addition method. The blank-corrected ^{27}Al signals of the aliquots are then combined with the individual weights of the sample and standard solutions added to each aliquot and, together with their total solution weights, the Al concentration of the original sample solution can be estimated via a least-squares fit of the data (script written in Mathematica (C. Maden, pers. comm.). This method does not require all aliquots to contain the same amounts of sample solution and to have the same total solution weights, which would be required if the data were evaluated via a linear regression of blank-corrected signal intensity vs. amount of Al standard added to the aliquot. The obtained concentrations were back-calculated using the exact weights of the different dilution steps. The uncertainty of the measurement has been determined to be not better than 3 % and is propagated into the ^{26}Al concentrations.

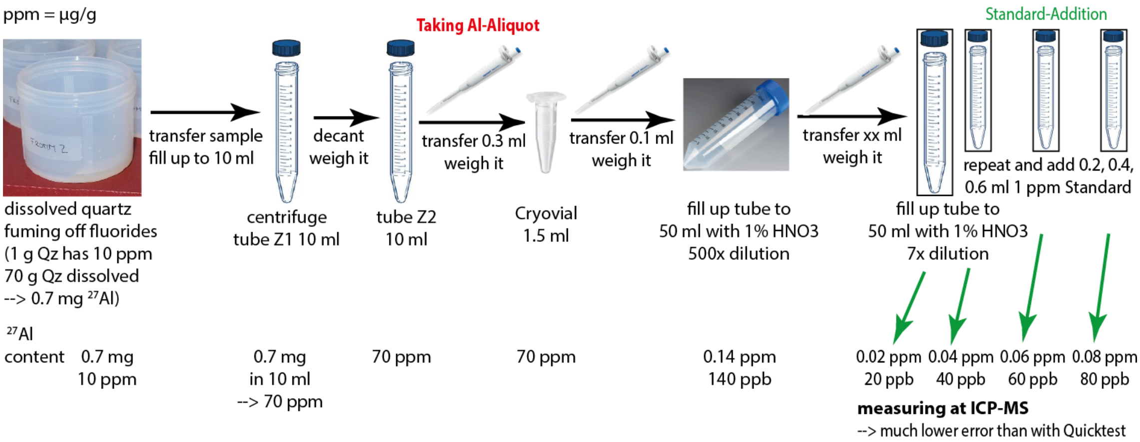

Fig. 27: Procedural description of the method of standard bracketing for Al determination using ICP-MS

This method allows a very low uncertainty of 3 % to be obtained, and thus much lower than the routine applied for the Quick Test by alternatingly measuring the sample, standards and blanks (uncertainties in the order of 10 to 30 %).

3.4 Age modelling of $^{26}Al/^{10}Be$ data for isochron burial dating

Unlike traditional/simple burial dating, the age of the sampled stratigraphic horizon is not calculated from a single sample but from a dataset with at least 2 – 3 sample numbers, preferably more. For a larger dataset with a significant spread between individual samples, the results for age modelling can be much better consolidated.

Due to the scatter typical for measurements of geological samples, the samples plotted in the ^{26}Al-^{10}Be diagram must be regressed to establish the specific slope and y-intercept. Knowing the slope of the regression line yields the measured ratio which can be used to calculate a burial age. The intercept with the y-axis depends on the post-burial production and can be used to check the plausibility of possible post-burial production under erosion rates typical for the environment at burial (Granger 2014).

The linear regression analysis for a scattered dataset must consider both uncertainties from the x- and y-axes. Thus, the regression analysis should not be restricted to fit a line through the mean datapoints (as the linear regression in Excel does) but also through the 1σ uncertainty range of them. The two most frequently used calculation algorithms are the Matlab code provided by D. Granger (called the "Granger code" hereafter and described in Erlanger et al. (2012), Granger (2014) and the Matlab code described in Bender et al. (2016) (called the "Bender code" hereafter). Both modelling codes provide an error-weighted regression analysis of isochron data and deliver the desired parameters of slope and intercept. In this study, both codes will be used for data analysis and age determination. In the following, the differences and similarities are discussed in detail.

3.4.1 Age modelling using the method of York (Granger code)

Commonly, linear regression is performed after the method of York (1968) that accounts for uncorrelated errors in both ^{26}Al and ^{10}Be. In York, least-squares linear regression, the slope and intercept values are assumed to be Gaussian, independent and uncorrelated. D. Granger (University of Purdue, USA) developed a Matlab code using a Monte Carlo routine simulation to iteratively calculate an isochron burial age (Erlanger et al. 2012, Granger 2014).

In the following, the calculation steps are briefly repeated and illustrated in Fig. 28 (for more details see Erlanger et al. (2012). The relevant input parameters for the code are the ^{26}Al and ^{10}Be data, the latitude/longitude and the elevation of the (assumed) source area. To simplify equations and calculation steps, the measured data are normalised, i.e. divided by the production rate of the indicated source area site times the radioactive mean life (cf. Granger 2014). The production rate itself is scaled according to the Lifton-Sato-Dunai (LSD) scheme (Lifton et al. 2014). This scheme considers varying production over time due to geomagnetic variation in contrast to the scaling scheme of Lal/Stone (Stone 2000) with constant nuclide production.

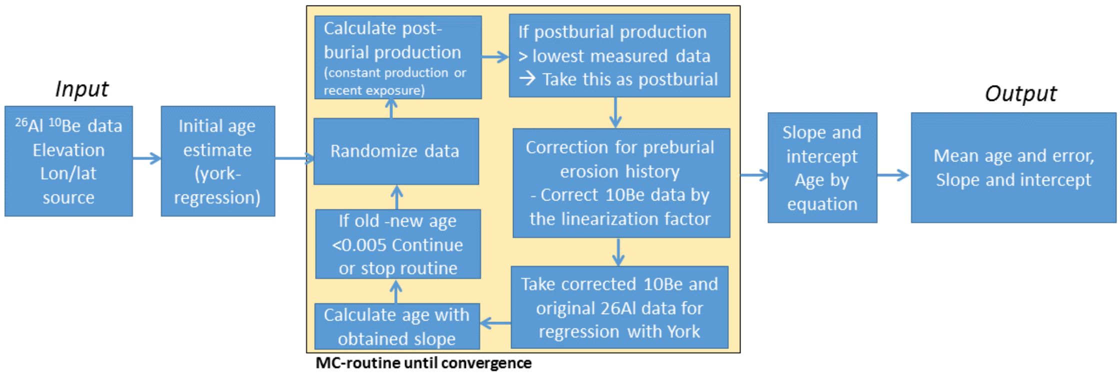

Fig. 28: The calculation process for the Matlab code using linear regression following York (1968) in the Granger code

In the first step, the ^{26}Al and ^{10}Be concentrations are plotted with 1σ uncertainty for each sample. An initial regression is fitted through the data points, which yields a first slope and intercept of the line (Fig. 29A). This first slope can now be used to calculate a first estimate of the isochron burial age. The user has to decide whether post-burial production is best approximated by constant production (maximum post-burial production under zero erosion) or recent exposure (minimum post-burial production, erosion > 0). Accordingly, the post-burial production is calculated based on this initial age estimate.

The intercept of this post-burial production line with the initial regression line gives the post-burial component of ^{10}Be and ^{26}Al for the samples (box "Calculate post-burial production" in Fig. 28, see also Fig. 29B). If the calculated post-burial production exceeds the lowest measured concentration, the latter is taken as post-burial production (which is important for datasets with very low nuclide concentrations).

The next calculation steps describe the correction for pre-burial complex erosion history and the required linearisation of the ^{10}Be data (Fig. 29B). Again, the user has to decide whether the pre-burial erosion history is best represented by constant exposure (zero erosion rate) or assumed steady erosion (erosion rate > 0). For actively eroding landscapes, the latter should be chosen. Based on the initial burial age estimate and the selected pre-burial erosion scheme, the inherited nuclide concentrations are corrected for radioactive decay. These decay-corrected, inherited ^{10}Be concentrations differ from the uncorrected, inherited ^{10}Be concentrations by a sample-specific linearisation factor (mostly close to 1 for the cases analysed here, values of exactly 1 do not change the sample concentrations for the fit). The fitted ^{10}Be concentrations are the sum of the previously calculated ^{10}Be post-burial production term and the linearised, inherited ^{10}Be concentrations.

The fitted ^{10}Be concentrations are then plotted against the measured ^{26}Al concentrations. In this updated plot, a regression is fitted through and the slope is used to calculate the isochron burial age. The entire process is iterated until convergence (difference < 0.005 Myr). For each new iteration loop, the measured data are randomised within their 1σ Gaussian interval. The resulting slope representing the measured ratio is inserted into Eq. (3) which is also implemented in the code (Balco & Rovey 2008). The output table consists of the isochron burial age and its absolute uncertainty, which are labelled as "Mean age" and "Error", as well as the slope ("Mean slope" and "Slope_error") and the intercept of the best fit of the regression analysis ("Mean offset" and "Offset_error"). It is important to note that the output parameters slope, intercept and post-burial component of ^{10}Be and ^{26}Al - are listed as normalised parameters. However, back-calculating these normalised parameters is required for using them in other plotting software and was performed by adjusting the Matlab code to perform a multiplication of the normalised values with the correct production rates. The "real", not normalised values are labelled at the end of the code by the suffix "_real", e.g. "Mean_offset_real", etc.

So far, the choice of the scheme for pre-burial exposure and post-burial production does not significantly affect resulting ages for Alpine, glacially derived samples such as the ones from the Deckenschotter deposits from the Northern Swiss foreland. Tests show a difference between the two pre-burial exposure schemes of less than 0.9 % in the resulting age, and less than 0.4 % between the two post-burial production schemes. The post-burial production scheme "recent exposure" seems to be more feasible for the assumedly episodic erosion events along the sampled terraces edges of the Deckenschotter units such as sackung-type movements. For the relevant pre-burial erosion history at the source, the scheme "steady erosion" was chosen to be representative due to the high and continuous Alpine erosion. The choice of the source altitude being either 2'000 or 3'000 m a.s.l. is also not crucial (variation in the calculated age in the order of less than 0.5 %). Source area elevation is more important for cases when erosion rates are low, which is not the case for this setting.

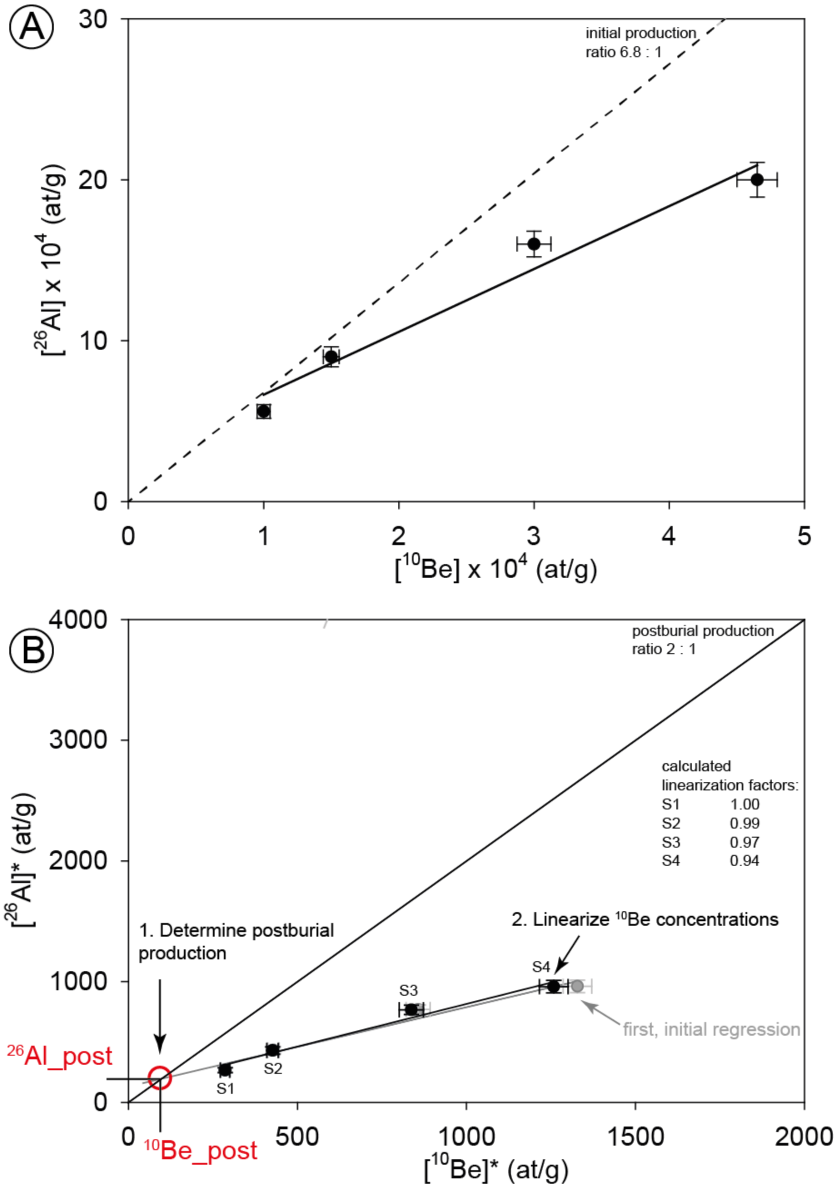

Fig. 29: Illustration showing the working principle of the Granger code using synthetic ^{26}Al and ^{10}Be data (A)

The ^{10}Be data plotted in B) are normalised to sea-level high latitude indicated by the *notation of the ^{10}Be axis (production rate scaled to an altitude of 2'500 m a.s.l. and Lon/Lat for the Central Alps). The intersection point of the post-burial production ratio of 2:1 (because normalised to sea-level high latitude, see Granger (2014) and the first initial regression line give the post-burial production (red circle). The resulting ^{26}Al and ^{10}Be post-burial production is used to calculate the inherited concentrations. The inherited ^{10}Be concentrations are linearised (depending on the chosen pre-burial scheme constant exposure (zero erosion or steady erosion). The fitted ^{10}Be concentrations (= post-burial + linearised concentrations) and the normalised ^{26}Al concentrations are used to perform an improved fit to the data. This process is iterated with measurement data randomised within the Gaussian error of the 1σ range.

3.4.2 Age modelling using the Bayesian approach (Bender code)

In York least-squares linear regression, the slope and intercept values are assumed to be Gaussian, independent, and uncorrelated, unless the correlation coefficient is known. In some cases, this may misrepresent the values and errors of the modelled slope or intercept if there is a correlation between slope and intercept values (Bender et al. 2016). The Bayesian method, on the other hand, tests the likelihood of modelled linear fits to the observed data and can resolve the correlation between parameters without prior knowledge. The resulting posterior probability density functions of parameter values provide a more statistically meaningful assessment of uncertainty of slope and intercept. The most likely estimate (MLE) in York and Bayesian linear regressions is typically the same or very similar (Bender et al. 2016).

Bender et al. (2016) incorporated the Bayesian approach into a Matlab script with the aim of fitting a line using a Bayes Monte Carlo search, assuming Gaussian errors. In contrast to the Granger code, the measured ^{26}Al and ^{10}Be concentrations are the only relevant input data (Fig. 30) and neither information on pre- and post-burial production schemes nor source areas has to be provided. The user can support the finding of the best solution by setting appropriate prior bounds for possible ranges of slope and intercepts. Prior to age calculation, the nuclide data are internally normalised for each nuclide. From each sample concentration, the arithmetic mean of the dataset is subtracted and then divided by the corresponding standard deviation. The resulting plot of residuals indicates whether there are samples that deviate by $> 2\sigma$ from the other samples. If so, then the model routine stops by warning that there is zero likelihood for models and the uncertainties of the data should be enlarged.

For the actual age calculation, the measured dataset itself is used (no normalisation). The model uniformly searches within the prior bounds to test the likelihood of parameter combinations fitting the measured data. If the prior bounds are too narrow to provide a fit of the data, then a message appears to let the user know. The likelihood of each trial was computed based on the assumption that uncertainties in x and y values of the measured data are Gaussian. The linear fit with the highest calculated likelihood is chosen as the best-fit model (Fig. 31A). If the posterior distributions for parameter values are roughly Gaussian, then the most likely, mean, and median values for slope and intercept are nearly indistinguishable (Fig. 31B).

In contrast to the isochron code presented by D. Granger, the Bender code only delivers slope and y-intercept and corresponding uncertainties of the linear regression. The user therefore has to apply Eq. (3) (Balco & Rovey, 2008) for the age calculation and its uncertainty. There is no possibility to specify pre- and post-burial settings as observed for the sampled site and its corresponding source region. However, as the generated slopes and intercepts for both codes of Granger and Bender yield very similar results, details of pre- and post-burial settings obviously appear not to be crucial in our examples. As mentioned above, the Bender code does not find a solution if it is impossible to pass a line through all of the 2σ uncertainty ellipsoids of the samples (message "check your data errors, no models found"). This issue is relevant for the datasets elaborated in this project, as both small 2σ uncertainty ellipsoids and scattered data may occur simultaneously.

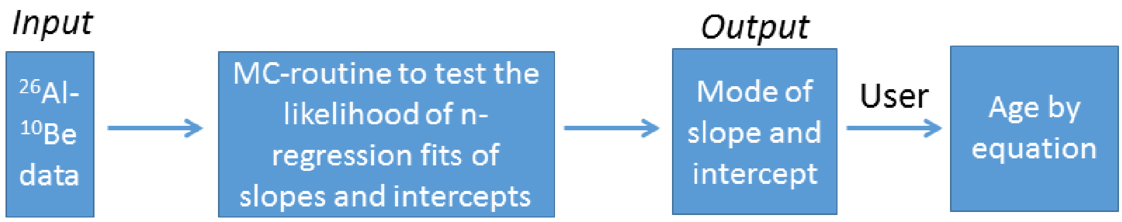

Fig. 30: The calculation process for the code using the Bayesian approach

Bender et al. (2016)

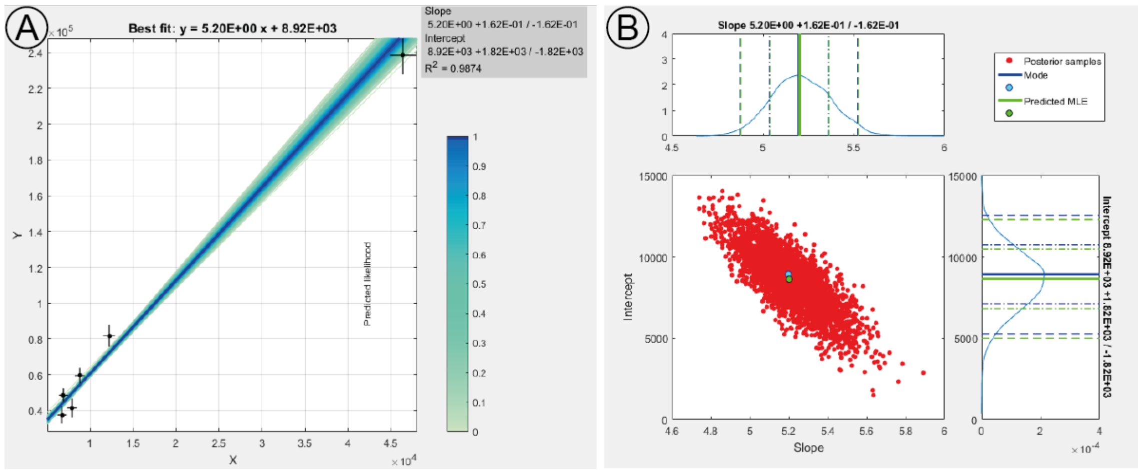

Fig. 31: Output figures from the Bayesian linear regression algorithm

Bender et al. (2016). The ^{26}Al-^{10}Be data plotted along with the results from the Bayesian regression (A). Slope and age uncertainties are based on the uncertainty at the 1σ or 68 % confidence (defined from the code) range for Gaussian and asymmetrical posterior slope distributions, respectively (B). As the mode and the most likely estimate (MLE) of the slope and intercept are almost identical, the posterior distributions are most likely Gaussian. In such a case, the output results from the Granger and Bender codes are necessarily very similar. Note, for the final age calculation it is required that the user takes the mode of the slope to insert into Eq. (3) (Balco & Rovey 2008).

3.4.3 Comparison of Granger and Bender codes

The Granger code is more complex and not as easy to handle as the Bender code. Modelling results from both codes agree well within 1σ, for datasets with samples well oriented along a line (see results below for Feusi). Disagreement occurs where the code must calculate a regression through datasets with a data cloud and a single datapoint which steers the linear regression (see results below for Iberig and Tromsberg).

Comparing the frequency with which both codes have been used in publications, there is a strong difference between the Granger and Bender codes. The Granger code has been used in a few publications (e.g. Çiner et al. 2015, Erlanger et al. 2012, Zhao et al. 2016, Zhao et al. 2017). In contrast, the Bender code has been used only once in the original publication of Bender et al. (2016). For the sake of comparison, both codes are applied for age modelling in the results (see the following chapter).

The Bender code is valid only for cases where erosion rates are fast enough to render radioactive decay prior to burial unimportant. Otherwise the data are spread along a curve rather than a line, and the regression will yield an incorrect age. The Granger code takes radioactive decay prior to burial into account and can thus also be used in settings with low erosion rates.

4 Sampling sites

The first section of this chapter (Section 4.1, Selection process) deals with the previously determined criteria for assessing the quality of outcrops for applying isochron burial. Based on their ranking, a final selection of outcrops was made and is presented in the second part of this chapter (Section 4.2, Overview and presentation of the sampling sites).

4.1 Selection process based on the map of outcrop potential

The outcrop locations for sampling were chosen based on a few criteria in the form of a decision tree, where each criterion is assigned points (see Appendix B "Assessment of the outcrop potential for isochron burial dating"). The final sum determines whether the outcrop has a high or low potential to be successfully dated using isochron burial dating. The final estimated potential level is displayed in the map (Fig. 32). Additional attributes checked include available grain-size fractions in the sediment matrix or in lenses, paleosols or other sequence boundaries, maximum depths possible to sample (for true burial) and, last but not least, practical and logistical issues (rockfall, safety, access).

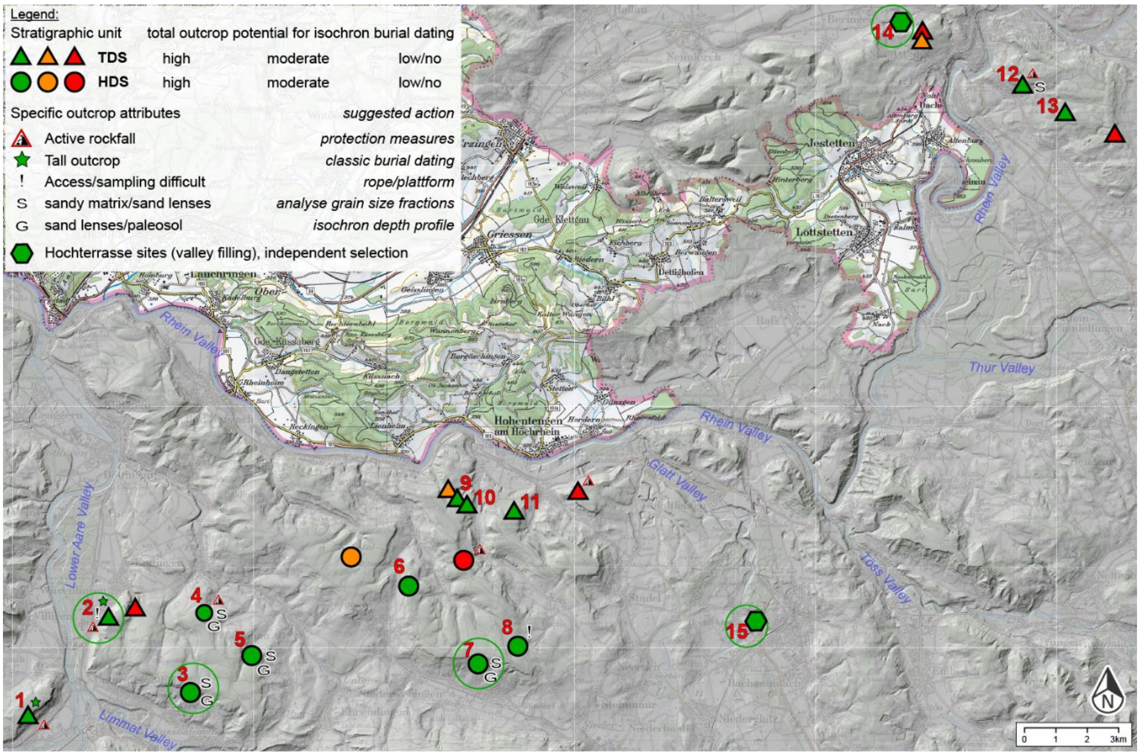

Fig. 32: Map of the Northern Swiss foreland with the classified outcrop potential

Certain regions such as Irchel or around Mandach were not subject to this assessment due to ongoing projects of other scientists. The circled sites No. 2, 3, 7, 14 and 15 represent all sampled sites up to December 2018. The sites No. 14 and 15 (Beringen and Glatt Valley, see main text) were not part of the outcrop evaluation. As for the Cholfirst site, only reconnaissance work was performed in order to evaluate the abundance of quartz-rich lithologies for a pilot study (see Appendix C).

According to the map (Fig. 32), several outcrops from both Höhere and Tiefere Deckenschotter units show a high potential (from left to right, indicated by green colours on the map): 1) Bruggerberg 2) Iberig (both TDS), 3) Tromsberg, 4) Stutz-Usserberg and 5) Hüsliberg, 6) Schüliberg, 7) Feusi, 8) Sünikon (all HDS), 9-10) Oberbelche-West and -East, 11) Schwändihalden, 12) Chirchhölzli and 13) Vorder Hörnli (all TDS).

4.2 Overview and presentation of the sampling sites

Following the outcrop catalogue and the individual ranking, three different outcrops were chosen for sampling and investigation using isochron burial dating (Fig. 32). For the Höhere Deckenschotter unit, these are the Tromsberg (Dürn-Gländ) and Feusi (Egg, Oberweningen) sites. The sampling sites belonging to the Tiefere Deckenschotter are Iberig (Würenlingen) and Cholfirst (Laufen-Uhwiesen). Due to the adjacent proximity of the Tromsberg and Iberig sites, the aim is to reconstruct the incision along a transect. Two outcrops belonging to the Hochterrasse were selected independently of the outcrop assessment: the active gravel pit in Beringen and the samples from the drill core "Bülach B5/12" and "Hochfelden B1/12" from the Glatt Valley (Buechi et al. 2017a). In the following sub-sections, more details about these sampling sites are provided. Additionally, available knowledge from the literature will be presented. As is it not the goal to present a comprehensive literature review for each site, the reader is referred to the cited references where indicated.

Tab. 12: Table of sampled sites in the Northern Swiss foreland with details of collected samples

Stratigraphic unit	**Name site**	**Archive type**	**Municipality**	**Altitude sample** [m]	**Swiss Coordinates CH1903**	**Sampling depth** [m]	**# collected samples**
HDS	Tromsberg	Outcrop	Kirchdorf	560	663'749 261'512	~ 15	~ 45
HDS	Feusi	Outcrop	Oberweningen	600	672'951 262'502	~ 8 – 10	~ 40
TDS	Iberig	Outcrop	Würenlingen	458	661'188 263'896	~ 22	~ 60
HT	Glatt Valley	Drill core B5/12	Hochfelden		681'786 263'503	144.5 – 151	1
		Drill core B1/12	Bülach		682'367 264'900	171.5 – 167	2
HT	Beringen	Outcrop	Beringen	410	663'760 261'530	35 – 40	~ 40

4.3 Höhere Deckenschotter

4.3.1 Tromsberg, Dürn-Gländ

The Tromsberg outcrop, north of the village Kirchdorf AG, is situated in the southern rock cliff of the "Dürn-Gländ" hill chain. It represents a former, man-made gravel pit for local use of gravel. Its stratigraphy represents a typical sequence of Deckenschotter consisting of sandy gravels with intercalated block or gravel layers and sand lenses (Fig. 33 and 34).

Fig. 33: Outcrop situation at the Tromsberg gravel pit (Kiesgrube, KG)

Showing the rock wall with two sampled sandy intervals (sandy gravel left, sand lens right) which are suitable for isochron burial using different grain sizes whose measurements can be compared with those of clasts. According to Graf (1993), the sediment strata visible in this outcrop are interpreted to be the "Südliche Dürnschotter". The size of the book is 21 × 13 cm.

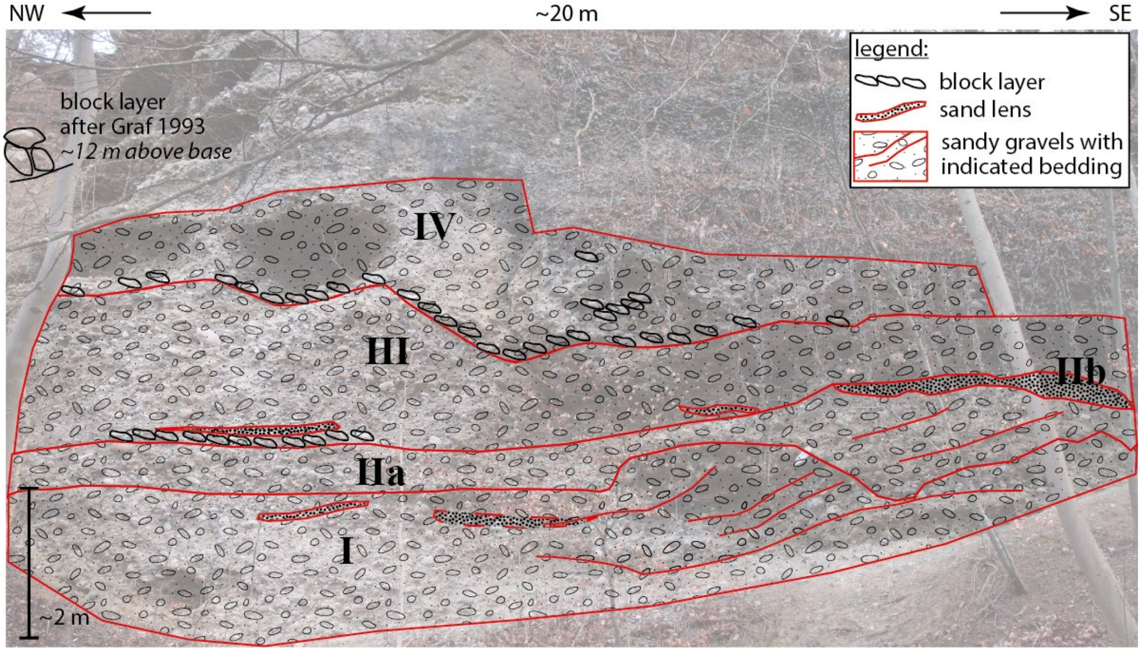

Fig. 34: Schematic stratigraphy sequence based on photographs and field observations

The sequences I and II (a and b) were selected for sampling (the extent of this figure is equal to the outcrop picture in Fig. 33).

According to Graf (1993), there are grey gravels at the base with a few spots of infiltrated glacial milk. Vertically in the middle of the outcrop there is a 2-m thick intercalated, matrix-supported block layer with diameters up to 45 cm. Towards the top, the gravel facies gradually change to a block facies with blocks of several cubic metres' volume. The lithology spectrum confirmed that found by Graf (1993) and consists of Alpine limestones, quartzites and Jurassic carbonates from the Malm and Dogger periods. Besides this, reworked Molasseknauer and the rather rare Sernifit and Quartenschiefer were found.

Following Graf (1993), the sampled horizon at the Tromsberg outcrop can be related to the Südliche Dürnschotter. These gravel deposits were deposited north of the Walensee-Rhine system. The block facies indicates a close glacier, but a basal till has not been found so far. Since there is a gradual change from gravel to block facies, these gravels were interpreted as being related to a glacier advance (Graf 1993). Attempts to date the Deckenschotter at this specific outcrop have not been performed so far.

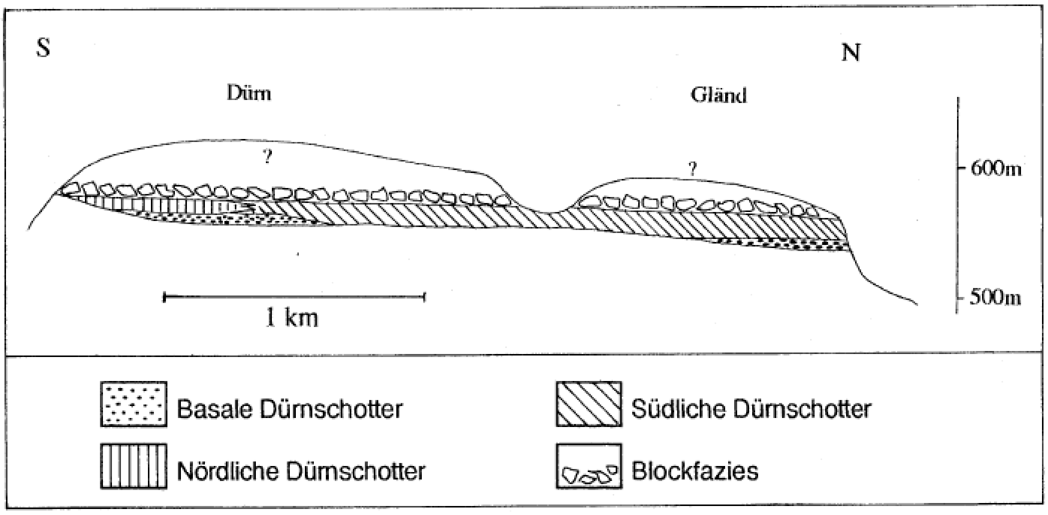

Fig. 35: Schematic profile through the Höhere Deckenschotter of Dürn-Gländ

Graf (1993). The sampled outcrop is on the left (southern) side of the hill.

4.3.2 Feusi (Egg)

The Feusi outcrop is situated in the southern rock cliff of the hill chain "Egg" or also "Schliniker Platten" north of the village of Oberweningen. It represents a former, man-made gravel pit for local use of gravel. Its stratigraphy represents a particularly interesting sequence of Deckenschotter with intercalated glaciofluvial gravels and sands with a prominent, faintly beige till layer in the upper half of the outcrop face (Fig. 36 and 37). The till layer itself has not been studied in detail due to its inaccessible location 10 m above the ground and the overhanging roof consisting of gravels (Graf 1993 and references therein). For the recent work, the sedimentological and geotechnical parameters of the till layer were studied in detail (Buechi et al. 2018). Besides this study, attempts to date using paleomagnetism are also in progress (S. Scheidt, pers. comm.).

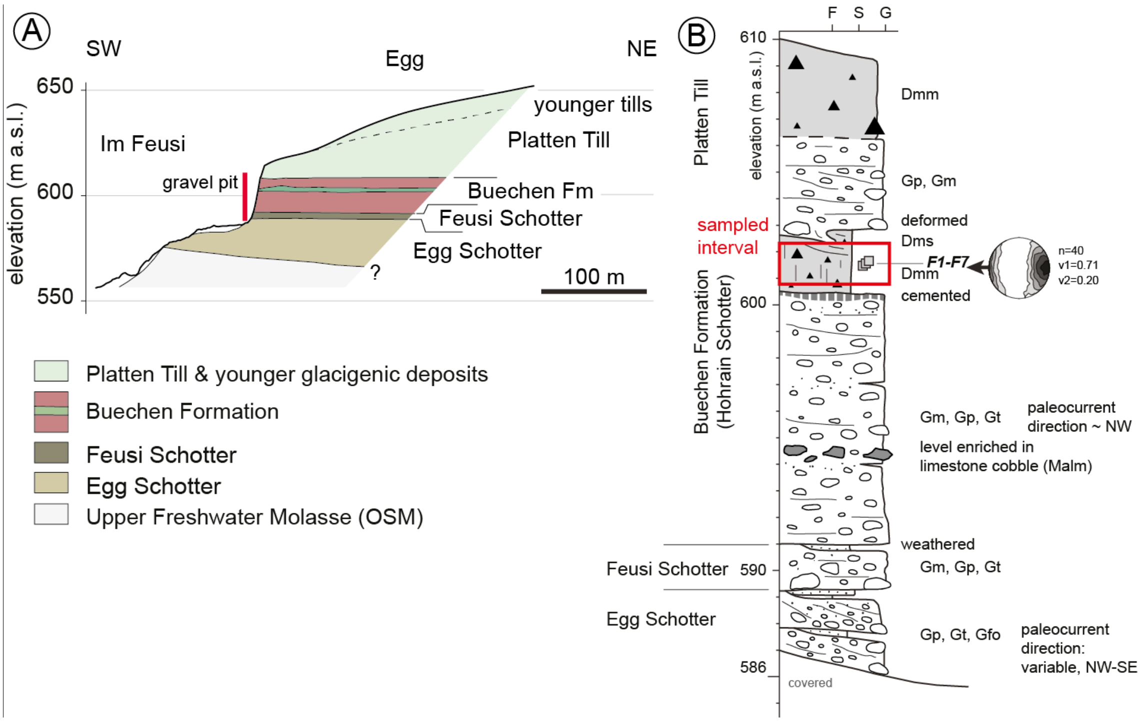

Fig. 36: Stratigraphy at the Feusi outcrop with details of the gravel pit

Modified according to Buechi et al. (2018), Graf et al. (2006) and Haldimann et al. (2017). A) shows a schematic overview and the names of the different sediment deposits and B) shows the layer sequence and details of the sedimentary facies.

The stratigraphy of the outcrop is presented in Fig. 36. The basal and only partly outcropping layer is the Egg Schotter (Graf 1993). This unit represents a few-metre-thick sequence of glaciofluvial gravels separated by a 5-cm thick lens of silt at the top as a transition from a further unit of 2 m of glaciofluvial gravels in the hanging part, the "Feusi Schotter". The thickest formation of the outcrop is represented by the Buechen Formation (Hohrain Schotter, Graf (1993), with ten metres of glaciofluvial gravels and an intercalated prominent 2 – 3-m thick diamict and again glaciofluvial gravels above the diamict (Fig. 37). This lower diamict, which has been sampled in this study, was interpreted to be a till based on the abundance of scratched clasts. The topmost gravel sheets – the Buechen Formation – show wedge-type erosion features into this till body, indicating that diagenetic processes were consolidating the till before the gravels were deposited. The topmost gravel layer in the outcrop is represented by the Platten Till, a washed-out diamict either from actual till deposition or washed out and re-deposited from till bodies located higher up.

Fig. 37: "Feusi" outcrop at the Egg/Schliniker Platten site

Close-up pictures show the prominent till layer during sampling. The till layer was sampled along the yellow boxes as sketched in the upper photograph.

4.4 Tiefere Deckenschotter

Iberig

The Iberig sampling site, east of the village of Würenlingen, is located in the Lower Aare Valley on the eastern valley flank formed by the Iberig hill. The outcrop is a beautiful example of bedrock incision (Fig. 38), here Jurassic limestone (Malmkalke) and subsequent infill of Deckenschotter deposits (Graf 1993, Preusser et al. 2011). The SW-NE trending channel is clearly visible looking from the west and has been documented by several drillings on top of the hill (Preusser et al. 2011). For a visualisation of the channel, the bedrock surface was roughly mapped based on the drillings where the bedrock was identified (Fig. 39A-B). The drillings further revealed the presence of three glaciofluvial and two glacial units at this site (Fig. 39C, Preusser et al. 2011). Based on gravel petrography, the conclusion was drawn that the lower till and the lower gravel unit (Wolfacher Schotter, Wolfacher Till) are genetically related (Fig. 41C, Graf (1993). The middle gravel unit (Iberig Schotter) reveals no petrographic relation to the glacigenic deposits, but the two upper units are again genetically related (Bärengraben Schotter, Bärengraben Till). So far, the depositional age of this site has not been constrained.

Fig. 38: Northern part of the Iberig outcrop with the discordance of Jurassic limestones and Tiefere Deckenschotter deposits

A): Northern part of the Iberig outcrop with the discordance of Jurassic limestones and Tiefere Deckenschotter deposits. An incision into the limestones is indicated by the obliquely cut limestone strata. B) Inset picture: most southern part of the Tiefere Deckenschotter (bedrock below the outcrop base). Large picture: zoomed picture with the main sampling horizon of 2 m height (to the right of the person standing). All samples that could be accessed without a ladder were sampled (including the prominent sand lens in the middle).

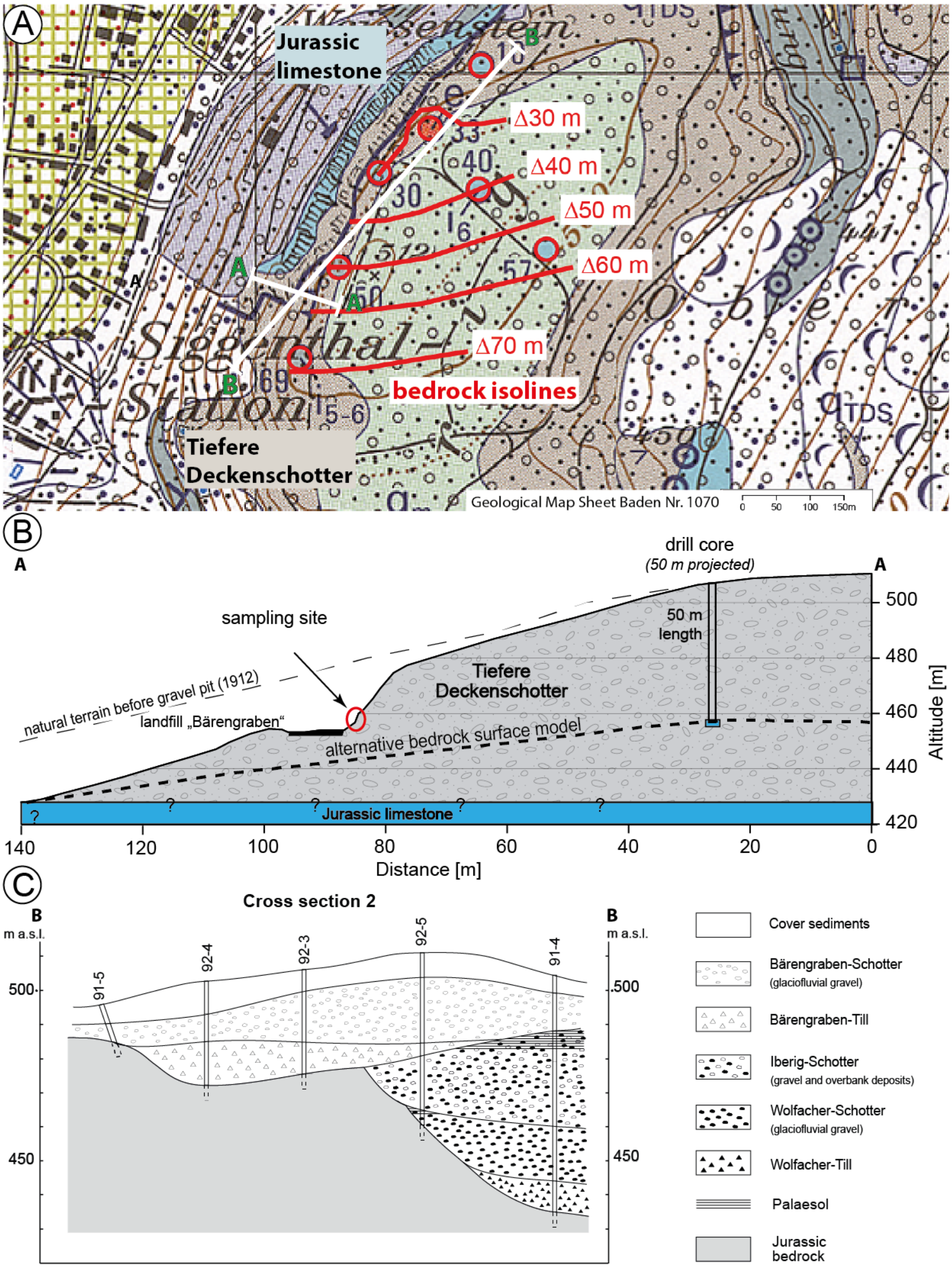

Fig. 39: Geological map of the Iberig in the municipality Würenlingen and cross-profiles

A): Geological map of the Iberig in the municipality Würenlingen with indicated drill cores and mapped bedrock surface that exhibits a channel morphology. B): Cross-profile W-E with profile trace indicated in A) with the artificial outcrop (former gravel pit), the sampling site and interpreted bedrock surface. An alternative bedrock surface is suggested because the drill core had to be projected from 50 m distance to the profile trace. C): Cross-profile SW-NE across the hill with indicated drillings (figure modified from Preusser et al. (2011) and Graf 1993). The sampled horizon is interpreted to be within the Wolfacher-Schotter.

4.5 Hochterrasse

Beringen

The study site is located in the eastern part or entrance of the Klettgau Valley in Schaffhausen and is understood to record several phases of glaciation during the Pleistocene. This valley was part of the Rhine Valley during most of the Pleistocene prior to the re-rerouting to today's riverbed but remained dry as an abandoned valley (Graf 2009 and references therein).

In the original study site of Lowick et al. (2015), located in a now filled gravel pit, a succession of two gravel units – the Hardau and Geisslingen Schotter, both glaciofluvial gravels - was described (Fig. 40). The gravel units were interpreted to represent two distinct glaciations. The block layer separating these units was interpreted to represent a glacier advance close to or at the study site, which was also important to distinguish them in the field. However, a clear distinction between these two units was not even clear to the authors of the paper. The third, stratigraphically higher formation is the Buechbrunnen Schotter also representing a glaciofluvial gravel. The topmost formations are the Schmerlet and Lusbüel Formations that represent a succession of fluvial/lacustrine and diamictic/glaciofluvial sediments. For details of the stratigraphy, see Lowick et al. (2015) and references therein. Age determinations in the Hardau Schotter yielded uncorrected feldspar infrared stimulated luminescence (IRSL) and quartz OSL ages of ~ 200 kyr. These ages were considered to be reliable but significantly underestimated the expected ages and prompted a reconsideration of earlier interpretations of the stratigraphy for this site. Therefore, dating these sediments with cosmogenic nuclides might allow cross calibration of the luminescence ages. The OSL ages with ~ 200 kyr represent the lower age limit of burial dating, since the nuclide signature is difficult to distinguish from present-day samples. According to Graf (2009), the deposits are assumed to be older, and there might therefore be a potential to better constrain the age by burial dating.

The sampling site in this study is located 400 – 500 m to the east of the original study site (a re-filled gravel pit) in the open gravel pit of the Kies AG Beringen company whose gravel excavation is ongoing. At an elevation similar to that in the study of Lowick et al. (2015), a weakly articulated gravel and block layer was found at the deepest point of the active gravel pit (note that in 2018 this pit was in an infilling stage). This layer was interpreted to be the prominent block layer known from the study of Lowick et al. (2015). Therefore, the first sampling campaign in spring 2017 was performed along this block layer. A second sampling campaign in summer 2018 was carried out approximately 50 m further to the south (Fig. 41 and 42). The correlation of these two outcrops could be reasonably established, and therefore both sub-sample sets can be virtually merged and considered to originate from the same sampled horizon.

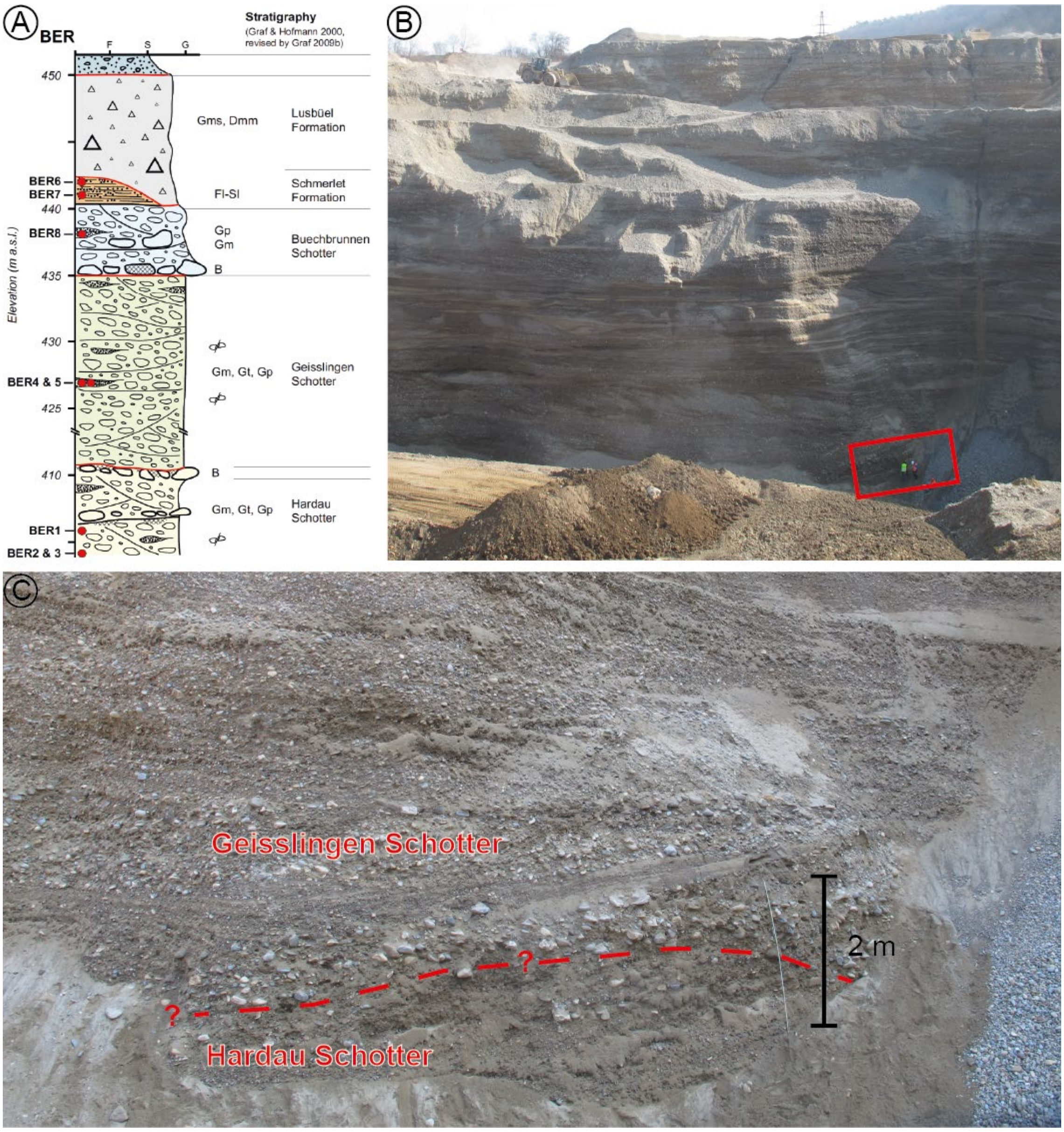

Fig. 40: Stratigraphic profile

A) Stratigraphic profile from Lowick et al. (2015) who dated the sampled horizons at the base of the gravel pit – the Hardau-Schotter - to ~ 200 kyr. B) and C) are taken from the open gravel pit (1. sampling campaign) and the interpreted situation in the outcrop with assignment of the formations. The boundary between the Hardau and Geisslingen Schotter is unclear.

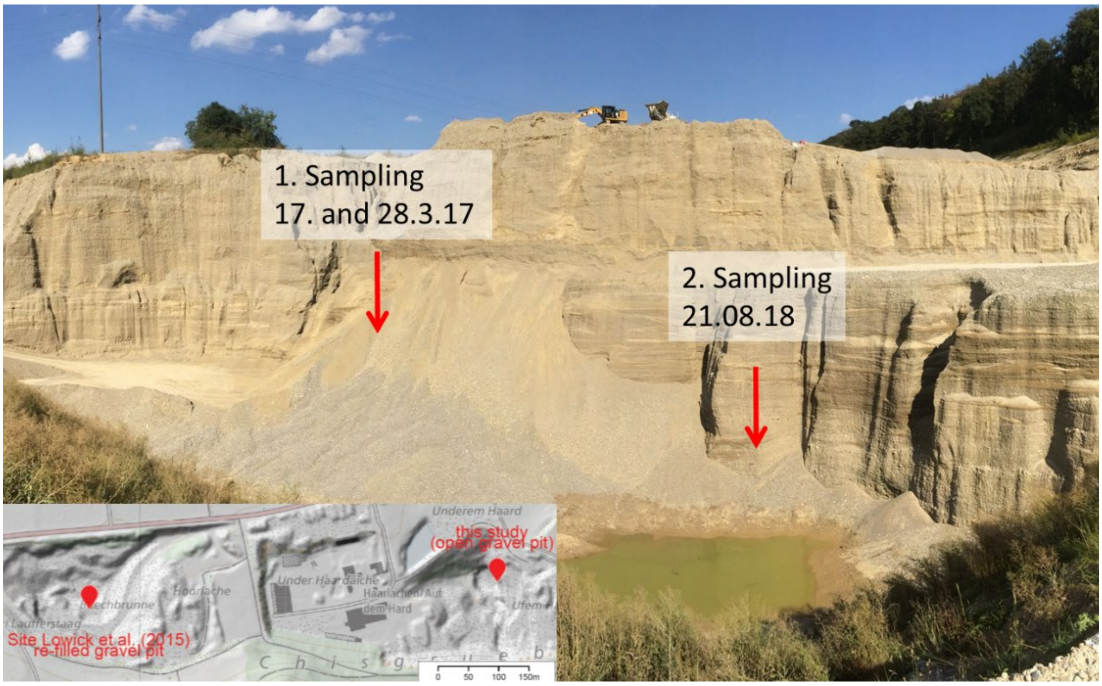

Fig. 41: Field picture from the west to the east with indicated sampling locations (first and second time)

The zoomed map view indicates the original study site of Lowick et al. (2015) and our study site further to the east. Initial sampling occurred before the fresh talus (visible in this photograph) was deposited. The sampled horizons were at the same elevations (arrows might be misleading).

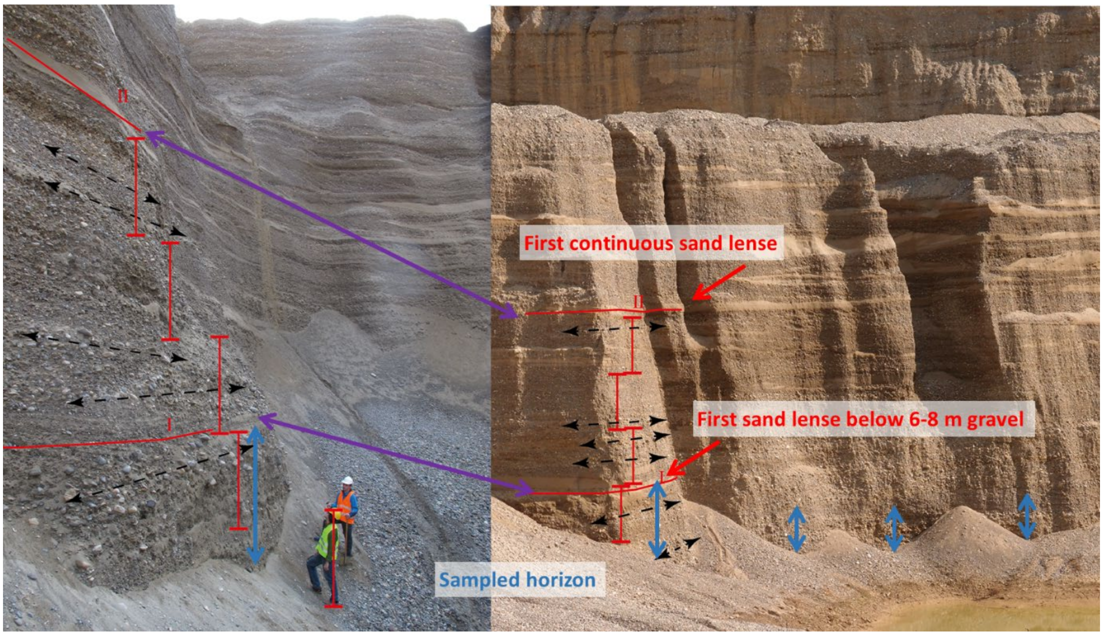

Fig. 42: Comparison of the outcrops from the first and second sampling campaigns

Although the horizontal extension of the sand and gravel lenses in particular is genetically rather unlikely, a reasonable correlation of the two outcrops could be established.

Glatt Valley

The study site is located in the Lower Glatt Valley in the north-eastern Swiss foreland (Fig. 43A). The Valley is considered to be the result of Pleistocene subglacial erosion by repeated advances of the Glatt Valley lobe of the Linth-Rhine glacier (Buechi et al. 2017a, Buechi et al. 2018, Preusser et al. 2011). Numerous boreholes revealed a buried bedrock relief with distinct narrow, deep troughs (Fig. 45B, cf. Jordan (2010). These troughs extend 180 m below the modern, and 140 m below the lowest Pleistocene base level, respectively (Glatt and Rhine river; Graf (2009) and are therefore termed "overdeepened" (e.g. Preusser et al. 2010).

Buechi et al. (2017a) studied the drill cores B1/12 (from the Bülach Trough) and B5/12 (Hochfelden) in detail (Fig. 44) and, among other units, found diamicts that were interpreted as subglacial tills. The interpretation of several drill cores allowed reconstruction of the sedimentary architecture of the fill in this overdeepened glacial basin. The reconstruction of the basal infill revealed three glaciolacustrine depositional periods. However, the timing during which overdeepened basins were eroded and filled is largely unknown. Buechi et al. (2017b) attempted to numerically date the infill of this overdeepened basin with luminescence dating. While IRSL signals are close to saturation, quartz OSL ages were considered to be within the range of reliable dating. For the drill core B5/12, quartz OSL ages of ~ 200 kyr were reported. In fact, 100 to 200 kyr is the lower limit for burial dating and therefore presents an opportunity to cross-calibrate burial dating using OSL.

In order to improve the current chronology based on luminescence dating, an attempt to burial date samples from the drill core was undertaken (Fig. 44). Similar to the situation at the Beringen site, complete shielding during the entire burial time was assumed. This assumption allows true burial dating to be applied based on one single sample. Two samples (indicated in Fig. 46) were taken from the drill cores B5/12 and B1/12 at depth intervals of 134 – 138 m (Gla1) and 167 – 171.5 m (Gla3). The selection process was driven purely by the fact that enough sand-sized quartz could be found within the silt-dominated grain size of the sediment. In order to maximise the sample volume, the dried-out core pieces or briquette-types were collected in boxes. The dry silty sands were then directly washed in these boxes to wet-sieve the sediment for acquiring sand. The sampled spectrum consists of two sand samples since true burial dating was attempted. A detailed list of all processed samples can be found in Appendix C "Detailed list of all samples".

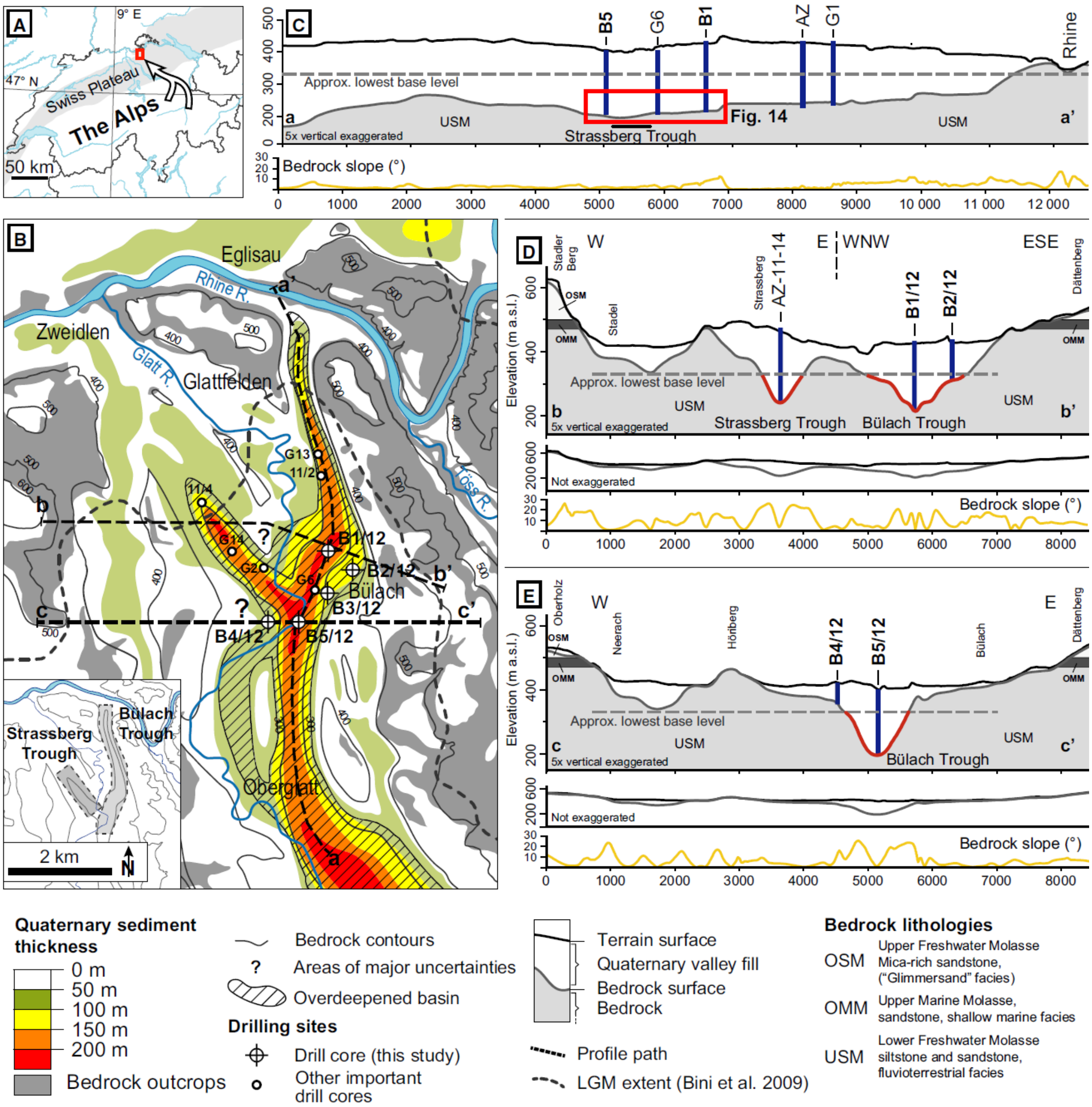

Fig. 43: Location of the study area in the Lower Glatt Valley in the Northern Swiss Plateau, bedrock surface map, longitudinal valley profile, valley cross-sections

Figure and text from Buechi et al. (2017a): (A) Location of the study area in the Lower Glatt Valley in the Northern Swiss Plateau (shaded area: Molasse basin). The arrows indicate the general ice flow direction during the Pleistocene. (B) Bedrock surface map indicating the extension of the overdeepened basins (Bülach and Strassberg Troughs, see inset) and the approximate thickness of the Quaternary infill (calculated as surface minus bedrock elevation; bedrock surface map is courtesy of AWEL and Nagra). Only important drillings are shown. (C) Longitudinal valley profile a-a' along the deepest part of the Bülach Trough until its abrupt termination in a reverse slope. (D) and (E) Valley cross-sections b-b' and c-c' showing the narrow and steep inset character of the two troughs cut into the broad valley geometry. The cross-sections are duplicated without vertical exaggeration and with the local bedrock slope to give a more realistic impression of the geometry. LGM = Last Glacial Maximum.

Fig. 44: Logs of the drill cores B5/12 and B1/12 of the basal core segments in the central part of the overdeepened basin

Buechi et al. (2017a). Lithofacies codes after Keller (1996)

5 Results

5.1 Cosmogenic ^{10}Be and ^{26}Al data

Measured ^{10}Be concentrations vary between $(2.8 \pm 0.4) \times 10^3$ at/g and $(4.8 \pm 1.0) \times 10^5$ at/g and ^{26}Al concentrations between $(2.1 \pm 0.3) \times 10^5$ at/g and $(2.0 \pm 0.8) \times 10^6$ at/g (Tab. 13 and Fig. 45 – 46). Total ^{10}Be concentrations of the samples deviate from the added carrier values within the uncertainties of the ICP-MS, which indicate a negligible contribution of native Be, if present. Total Al concentrations are between 6 and 105 ppm. $^{26}Al/^{10}Be$ ratios vary from 3.4 ± 0.2 to 31.0 ± 5.0. Total ^{26}Al concentrations of the samples are of cosmogenic origin, and non-cosmogenic ^{26}Al can be excluded (see Appendix D). The $^{10/9}Be$ ratio of the IBE55 sample could not be measured due to sample loss in the lab.

Tab. 13: Table of ^{26}Al and ^{10}Be concentrations

Site	**Sample weight**	**Carrier weight**	**^{27}Al 1σ=3 %**	**$^{26/27}Al$ AMS**		**^{26}Al**	**1σ**	**$^{10/9}Be$ AMS**		**^{10}Be**	**1σ**	**$^{26}Al/^{10}Be$**	**1σ**	
	[g]	**[mg]**	**[ppm]**	**10^{-12}**	**1σ** (%)	**at/g**	**at/g**	**10^{-12}**	**1σ** (%)	**at/g**	**at/g**	**[-]**	**[-]**	
Beringen														
BER11	63.255	0.198	11.09	0.138	17	34'052	4'976	0.019	14	2'887	410	**11.8**	**3.7**	**x,y**
BER6	54.655	0.201	35.72	0.108	13	86'454	9'462	0.024	16	4'648	737	**18.6**	**5.4**	**x,y**
Ber4	59.328	0.160	52.97	0.061	10	72'286	8'317	0.054	6	8'864	496	**8.2**	**1.2**	**y**
Ber1	49.262	0.123	51.29	0.018	12	20'841	2'736	0.027	8	3'553	295	**5.9**	**1.2**	
Ber7	45.772	0.163	14.55	0.273	8	88'625	7'495	0.055	6	11'740	710	**7.5**	**1.1**	
Ber 17	58.079	0.174	69.95	0.157	6	275'069	17'011	0.050	10	8'876	873	**31.0**	**5.0**	**y**
Ber 35	64.900	0.180	64.23	0.099	9	147'997	13'529	0.132	6	23'504	1'417	**6.30**	**0.96**	
Ber 36	64.481	0.177	71.77	0.166	9	283'402	25'462	0.097	6	16'767	1'033	**16.9**	**2.6**	**y**
Iberig														
IBE 1	58.792	0.201	88.68	0.022	13	43'469	11'208	0.037	19	7'323	1'388	**5.9**	**1.6**	**x**
IBE-VC	64.158	0.196	33.10	0.077	9	56'594	7'212	0.042	9	7'507	667	**7.5**	**1.9**	**x**
IBE22	63.255	0.160	7.73	0.304	7	52'495	3'914	0.058	5	8'894	480	**5.9**	**0.8**	
IBE23	60.548	0.163	26.67	0.109	8	64'593	6'164	0.074	5	12'327	585	**5.2**	**0.8**	
IBE3	58.732	0.163	20.01	0.497	5	222'155	10'278	0.256	3	46'469	1'483	**4.8**	**0.5**	
Ibe-S	65.479	0.159	80.81	0.020	13	35'651	4'928	0.055	6	8'081	487	**4.4**	**1.0**	
Ibe-VC2	66.533	0.158	80.95	0.018	13	32'593	4'600	0.048	6	6'849	401	**4.8**	**0.9**	
Ibe-GC	66.594	0.161	71.03	0.031	8	48'744	5'372	0.049	6	6'996	407	**7.0**	**1.0**	
IBE 53	55.068	0.179	83.45	0.033	22	78'847	17'106	0.057	8	11'204	846	**7.0**	**2.1**	
IBE 55	62.369	0.179	98.47	0.022	46	55'692	25'453							

Tab. 13: Cont.

Site	Sample weight	Carrier weight	^{27}Al 1σ=3 %	$^{26/27}$Al AMS		^{26}Al	1σ	$^{10/9}$Be AMS		^{10}Be	1σ	^{26}Al/ ^{10}Be	1σ	
	[g]	[mg]	[ppm]	10^{-12}	1σ (%)	at/g	at/g	10^{-12}	1σ (%)	at/g	at/g	[-]	[-]	
Tromsberg														
TRO16	67.795	0.201	89.37	0.038	12	76'025	12'726	0.045	13	7'827	1'070	**9.6**	**1.7**	**x,y**
TRO-VC	65.696	0.202	24.66	0.115	7	63'175	4'898	0.059	10	10'883	1'112	**5.7**	**0.7**	
TRO25	65.944	0.200	61.71	0.100	9	137'245	12'324	0.082	8	15'588	1'279	**8.7**	**1.1**	**x,y**
Tro2	69.012	0.161	6.16	0.244	10	33'547	3'388	0.048	6	6'571	396	**5.0**	**0.6**	
Tro8	71.790	0.161	75.78	0.018	14	30'095	4'456	0.039	6	4"931	318	**6.0**	**0.9**	
Tro-VC2	67.654	0.160	26.12	0.097	9	56'469	4'952	0.070	6	10'195	573	**5.5**	**0.6**	
Tro20	64.904	0.162	59.89	0.055	6	73'501	5'885	0.079	5	12'194	616	**6.0**	**0.5**	
Tro33	64.992	0.160	31.00	0.622	5	430'646	22'076	0.762	2	124'807	2'498	**3.4**	**0.2**	
Tro45	64.939	0.162	50.36	0.057	6	63'517	4'936	0.069	6	10'512	626	**6.0**	**0.5**	
Tro-S	63.890	0.160	78.87	0.030	9	53'402	6'034	0.043	7	6'219	431	**8.5**	**0.9**	**y**
TRO 16*	60.797	0.177	61.94	0.027	21	47'443	9'768	0.050	8	8'747	718	**5.4**	**1.2**	
TRO 25*	24.001	0.178	20.24	0.059	12	87'842	10'741	0.039	14	16'693	2'420	**5.3**	**1.0**	
TRO 27	65.608	0.180	55.90	0.014	27	21'230	5'762	0.027	9	3'978	345	**5.3**	**1.5**	
TRO 40	68.472	0.179	70.92	0.020	27	37'614	10'042	0.056	8	8'769	679	**4.3**	**1.2**	
Feusi														
Feu2	68.437	0.159	67.61	0.065	8	98'093	7'476	0.173	4	25'921	1'002	**3.8**	**0.3**	
Feu4	63.108	0.157	14.95	2.486	4	829'709	30'581	1.295	2	214'944	4'301	**3.9**	**0.2**	
Feu 16	38.818	0.177	30.75	0.128	8	163'031	12'938	0.098	5	28'150	1'460	**5.8**	**0.5**	
Feu 21	58.486	0.178	16.70	0.103	8	47'624	3'793	0.031	13	5'255	691	**9.1**	**1.4**	**y**
Feu 26	60.849	0.178	17.85	0.090	8	43'692	3'478	0.038	12	6'458	801	**6.8**	**1.0**	
Feu 37	59.996	0.178	71.26	1.016	4	2'015'488	78'021	2.399	2	475'954	9'519	**4.2**	**0.2**	
Feu VC	60.079	0.180	9.39	0.251	5	66'462	3'589	0.075	10	14'001	1'393	**4.7**	**0.5**	
Glatt Valley														
Gla3	66.780	0.161	85.40	0.015	13	28'354	3'693	0.030	8	3'860	302	**7.2**	**1.1**	
Gla1	60.712	0.178	105.39	0.025	30	73'657	22'231	0.031	10	4'979	510	**14.8**	**4.7**	**y**

* Indicates a new aliquot from the sample, x = first sample batch, y = excluded from the linear regression.

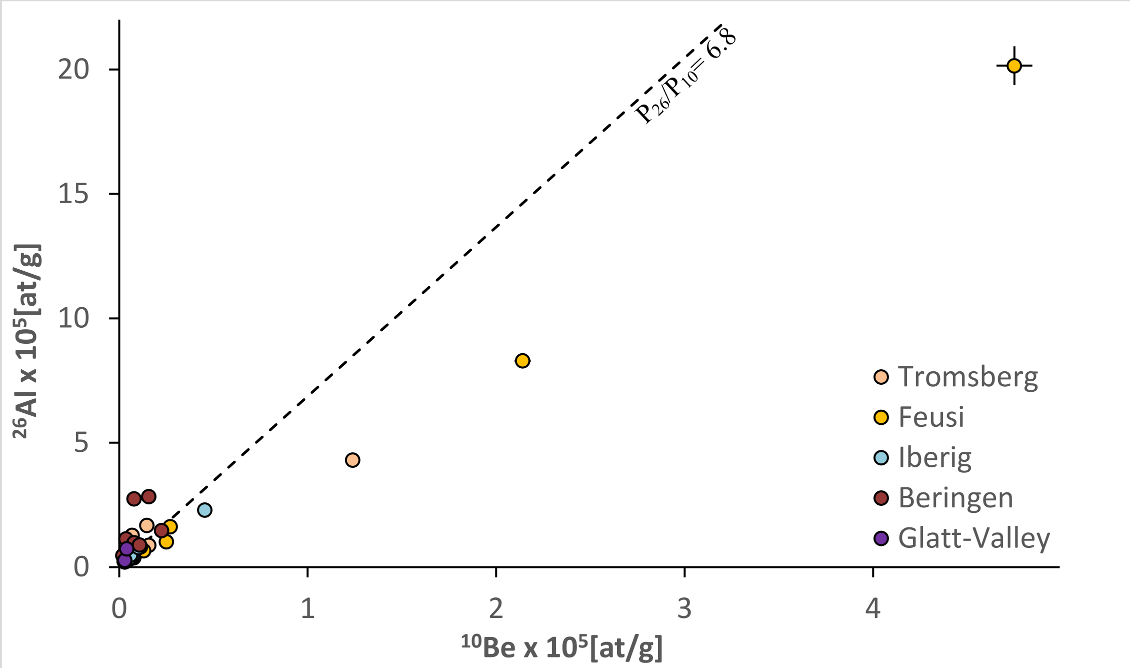

Fig. 45: ^{26}Al-^{10}Be data with 1σ uncertainties for all five sites measured in this project

Colour code as in Tab. 13. Samples with indicated 1σ uncertainties (cross)

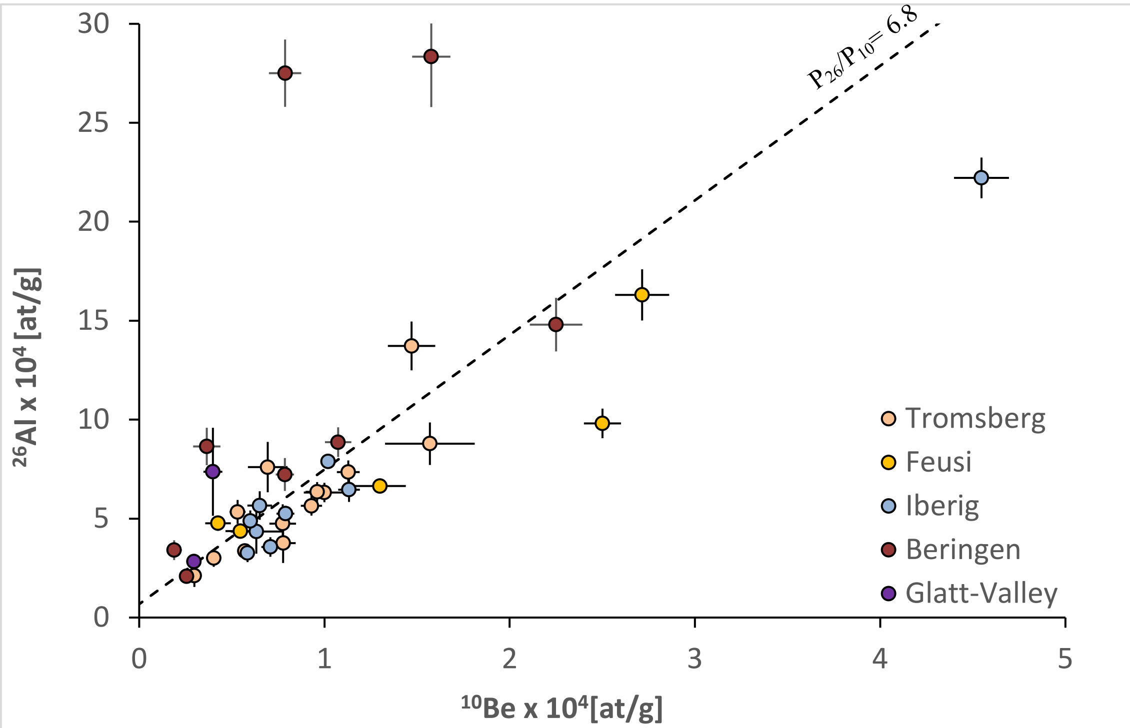

Fig. 46: ^{26}Al-^{10}Be data for all five sites measured below 50'000 at/g 10^{Be} and 300'000 at/g ^{26}Al

More than 90 % of the data plot in the range of rather low ^{10}Be and ^{26}Al concentrations

Internal AMS comparison measurements and consequences

The samples for the very first sample batch measured in summer and autumn 2017 yielded elevated ratios, i.e. clearly above a $^{26}Al/^{10}Be$ ratio of 9 (i.e. no overlap within 1σ with 6.8, see Tab. 13). The first sample batch was designed as a pilot study to evaluate the best procedure for extracting the nuclides from large samples in the lab and measuring low ^{26}Al concentrations with the AMS. Therefore, it was suspected that the elevated $^{26}Al/^{10}Be$ ratios might display an artefact because the chemistry in the laboratory was not optimised. Thus, it was attempted to re-measure these samples. However, only for the Tro16 and Tro25 samples was enough quartz material available to reprocess the sample. The second aliquots from the Tro16 and Tro25 samples were measured in February 2019 (including both AMS and ICP-MS measurements). While the quartz purification procedure remained the same for the second aliquot of Tro16 and Tro25, a few modifications to the extraction and measuring protocols for ^{26}Al and ^{10}Be were applied: the ^{9}Be carrier weight was slightly reduced (to increase the $^{9}Be/^{10}Be$ ratio of the AMS sample), larger ion-exchange columns were used during the nuclide extraction (to increase the chemical yield for both Al and Be), the sample solution was spiked with 100 µl of Fe (ICP standard material) before final precipitation of BeOH (to bulk the material obtained) and, lastly, the AMS measurement time was maximised resulting in more than 4'000 seconds' measurement time (> 1h) for ^{10}Be samples and more than 20'000 s (> 5 h) for ^{26}Al samples (improving AMS counting statistics).

As consequence, the uncertainties for both ^{10}Be concentrations and $^{26}Al/^{27}Al$ ratios of the samples measured in the following batches were significantly reduced. Also, ^{26}Al concentrations of the repeated samples dropped by a factor of 2 – 3 (Fig. 47), while the re-measured ^{10}Be concentrations stayed within 1σ compared to the first measurements. The resulting $^{26}Al/^{10}Be$ ratios of the re-analysed samples plot was within the physically allowed range. Based on these results, we conclude that the elevated (and physically impossible) $^{26}Al/^{10}Be$ ratios measured in a few samples from the first batch probably have to be explained with problems during either Al/Be separation in the lab (e.g. aliquot separation), AMS/ICP measurements and related interferences, or both. Therefore, we decided to exclude the samples Ber11, Ber6, Tro16 and Tro25 from the first batch from further analysis (marked with "x,y" in Tab. 13). Also, some samples that were prepared and measured according to the improved protocol (i.e. Gla1, Feu21, Tro-S, Ber17 and Ber36), show elevated (physically impossible) $^{26}Al/^{10}Be$ ratios. Although repeated measurements are missing for these samples, we decided to also exclude them from further analysis (marked "y" in Tab. 13).

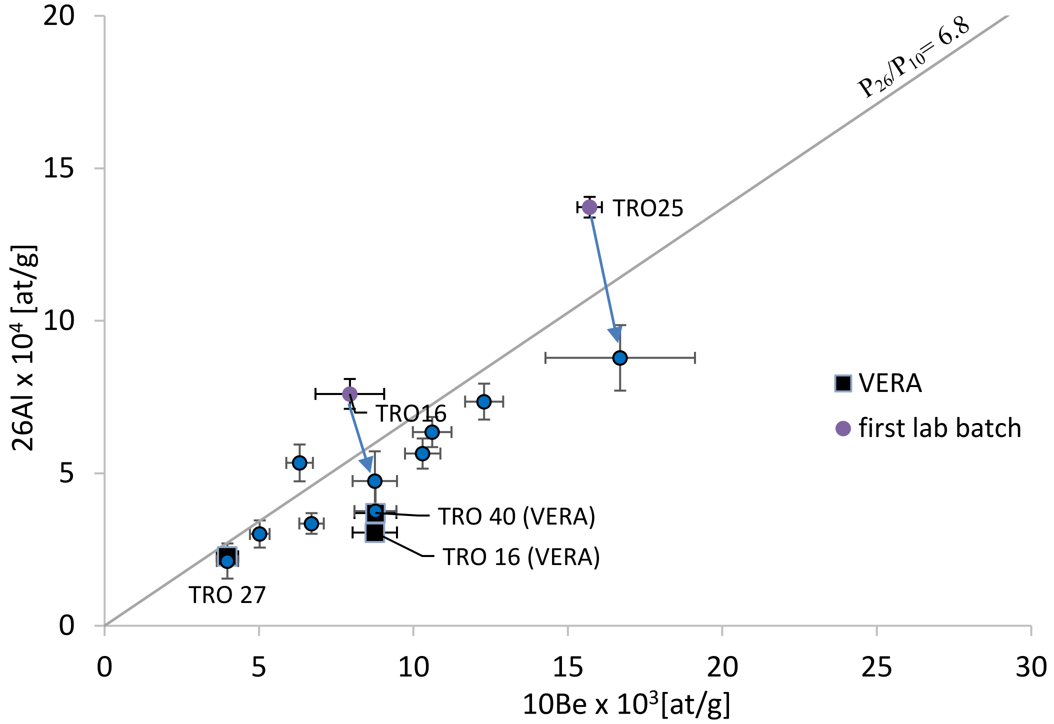

Fig. 47: ^{26}Al-^{10}Be plot of the Tromsberg site

The samples from the first batch Tro16 and Tro25 (yellow circles) show a significant drop after re-measuring (both measured at TANDY-AMS).

The fact that modifications in the chemistry led to lower ^{26}Al measurements and thus more realistic ^{26}Al/^{10}Be ratios indicates that elements which are masked as ^{26}Al in the AMS might have been removed. For instance, molecular Mg could be a potential source of masked ^{26}Al and thus possible AMS interferences (more ^{26}Al is detected than is actually in the sample). However, a rather high Mg content is required to explain the excess of ^{26}Al. Further tests measuring the Mg content in the diluted samples with ICP-MS are recommended, paired with mixed Mg-Al samples for the TANDY set-up.

Measurement times often exceeding 5 hours for a sample can potentially leave the results highly sensitive to low levels of interference, whether from machine background or molecular interference from the samples. It has been shown, however, that the machine background for the AMS facility TANDY used seems to come mainly from the detector (C. Vockenhuber, pers. comm.). Therefore, a constant background rate determined for each measured batch was subtracted from the ^{26}Al counts from each sample (see Appendix D). For samples with very few ^{26}Al counts (low ^{26}Al concentrations), the subtraction of ^{26}Al counts from this correction step varied from 0.3 % for Feu4 up to 73 % (Ibe-55). Samples with low ^{26}Al concentrations show a higher background correction due to low ^{26}Al counts in the detector and long run times. As mentioned previously, samples with low levels of ^{26}Al are strongly dependent on the amount of background correction. However, even if the background correction is inherently uncertain and thus the low ^{26}Al concentration of a sample might show a higher uncertainty, the bulk of samples with low ^{26}Al concentrations confirm the corresponding ^{26}Al signal as an entire cloud.

5.2 ^{26}Al-^{10}Be plots

In the following, the specific datasets for each site combined with the best-fit regression through the data (from the Granger code) are presented. Additionally, the datasets were also modelled with the Bender code whose screenshots of the output figures are available. Note that the Bender code only delivers mean slope and intercept and the final age was calculated using Eq. (3) from Balco & Rovey (2008).

5.2.1 Feusi (HDS)

In total, seven samples were analysed and all show a normal ^{26}Al/^{10}Be ratio, i.e. not higher than the present-day production ratio of 6.8 (Fig. 48). The calculated slopes and intercepts from the Granger and Bender codes are in good agreement as the age estimates are around 1.11 and 1.12 Myr (Fig. 48 and 49, Tab. 14).

Tab. 14: Output table from modelled age estimates using the Granger and Bender codes for Feusi

Calculation method	Model output parameters				Calculated age estimate	
	Mean slope [-]	±1σ	Intercept [at/g]	±1σ	Mean age [Myr]	±1σ
Granger	3.98	0.18	14'291	4'495	1.11	0.09
Bender	3.98	0.48	14'500	1'700	1.12	0.24

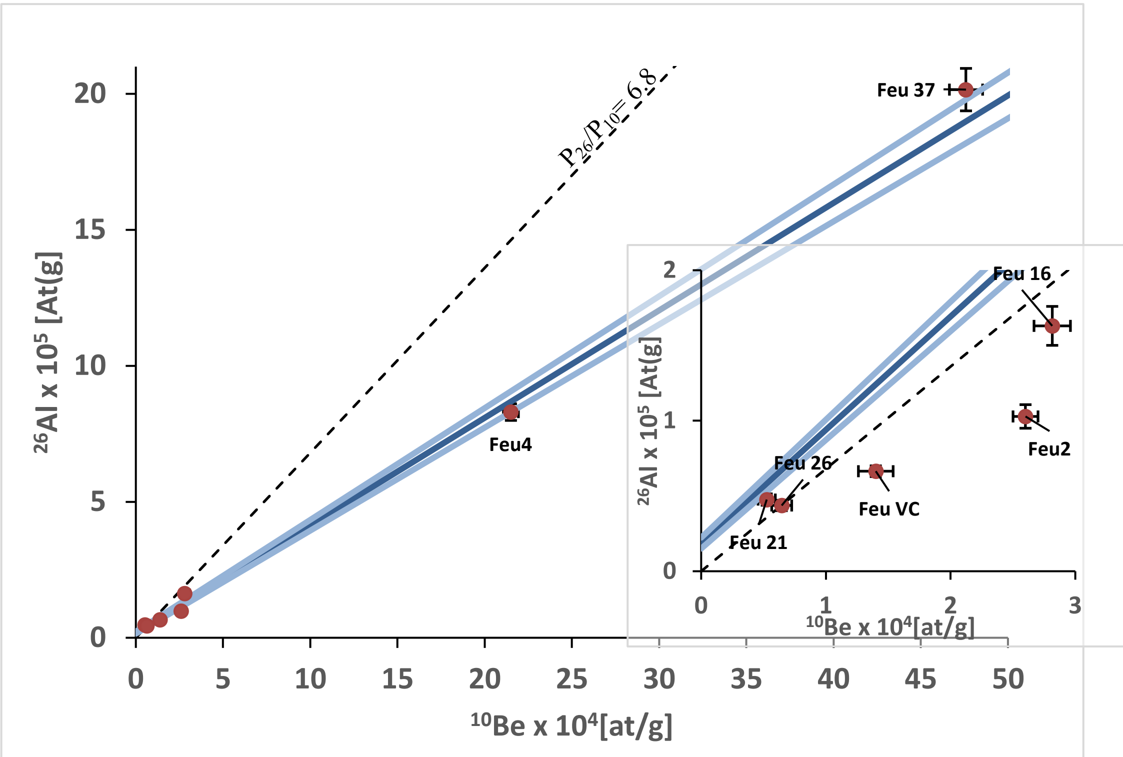

Fig. 48: ^{26}Al-^{10}Be plot of the Feusi site with the modelled linear regression

After Granger (2014). The Feu 21 sample was not considered for the linear regression analysis.

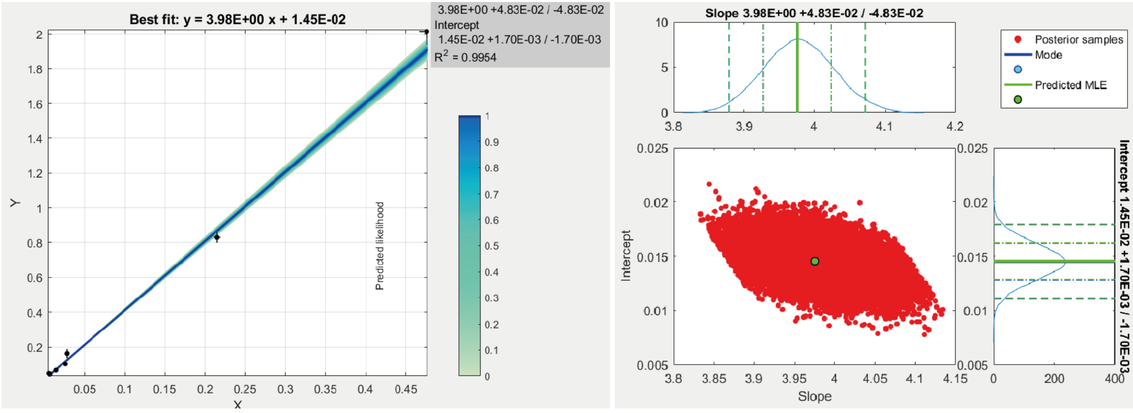

Fig. 49: ^{26}Al-^{10}Be plot of the Feusi site with the modelled linear regression

After Bender et al. (2016). To enable the model to fit a line, the uncertainties of all samples were taken on the 2σ level. To obtain 2σ uncertainties, the existing 1σ were doubled. Consequently, the resulting 1σ error of the age calculated using the Bender code is also enhanced.

5.2.2 Tromsberg (HDS)

In total, fourteen samples were analysed, of which two, Tro16 and Tro25, show an elevated $^{26}Al/^{10}Be$ ratio (Fig. 50). Sample Tro-VC did not show a high ratio but, for the sake of consistency, was also excluded from the later regression analysis along with Tro16 and Tro25 because all three samples were processed in the first batch in the laboratory. As explained above, the data from the first batch were rejected. The calculated slopes and intercepts from the Granger and Bender codes differ slightly but agree within 1σ. The mean age estimates from both codes are 1.41 and 1.23 Myr and overlap with each other (Fig. 50 – 51, Tab. 15).

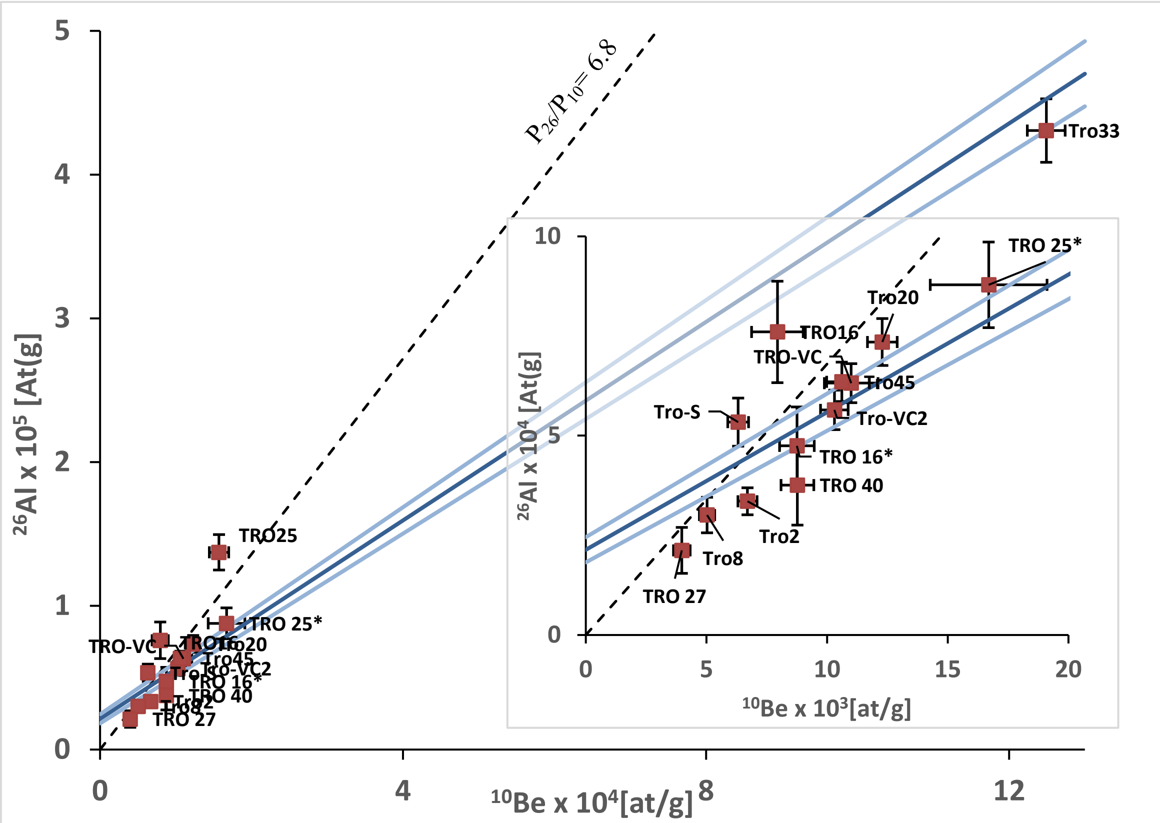

Fig. 50: ^{26}Al-^{10}Be plot of the Tromsberg site with the modelled linear regression

After Granger (2014). The Tro16, Tro25 and Tro-S samples were not considered for the linear regression analysis.

Tab. 15: Output table from modelled age estimates using the Granger and Bender codes for Tromsberg

Calculation method	Model output parameters				Calculated age estimate	
	Mean slope [-]	±1σ	Intercept [at/g]	±1σ	Mean age [Myr]	±1σ
Granger	3.45	0.15	22'110	3'310	1.41	0.16
Bender	3.78	0.14	11'800	1'580	1.23	0.08

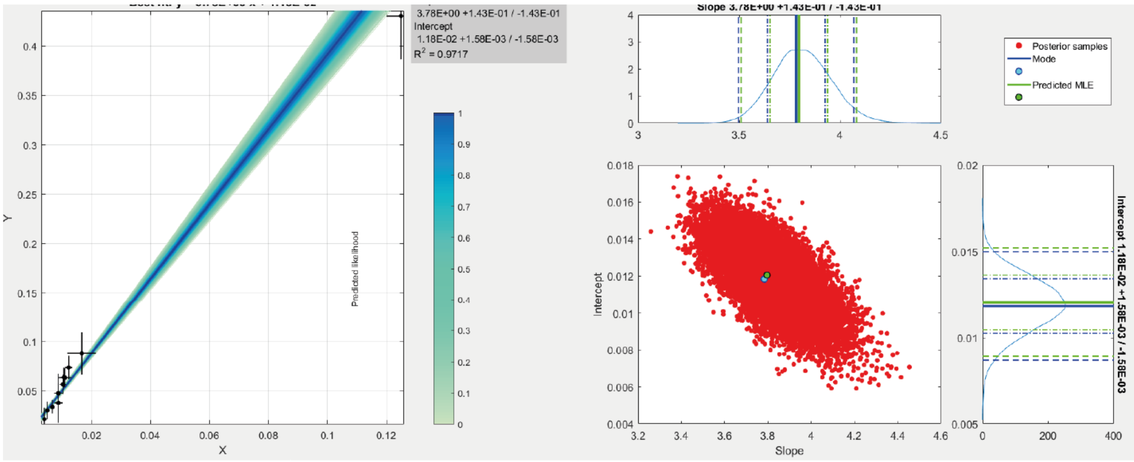

Fig. 51: ^{26}Al-^{10}Be plot of the Tromsberg site with the modelled linear regression after Bender et al. (2016)

The uncertainties of all samples were taken on the 2σ level. Consequently, the resulting 1σ error of the age calculated by the Bender code is also enhanced.

5.2.3 Iberig (TDS)

In total, ten samples were analysed, but only nine of them yielded ^{26}Al and ^{10}Be concentrations (Fig. 52). The Ibe55 sample did not yield enough material to press a target for AMS measurement. The calculated slopes and intercepts from the Granger and Bender codes differ slightly but are again in agreement within 1σ. The mean age estimates range from 0.79 to 0.65 Myr for the Granger and Bender codes, respectively (Fig. 52 – 53, Tab. 16).

Tab. 16: Output table from modelled age estimates using the Granger and Bender codes for Iberig

Calculation method	**Model output parameters**				**Calculated age estimate**	
	Mean slope [-]	**±1σ**	**Intercept** [at/g]	**±1σ**	**Mean age** [Myr]	**±1σ**
Granger	4.66	0.18	7'830	4'392	0.79	0.08
Bender	5.00	0.30	5'370	324	0.65	0.12

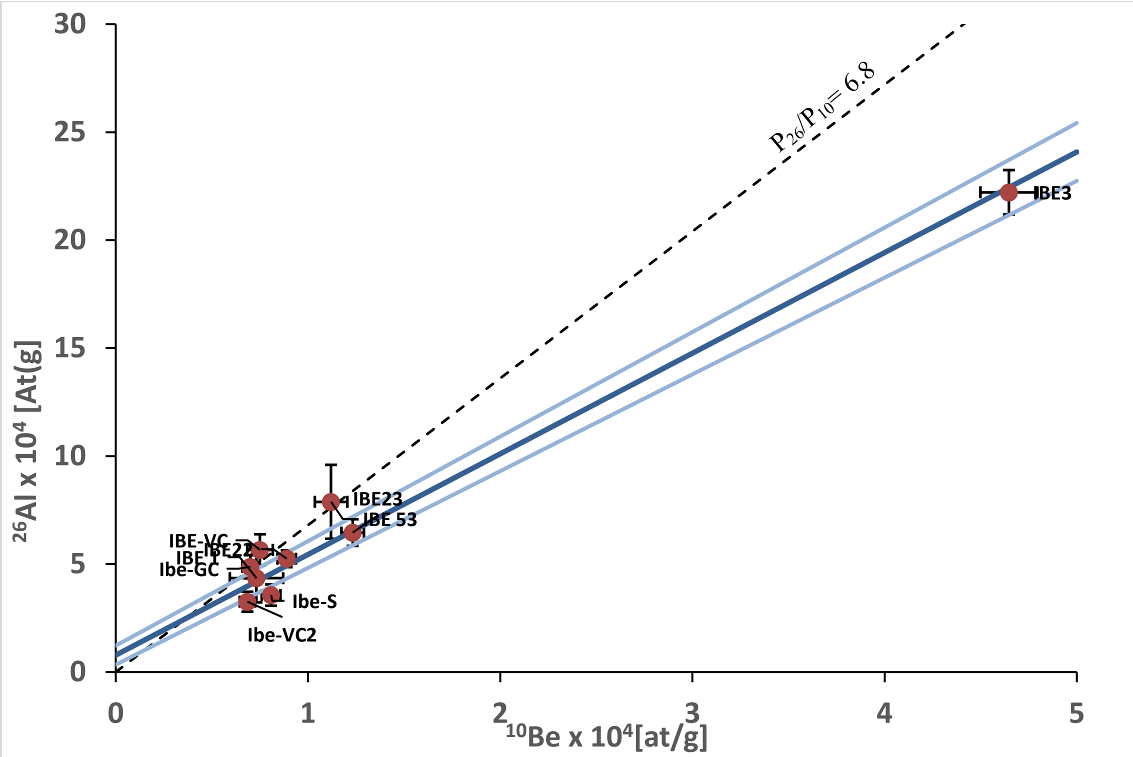

Fig. 52: ^{26}Al-^{10}Be plot of the Iberig site with the modelled linear regression Granger (2014)

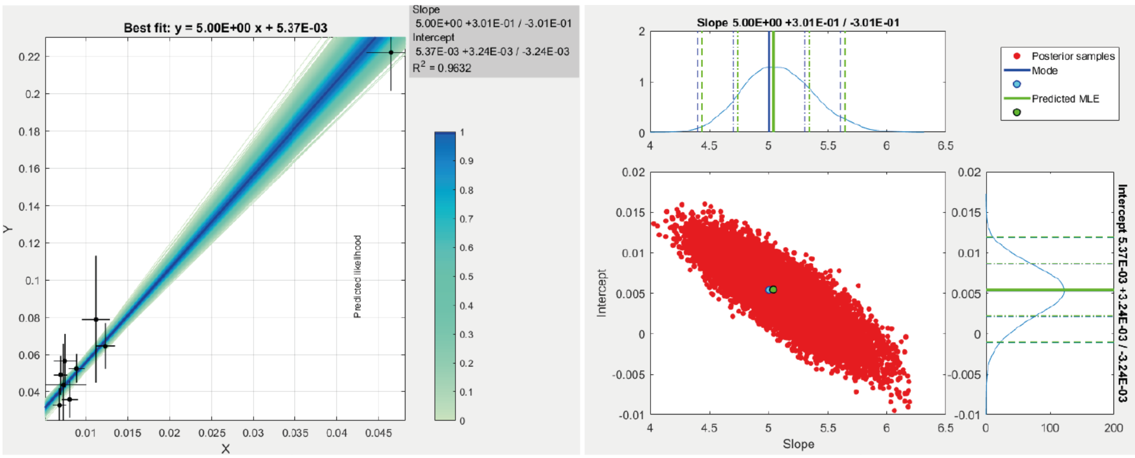

Fig. 53: ^{26}Al-^{10}Be plot of the Iberig site with the modelled linear regression Bender et al. (2016)

5.2.4 Beringen (HT)

In total, seven samples were analysed for their ^{26}Al and ^{10}Be concentration, but only three of them do not show an elevated ratio (Fig. 54). Therefore, the Ber1, Ber7 and Ber35 samples were chosen for regression analysis. Due to the close location of the sample concentration to the production ratio of $^{26}Al/^{10}Be$, a regression analysis is not straightforward as very young ages close to the present have to be expected (Fig. 54, Tab. 17). Therefore, the Ber35 sample with an $^{26}Al/^{10}Be$ of 6.30 was chosen to apply the true burial approach. The true burial age of Ber35 indicates an age of ~ 0.16 Myr.

Tab. 17: Output table from modelled age estimates using the Granger and Bender codes for Beringen

True burial was calculated using Eq. (1) and the sample Ber35.

Calculation method	**Model output parameters**				**Calculated age estimate**	
	Mean slope [-]	**±1σ**	**Intercept** [at/g]	**±1σ**	**Mean age** [Myr]	**±1σ**
True burial	6.30	0.96	-	-	0.160	0.30

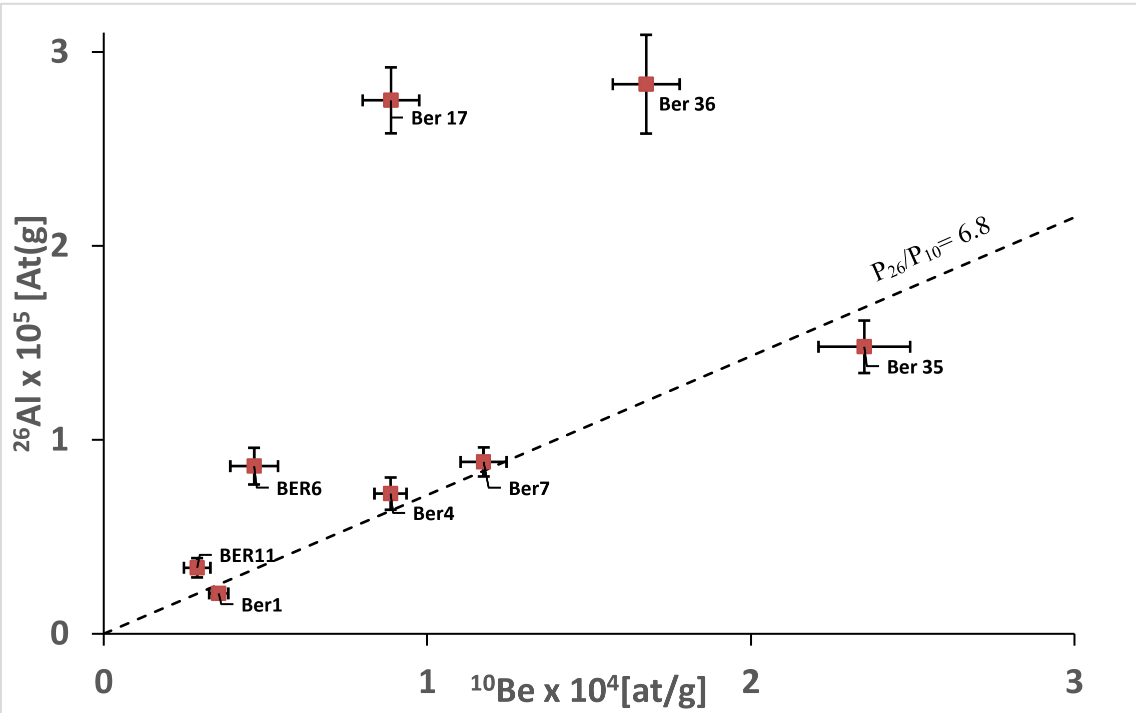

Fig. 54: ^{26}Al-^{10}Be plot from the Beringen samples

For the linear regression using the Granger code, only the Ber1, Ber7 and Ber35 samples were considered.

5.2.5 Glatt Valley (HT)

Two samples from the drill cores retrieved from the Glatt Valley were analysed (Fig. 55). The Gla1 sample was elevated and another sample yielded a rather modern ratio close to or higher than today's measured $^{26}Al/^{10}Be$ production ratio line of 6.8. As complete shielding by ice, water and later sediment was probably the case, true burial dating could have been applied, but since both the Granger and Bender codes require at least two datapoints, it was not possible to run a simulation by using the Gla3 sample alone. Furthermore, the Gla3 sample plots above the initial production ratio line and thus no modelling was performed. Additionally, true burial was not applied either (Tab. 18).

Tab. 18: Output table for the Glatt Valley site directly calculating the burial age from the sample nuclide ratio of Gla1

Calculation method	**Model output parameters**				**Calculated age estimate**	
	Mean slope [-]	**±1σ**	**Intercept** [at/g]	**±1σ**	**Mean age** [Myr]	**±1σ**
True burial	7.18	1.1	No post-burial production		Not determinable	

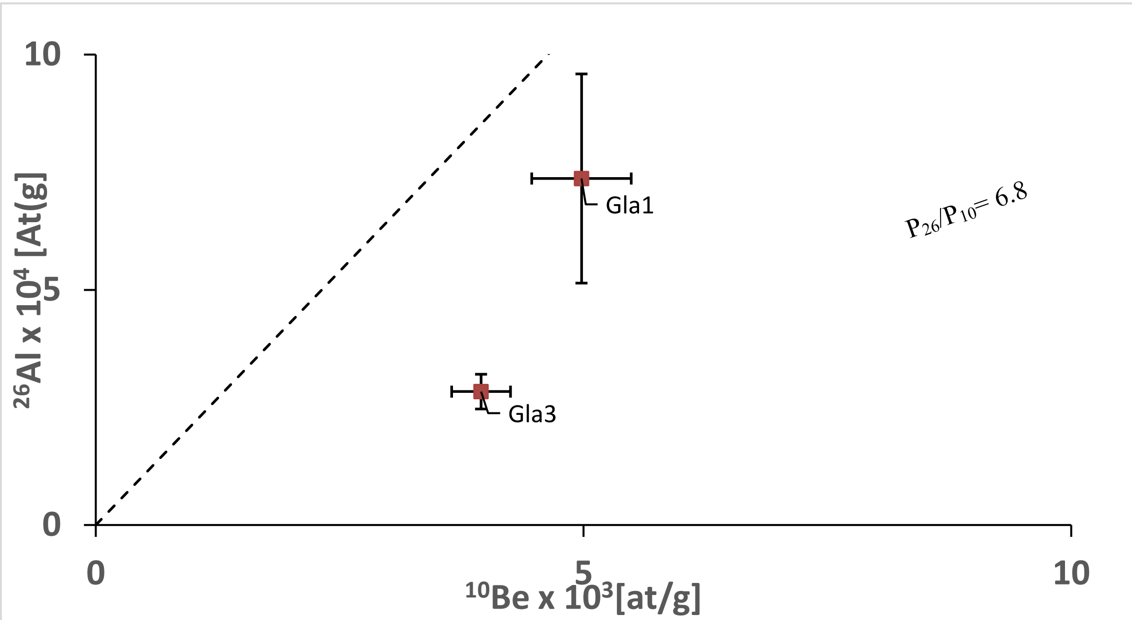

Fig. 55: ^{26}Al-^{10}Be plot from the Glatt Valley samples

The Gla1 sample was not considered for age calculation, therefore only the Gla3 sample remained for this purpose.

5.2.6 Comparison of the age estimates from the Granger and Bender codes

The mean slope and intercept parameters on the y-axis of the linear regression resulting from age modelling using either the Granger or Bender code are consistent for the Feusi (Tab. 14) and Beringen sites (Tab. 17). Mean slope and intercept with the y-axis from both codes are significantly different for the Tromsberg (Tab. 15) and Iberig (Tab. 16) sites. Consequently, the calculated ages either agree or differ in the mean value and its uncertainties (Fig. 56). However, the age estimates yielded by both codes overlap within 1σ uncertainty.

As already noted above in the previous sub-section, the Bender code only ran successfully when the sample uncertainties had to be doubled as documented for the Feusi, Tromsberg and Beringen sites, which might have a biasing and distorting effect. The resulting 1σ uncertainty of the mean age estimate also appears to be doubled.

Overall, the gravels of the Feusi and Tromsberg sites from the Höhere Deckenschotter appear to have accumulated before 1 Myr or even before 1.5 Myr. The Tiefere Deckenschotter at the Iberig site may have accumulated significantly after 1 Myr before present, i.e. between 0.6 and 0.8 Myr. Finally, the two sites for Hochterrasse gravels, i.e. the valley fillings in Beringen, yielded a modern age due to being close to the methodological limit but with uncertainty ranging back to ~ 0.2 Myr. However, the current database is not sufficient to conclude that original OSL ages can be confirmed.

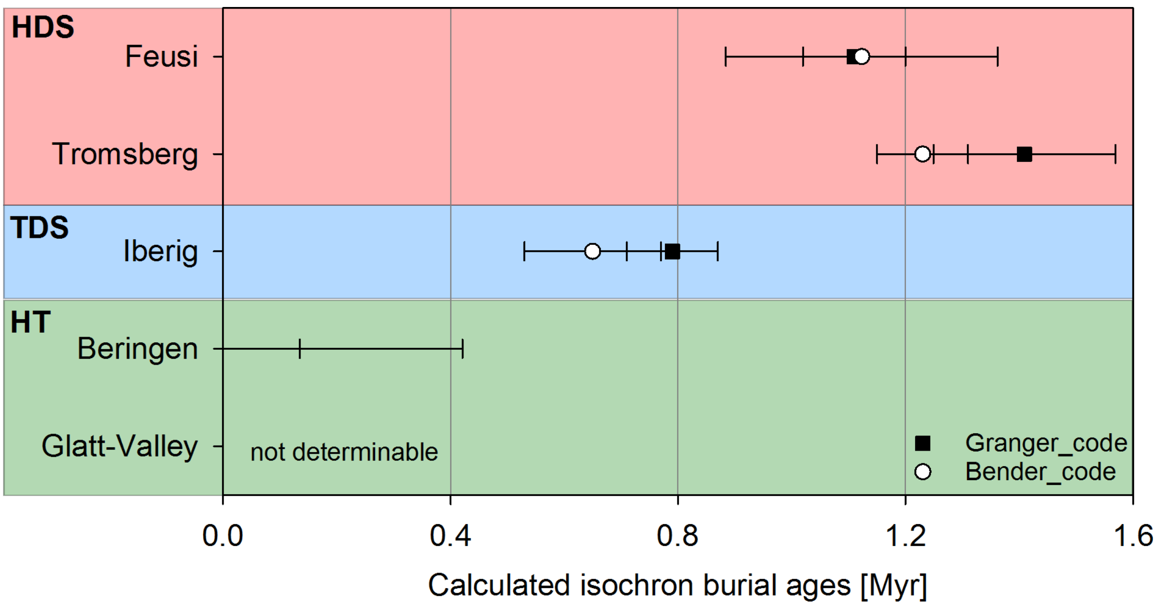

Fig. 56: Comparison of calculated age estimates with 1σ uncertainties from the Bender and Granger codes

For the Beringen site, the lower 1σ range is negative and therefore not plotted in this graph. For the Glatt Valley site, it was not possible to obtain an age.

5.3 Exposure-erosion banana plot

The erosion–burial diagram ("banana" plot) shows the $^{26}Al/^{10}Be$ ratio as a function of [^{10}Be] that is normalised to sea-level-high latitude (Fig. 57). Plotting the samples of all three sites, Tromsberg, Iberig and Feusi, shows a noisy pattern of normalised ^{10}Be concentrations between 10^3 and 10^4 at/g and – more importantly – various ratios between 8 and 3. As for isochron burial dating, the observed range of normalised ^{10}Be concentrations provides an insight into the potential erosion rate at the source which might range from a few m/kyr to several cm/kyr, i.e. a few mm/yr down to 0.01 mm/yr. These values of erosion rates are typical for the Alps, at least for modern Alpine erosion rates (cf. Wittmann et al. 2007).

Samples plotting along the same burial isoline across different erosion rate windows enable the estimation of a simple burial age for the sediments sampled (assuming there is no post-burial production, Granger (2006). Because post-burial production raises the $^{26}Al/^{10}Be$ ratio above what it would otherwise be, shallowly buried samples will always appear younger than their true age. For samples with significant post-burial production, the simple burial dating method thus indicates a minimum burial age (Granger 2014). Therefore, the vertical spread of the data points in the plot for each site suggest that the vertically distributed samples are plotting at higher ratios due to their – assumedly - predominant post-burial production. Post-burial production becomes dominant in the total nuclide concentration of a sample if the initially inherited concentration was already very low (e.g. 5 to 10×10^4 at/g ^{10}Be for rapidly eroding surfaces at the source) and further decayed due to radioactive decay. One strength of isochron burial dating and plotting the data in a ^{26}Al-^{10}Be plot is to identify possible outliers plotting below the isochron. However, in cases where the dataset consists of one main point cloud and a single data point far away from the point cloud, identifying outliers might be difficult. Here the erosion-burial diagram (Fig. 57) could help by identifying samples that plot far below the burial isoline of site-specific samples (see below for explanations).

For the Feusi site, the three samples with the lowest ^{26}Al /^{10}Be ratios plot between the 1.2 and 1.4 Myr burial isoline, whereas all other samples show vertical spread. The vertical spread could be reasonably explained by a predominant post-burial signal and sample-specific ratios higher than the actual ones resulting from burial without post-burial production. A comparison with the 1σ uncertainty range of isochron burial age of 1.05 – 1.20 Myr shows that a minimum age of 1.2 Myr seems to support the isochron age estimate. This apparent coincidence of the age ranges strongly supports the argument regarding the estimation of age uncertainties (see following discussion).

The situation for the samples at the Tromsberg site is less clear. One sample plots slightly below the isolines of 1.4 Myr and one sample plots slightly below the isoline of 1.0 Myr. All other samples plot separately with burial ages of 0.7 Myr and younger. This contrasting pattern of the low(er) ratios of the two samples (Tro27 and Tro33) indicates that they might be reworked. If so, then the calculated isochron age estimate is wrong as the age is controlled by the regression fitted through the sample Tro33 plotting far away from the other data points. More data are needed for this site to constrain the age. Because of this issue with a single controlling data point, comparing simple burial ages based on the erosion-burial diagram with the isochron burial age is not feasible. At least a minimum burial age of 0.7 Myr for Tromsberg could be derived.

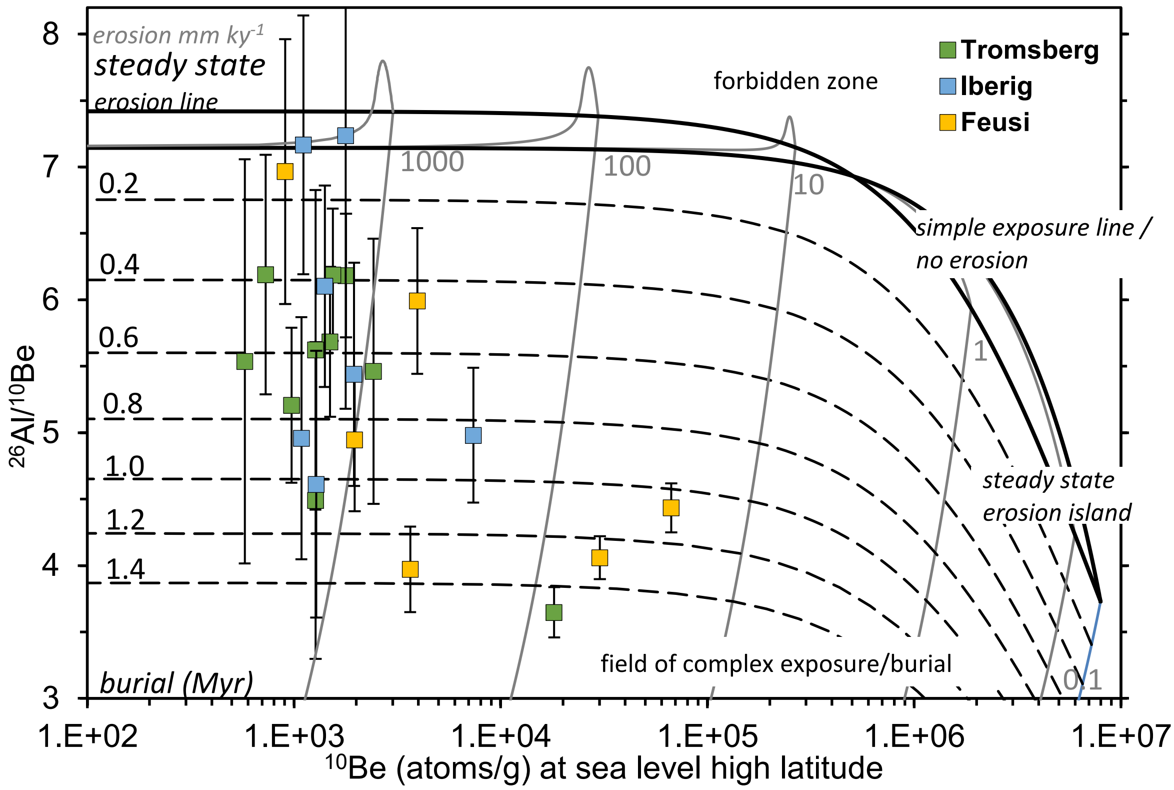

Fig. 57: Erosion-burial plot based on an initial $^{26}Al/^{10}Be$ production ratio of 6.8

The ^{10}Be concentration of the samples is normalised to sea-level-high latitude based on the ^{10}Be production rate scaled to the specific sampling sites (following Stone 2000). For comparison, see Fig. 25.

Again, quite a significant overlap of the minimum burial age and the isochron burial age is represented by the samples of the Iberig site. The burial age of the two lowest sample ratios indicate a minimum age range of 0.8 to 1.0 Myr, which is consistent with the isochron burial estimate of 0.6 to 0.8 Myr. However, the isochron burial age estimate is again controlled by a single datapoint located far away from the other point cloud. Nevertheless, the fact that at least two samples plot along a similar burial isoline is promising and supports the isochron burial age despite the limited dataset. For the Iberig site also, additional data are needed to constrain the age estimates.

A complication obscuring the rather simple erosion-burial plot might arise when the samples had a strongly different input ratio due to different erosion styles (e.g. lowered initial ratios with very low erosion rates, see the right plunging side of the banana in Section 3.2.). Since the different input ratios are not a priori known from measurement due to radioactive decay, it might be difficult to compare them. Therefore, interpretations based solely on the erosion-burial diagram should be regarded with caution.

6 Discussion

6.1 Assessment of the data

In this sub-section, the measured data are briefly discussed, and the limits of the datasets are indicated. This is followed by a discussion of the samples with elevated $^{26}Al/^{10}Be$ ratios which were not considered for the regression analysis. Finally, the choice of the initial production ratio is explained.

6.1.1 Measured data

The presented dataset covering all five sites consists of a total of 41 individual samples. Rejecting samples with elevated ratios (see discussion below) leads to a finalised dataset of 30 samples. For the sites with isochron burial – the sites consisting of Deckenschotter – finalised datasets of 6 samples each for Feusi, 10 samples for Iberig and 11 samples for Tromsberg are available. For the sites based on the true/simple burial method, the finalised datasets are much lower with 3 and 1 data points for Beringen and the Glatt Valley, respectively. While the total available number of data points for each site seems to be promising, one has to bear in mind that, for both Iberig and Tromsberg, one single sample and a point cloud steer the entire isochron regression fit. In contrast, the Feusi site shows a very consistent regression fit from very low to very high nuclide concentrations.

Based on this qualitative data assessment, it is reasonable to conclude that the Tromsberg and Iberig sites need a few additional data points to constrain the dataset and the regression fit. In particular, samples with higher nuclide concentrations are required to further constrain or discard the single sample steering of the regression. However, selecting samples with high nuclide concentrations is a trial and error process and impossible to predict. There is no shortcut indicating low or high nuclide concentrations. Therefore, the only way is to process samples and measure their nuclide concentrations.

In the literature, typical numbers of samples reported for isochron burial dating range from 2 – 5 (Çiner et al. 2015, Zhao et al. 2017) or 6 to 10 samples (Akçar et al. 2017, Darling et al. 2012, Zhao et al. 2016). However, as explained above, the required spread represented by the data points to obtain a meaningful regression line is much more decisive than the total number. Based on a larger dataset of at least 10 samples, the modelled age estimates become more robust and outlier samples with $^{26}Al/^{10}Be$ ratios that are either too high or too low can be more easily rejected from the regression (e.g. Bender et al. 2016, Darling et al. 2012). Çiner et al. (2015) presented an isochron burial plot with only five data points but a sufficiently high spread, allowing a solid regression analysis. However, this study was conducted in the arid, desert-like environment of Turkey.

6.1.2 Elevated $^{26}Al/^{10}Be$ ratios

In Section 4.1.2, the elevated, physically impossible $^{26}Al/^{10}Be$ ratios (above 9, thus no overlap within 1σ with 6.8, the initial production ratio of $^{26}Al/^{10}Be$) were interpreted to be a result of a combination of chemical/technical problems occurring in the laboratory and with AMS/ICP-MS. This line of reasoning is congruent with the interpretations of many other authors. For example, Erlanger et al. (2012) and Bender et al. (2016) classify the plotting of samples in the forbidden zone above the line of the initial production ratio of $^{26}Al/^{10}Be$ as a result of laboratory error.

In contrast, Akçar et al. (2017) and later also Braumann et al. (2018) explained elevated ratios – especially in glacial samples - as a result of muon production. At depth, where muon production is dominant and spallation ceases, the $^{26}Al/^{10}Be$ production ratio is around 8.3 or 8.4 at/g/yr (Braucher et al. 2013, Braucher et al. 2011). It has been assumed that a pebble plucked by glacial erosion at depth would carry the elevated $^{26}Al/^{10}Be$ signature. More recently, elevated ratios were presented in the study by Litty et al. (2018). However, the samples were sourced from a non-glaciated catchment and thus the explanation with elevated production ratios induced by glacial erosion failed. Accordingly, the elevated ratios were explained as an artefact resulting from laboratory errors.

In summary, very few authors explain elevated ratios with physical-geological processes, whereas the majority interpret them as a laboratory error. As our repeated sample measurements showed above, there is a high likelihood of laboratory errors, which could explain the elevated ratios in our dataset. Besides this, samples with ratios below the initial production ratio could also be affected by laboratory errors.

6.1.3 Assessment of correct initial production ratios

Isochron burial dating is based on the difference between the fitted regression through the measured $^{26}Al/^{10}Be$ ratios and the initial $^{26}Al/^{10}Be$ production ratio. For a long time, the latter has been assumed to be a canonical value of 6.75:1 $^{26}Al:^{10}Be$, which is nearly independent of latitude and altitude (Balco & Rovey 2008). Until now, this value has been used in all published studies describing fluvial landscapes where the initial isochron slope is assumed to correspond to the surface ratio (e.g. Balco & Rovey 2008, Bender et al. 2016, Darling et al. 2012, Erlanger et al. 2012). As already mentioned in the previous sub-section, Akçar et al. (2017) suggested applying the production ratio of 8.4 for samples likely originating from depth, as is the case for glacial samples such as pebbles and blocks being plucked while a glacier erodes them. Since the authors could not determine which value between 6.8 and 8.4 was the correct one, they applied the mean of 6.8 and 8.4 which is 7.6 ± 0.8 $^{26}Al/^{10}Be$ (Fig. 58). The presented production ratios of Akçar et al. (2017) are not based on ratios of measured data. The difference between a production ratio and a measured concentration ratio and its impact on the selection of the most appropriate initial production ratio will be discussed in the next section.

Currently, the subject of elevated production ratios at depth is a matter of debate in the scientific community. For this purpose, G. Balco (Berkeley Geochronology Center), who is an expert in the field and who invented the isochron burial method, was asked for his opinion. Although Balco did not perform any calculations specific to the samples we have measured, he provided a general outline of the important distinction between the instantaneous *production* ratio and the observed *concentration* ratio, which we summarise here. If a sample is exposed at, for example, 5 metres depth where production is predominantly the result of muon interactions, then the $^{26}Al/^{10}Be$ production ratio is > 8. If the sample starts off with zero nuclide concentration and sits there for a short time, such as a few tens of thousands of years, then the concentration ratio will also be > 8. However, it is difficult to propose any situation where a sample really (i) has zero nuclide concentrations, (ii) arrives at 5 m depth and remains there for a short time, and (iii) is then transported to whatever site one is interested in. It is nearly impossible for (i) to be true, because the question is, where the sample was before it was at 5 m depth. It must have arrived at that depth by gradual exhumation and, because muon production is spread over a very wide depth range, samples spend a long time in the zone of muon production. Even if the long-term erosion rate is 100 m/Myr, samples spend hundreds of thousands of years in the zone of muon production. Thus, the $^{26}Al/^{10}Be$ *concentration* ratio will be much lower than the *production* ratio because of radioactive decay. In other words, it is very difficult for a sample to really have a *concentration* ratio > 8. It has to be very rapidly transported from some very deep location and then reside for a very short time at moderate depth. If this does happen, there is a limit on how high the concentration can be – if the concentration at burial is higher than, e.g., 50'000 years times the production rate at depth (which is only approximately 2000 atoms/g ^{10}Be at 1'000 m elevation), then it is impossible for the concentration ratio to be equal to the production ratio – it must be lower because of decay. Therefore, if one hypothesises that the concentration ratio was > 8, then that places a strict limit on how high the absolute concentration can be. If the concentration is higher, then the sample must have resided in the muon production zone long enough for radioactive decay to have reduced the concentration ratio below the production ratio. The overall point is that it is true that the production ratio is greater than 8 for muon production, but that does not mean that it is likely that one will ever encounter a sample with a concentration ratio of > 8, and, furthermore, it is impossible to encounter this ratio unless the concentration is very low. Following Balco (pers. comm.), the only samples in the presented datasets that could have had a concentration ratio of > 8 at the time they were buried are the ones with a very low concentration off to the far left of the plot (Fig. 57). The ones with higher concentrations must have been either (i) exposed for a long time at muon production depths, in which case the concentration ratio would be much lower than the production ratio due to radioactive decay, or (ii) exposed for a shorter time at shallow depths, in which case the production ratio would be close to 6.75.

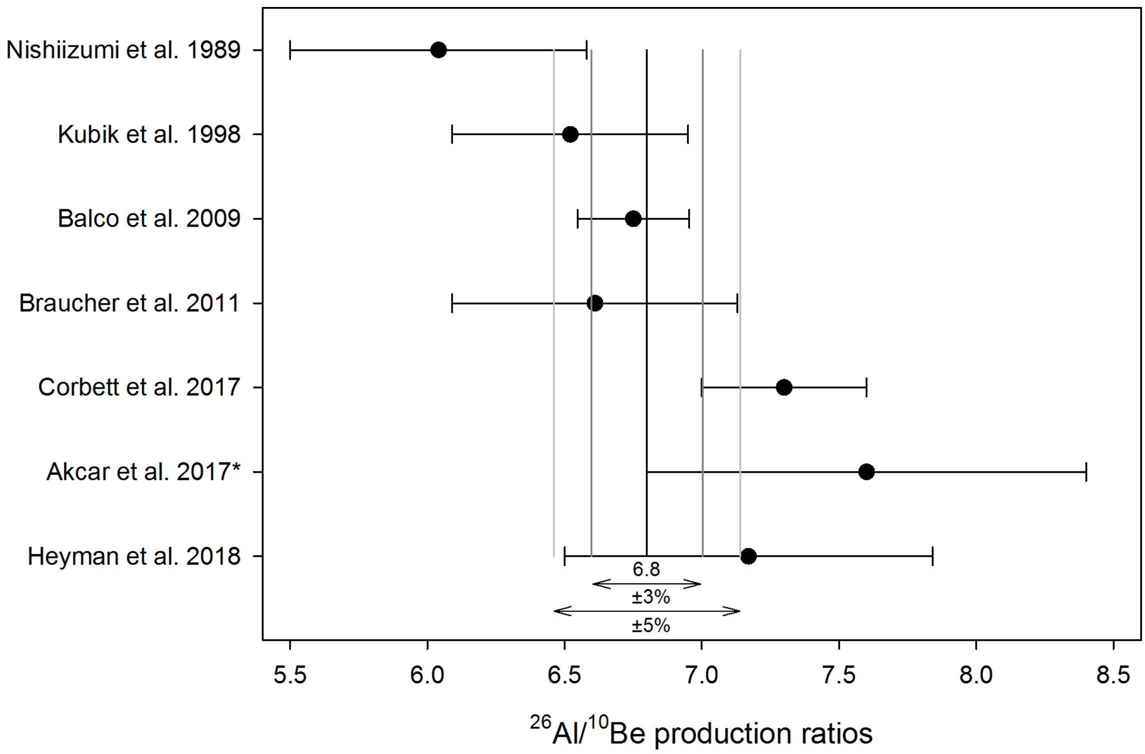

Fig. 58: Compilation of the most relevant initial production ratios used for $^{26}Al/^{10}Be$

Note, this compilation is not exhaustive. The ratio is not based on measured data but is suggested to apply for samples likely sourced by glacial erosion (cf. Akçar et al. 2017). The chosen value of 6.8 with conservative 5 % uncertainty overlaps well with most recent estimates of production ratios. Heyman et al. (2018) refer to the global compilation available online (http://expage.github.io/).

Due to these arguments, the initial production ratio of $^{26}Al/^{10}Be$ is set to 6.8 following Balco & Rovey (2008). Currently, other estimates are available for the initial production ratios that are all based on ratios of measured data (cf. Fig. 58), e.g. 7.3 for surface production ratio in Greenland (Corbett et al. 2017) or 7.17 from a global compilation (J. Heyman, pers. comm.; http://expage.github.io/). According to Heyman, the ^{26}Al and ^{10}Be production rates vary somewhat differently geographically, the ratio will vary with latitude and elevation, and the ratio of 7.17 is the reference value for a theoretical site at high latitude and low elevation. Heyman calculated the production ratio for a theoretical site potentially representing the source of Deckenschotter samples at 47°N/9°E for altitudes of 2'000 and 3'000 m of 7.03 and 6.96, respectively.

In order to account for this certain variability in the initial production ratio of $^{26}Al/^{10}Be$, a conservative error of 5 % was assumed, which covers the range from 6.46 to 7.14. The latter value is slightly higher than the commonly assumed 3 % uncertainty for the canonical value of 6.8 (Granger 2014).

A conservative range of production ratios is considered to represent the assumed variation of concentration ratios that the samples assembled prior to burial. The concentration ratios might vary slightly depending on the governing erosion rate and previous exposure time. However, the erosion rate and set-up for each single sample cannot be resolved within this study and is therefore included in the 1σ range of the production ratio.

6.1.4 Error propagation into age uncertainties

In the following, an error propagation of four main error sources or uncertainties is performed including uncertainties in the decay constants of ^{10}Be (1 %) and ^{26}Al (3 %) (Chmeleff et al. 2010; Korschinek et al. 2010; Nishiizumi, 2004), the initial production ratio of $^{26}Al/^{10}Be$ that was conservatively set to 5 % (see above) and the uncertainty arising from linear regression fitted through the dataset. All errors are propagated on the 1σ-level.

For a systematic and clear routine for carrying out uncertainty propagation, Eq. (3) according to Balco & Rovey (2008) that is used for the burial age calculation is derived based on the measured ratio (slope of linear regression, Eq. (4), initial ratio (Eq. (5)), the ^{26}Al decay constant (Eq. (6)) and the ^{10}Be decay constant (Eq. (7). The square root of the squares of these four derivatives yields the 1σ range of the burial age (Eq. (8).

$$t_b = \frac{-ln\,\frac{R_M}{R_{init}}}{(\lambda_{26} - \lambda_{10}}$$

Eq. (3): Where t_b is the burial duration equal to the age of sediment deposition, $\lambda_{26,10}$ represents the decay constants of ^{26}Al and ^{10}Be, and R_M, R_{init} the measured and initial ratio of ^{26}Al and ^{10}Be.

$$\frac{\partial}{\partial R_M}\,(Eq.3) = \frac{1}{R_M\,(\lambda_{10} - \lambda_{26})}$$

Eq. (4): Derivative of Eq. (2) for the measured ratio (the slope calculated from the regression).

$$\frac{\partial}{\partial_{init}}(Eq.3) = \frac{1}{R_{init}\,(\lambda_{26} - \lambda_{10})}$$

Eq. (5): Derivative of Eq. (2) for the initial production ratio.

$$\frac{\partial}{\partial\lambda_{26}}(Eq.3) = \frac{-ln\,\frac{R_M}{R_{init}}}{(\lambda_{26} - \lambda_{10})^2}$$

Eq. (6): Derivative of Eq. (2) for the 26Al decay constant.

$$\frac{\partial}{\partial\lambda_{10}}(Eq.3) = \frac{-ln\,\frac{R_M}{R_{init}}}{(\lambda_{26} - \lambda_{10})^2}$$

Eq. (7): Derivative of Eq. (2) for the 10Be decay constant.

$$\sigma_{t_b} = \sqrt{(Eq.4 \times \sigma_M)^2 + (Eq.5 \times \sigma_{init})^2 + (Eq.6 \times \sigma_{26})^2 + (Eq.7 \times \sigma_{10})^2}$$

Eq. (8): Calculation of the 1σ uncertainty using the squares of Eq. (3), (4), (5) and (6).

The site-specific age uncertainties are calculated in line with the equations presented above and are listed in Tab. 19. For the sake of consistency, the output results based on the Granger code were used for all three sites (see the corresponding tables in the results chapter). As the relative errors of the slope from the linear regression of around 4.3 % are similar, the absolute age uncertainties are similar as well. For the older Feusi and Tromsberg sites, the age uncertainties of ~ 140 kyr result in a rather low relative error of 10 – 12 %. The young Iberig site has a relative uncertainty of 20 %. The presented age uncertainties are comparable if the slightly different procedure of Granger & Muzikar (2001) is taken. Therefore, the age uncertainties can be considered to represent a robust and conservative estimate with the most important uncertainties taken into account.

Tab. 19: Table listing all uncertainties considered for the final calculations using the equations (3) – (6)

Name site	**Modelled mean age** [Myr]	**Modelled slope** [-]	**Rel. error**				**Rel. error age**	**Abs. age uncertainty**
			R_M (slope)	**R_{init}**	**λ_{26Al}**	**λ_{10Be}**	**1σ** [%]	**1σ** [Myr]
Feusi	1.11	3.98	4.5 %	5 %	3 %	1 %	14.2 %	0.16
Tromsberg	1.41	3.45	4.3 %	5 %	3 %	1 %	11.7 %	0.16
Iberig	0.79	4.69	3.8 %	5 %	3 %	1 %	17.8 %	0.14

6.2 Assessment of burial /isochron burial age estimates

In the following, the final 1σ age intervals are calculated and discussed in terms of their reliability (Tab. 20). The discussion is separated into the Höhere and Tiefere Deckenschotter sites (Section 5.2.1) and Hochterrasse (Section 5.2.2).

Tab. 20: Overview for the three sites with the final 1σ age intervals and the estimated reliability

Name site	**Stratigraphic**	**Modelled**	**Age uncertainty**	**1σ age interval**	**Estimated reliability**
	Unit	**Mean age** [Myr]	**1σ** [Myr]	[Myr]	
Feusi	HDS	1.11	0.15	0.96 – 1.26	Reliable and robust Minimum burial age = isochron age
Tromsberg	HDS	1.41	0.16	1.25 – 1.57	Unreliable, awaits more data Isochron age = maximum age? Minimum burial age = 0.7 Myr?
Iberig	TDS	0.79	0.14	0.65 – 0.93	Likely reliable, awaits more data Minimum burial age = isochron age
Beringen	HT	0.16	*(0.30)*	-	No age uncertainty possible due to data point close to detection limit
Glatt Valley	HT	Negative	-	-	No age estimates possible due to data scatter

6.2.1 Höhere and Tiefere Deckenschotter (Feusi, Tromsberg and Iberig)

The calculated 1σ age intervals are 0.96 – 1.26 Myr for the Feusi site, 1.25 – 1.57 Myr for the Tromsberg site and 0.65 – 0.93 Myr for the Iberig site. However, the spread of the data for Tromsberg and Iberig is not as ideal as for the Feusi site. For Feusi, a robust and solid dataset exists with seven datapoints that are aligned from very high to very low ^{26}Al-^{10}Be concentrations, whereas for the Tromsberg and Iberig sites, a point cloud at very low concentrations and one single sample steering the linear regression are available. The location of the single sample with high concentrations controls the slope and thus the calculated age. Based on this fact (see Section 5.1.1), the calculated ages of Tromsberg and Iberig represent preliminary ages and await more samples constraining the regression.

To further assess the reliability and robustness of the calculated ages, the exposure-erosion plot (banana plot) could help through the indicated minimum burial ages of 1.0 Myr for Tromsberg and 0.8 Myr for Iberig. Consequently, for Tromsberg the potential age range of gravel accumulation might be between 1.0 and 1.4 Myr based on this available preliminary dataset, and therefore the isochron burial age might represent rather a maximum age. For the Iberig site, the minimum burial age matches the isochron burial age well, indicating that the calculated age of 0.65 – 0.95 Myr might be reliable. Adding 1 – 2 more datapoints to constrain the regression further would support the age.

For the Feusi site, the calculated age of 1 to 1.3 Myr is interpreted to represent a robust age estimate for the till accumulation at this site. The glaciofluvial gravels, located further north at the Siglistorf site in the presumably identical spatially linked sediment deposit, were also dated using isochron burial (Akçar et al. 2017). The age of Feusi overlaps well with the slightly higher age of 1.1 to 1.5 Myr of Siglistorf (using the ages based on the initial production ratio of 6.75 presented in the paper).

6.2.2 Hochterrasse (Beringen and Glatt Valley)

The mean age estimates for the Beringen site indicate a very young age and cannot be further resolved due to the data quality. For the Glatt Valley, the data quality is even worse, and its age cannot be distinguished from the present. Accordingly, the true age of the sediment deposit might be close to the method's lower detection limit of 100 or 200 kyr (Balco & Rovey 2008, Granger 2014).

The following conclusion can be drawn from studying these two Hochterrasse sites: Because of too low concentrations and missing differentiation to the measurement background, cosmogenic pilot studies for the age determination of samples from the Beringen gravel pit and the Glatt Valley drill core are currently not productive, and no reliable age estimate for the two sites can be made.

6.3 Landscape evolution model based on cosmogenic data

The duration of past glaciations has been inferred by proxies for temperature such as by the global marine oxygen isotope record of the last 3.5 Myr that is based on the $\delta^{18}O$ of benthic foraminifera (Lisiecki & Raymo 2005). The foraminiferal $\delta^{18}O$ is a function of the temperature and $\delta^{18}O$ of the water in which it forms, and the $\delta^{18}O$ signal of seawater is a function of global ice volume and water salinity. Based on such data, the turnover from predominantly 41 kyr of glacier fluctuations before the Mid-Pleistocene Transition (from 1.2 to 0.7 Myr) to predominantly 100 kyr of glacier fluctuations was detected (Ruddiman et al. 1989). The obtained isochron ages plus the isochron age from Siglistorf (Akçar et al. 2017) and the biostratigraphic age from Irchel (Bolliger et al. 1996) are plotted versus the global stack of $\delta^{18}O$ of benthic foraminifera according to Lisiecki and Raymo (2005) in order to learn about potential driving mechanisms of Deckenschotter deposition (Fig. 59). Accordingly, the Feusi, Tromsberg and Siglistorf sites coincide with the beginning of the Mid-Pleistocene Transition, where the amplitudes of the $\delta^{18}O$ curve start to increase. Higher amplitudes have been suggested to indicate more ice in general and stronger ice ages with glaciers reaching up to the foreland (Lisiecki & Raymo 2005). The age of Iberig site coincides with the end of the Mid-Pleistocene Transition, when a clear 100 kyr glacier cyclicity was established with longer glacier cycles and larger ice mass resulting in glaciations that reached the foreland (Graf 1993, Kuhlemann & Rahn 2013).

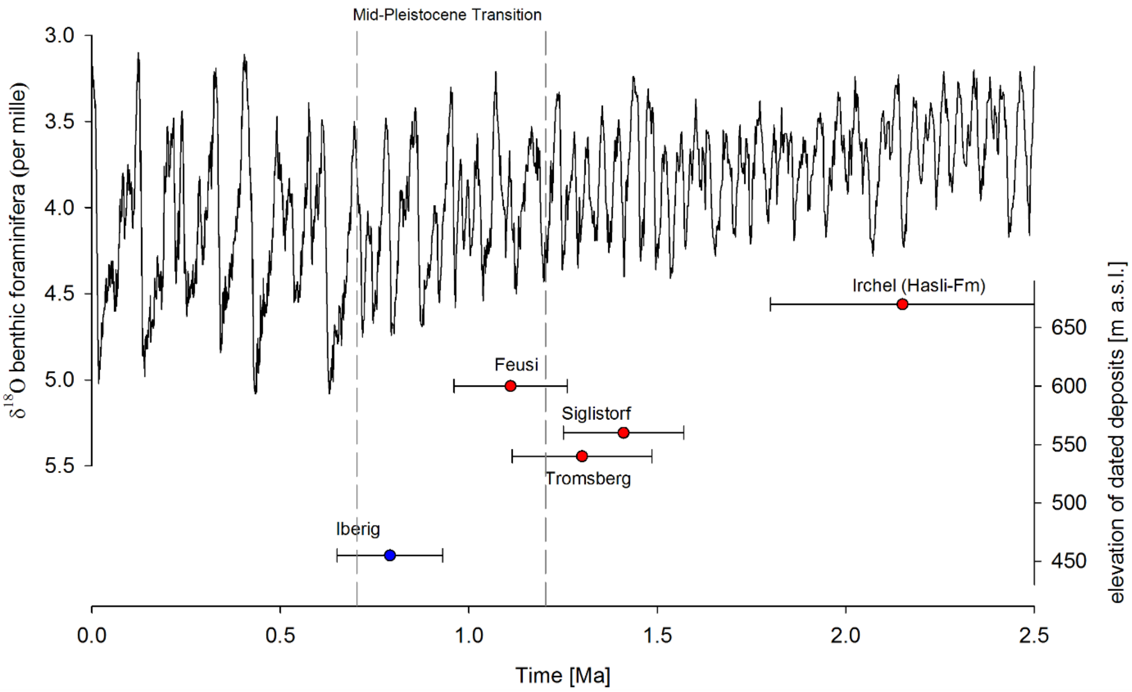

Fig. 59: $\delta^{18}O$ data from benthic foraminifera (Lisiecki & Raymo 2005) compared with the isochron burial data from this study and from Siglistorf (Akçar et al. 2017) and the age inferred from mammal teeth (Bolliger et al. 1996)

Red points indicate Höhere Deckenschotter units and blue points Tiefere Deckenschotter.

The ^{26}Al-^{10}Be concentrations were primarily used to constrain the timing of gravel accumulation. However, comparing the absolute concentrations measured for the five sites in this study can be used to better understand the landscape history. The inheritance – the ^{26}Al-^{10}Be concentrations as interplay of production and erosion at the source site – can be used to infer landscape erosion. Low erosion rates lead to a high nuclide concentration, whereas fast erosion and high erosion rates cause a drop in the nuclide concentration (Lal 1991). A landscape with predominantly glacial erosion processes is expected to contain sediments in its drainage system with a typically low nuclide signature. A slowly eroding landscape, e.g. due to a mild climate, weakly developed relief and drainage system, produces sediments with a high nuclide signature (Portenga & Bierman 2011).

In the conceptual landscape evolution model that will be presented in the following, the focus lies on the cosmogenic data observed in this study, the occurrence of 41 and 100 kyr glacier cycles and the estimated accumulation ages of the deposits (Fig. 60). A very simplified geometry of the cross-section of the Alps and the foreland was used. For the purposes of simplicity and easier visualisation, the elevation dependence of cosmogenic nuclide production (exponential increase with elevation) was ignored. Furthermore, direct transport from the source (the Alps) to the sink (the foreland) was assumed with no intermediate storage or reworking. Based on these assumptions the data suggest that:

(1) In the Early Pleistocene, prior to ~ 1.4 Myr, the predominantly 41 kyr glacial cycles possibly fluctuated within the inner Alps and were likely restricted to cirque glaciations (Fig. 60A). Low landscape erosion rates led to an ongoing enrichment of cosmogenic nuclides in the upper surface and thus to high concentrations within the exposed bedrock. According to conservative estimates of back-calculated inherited concentrations from the Feusi site, Alpine erosion rates were probably significantly below 0.1 mm/yr.

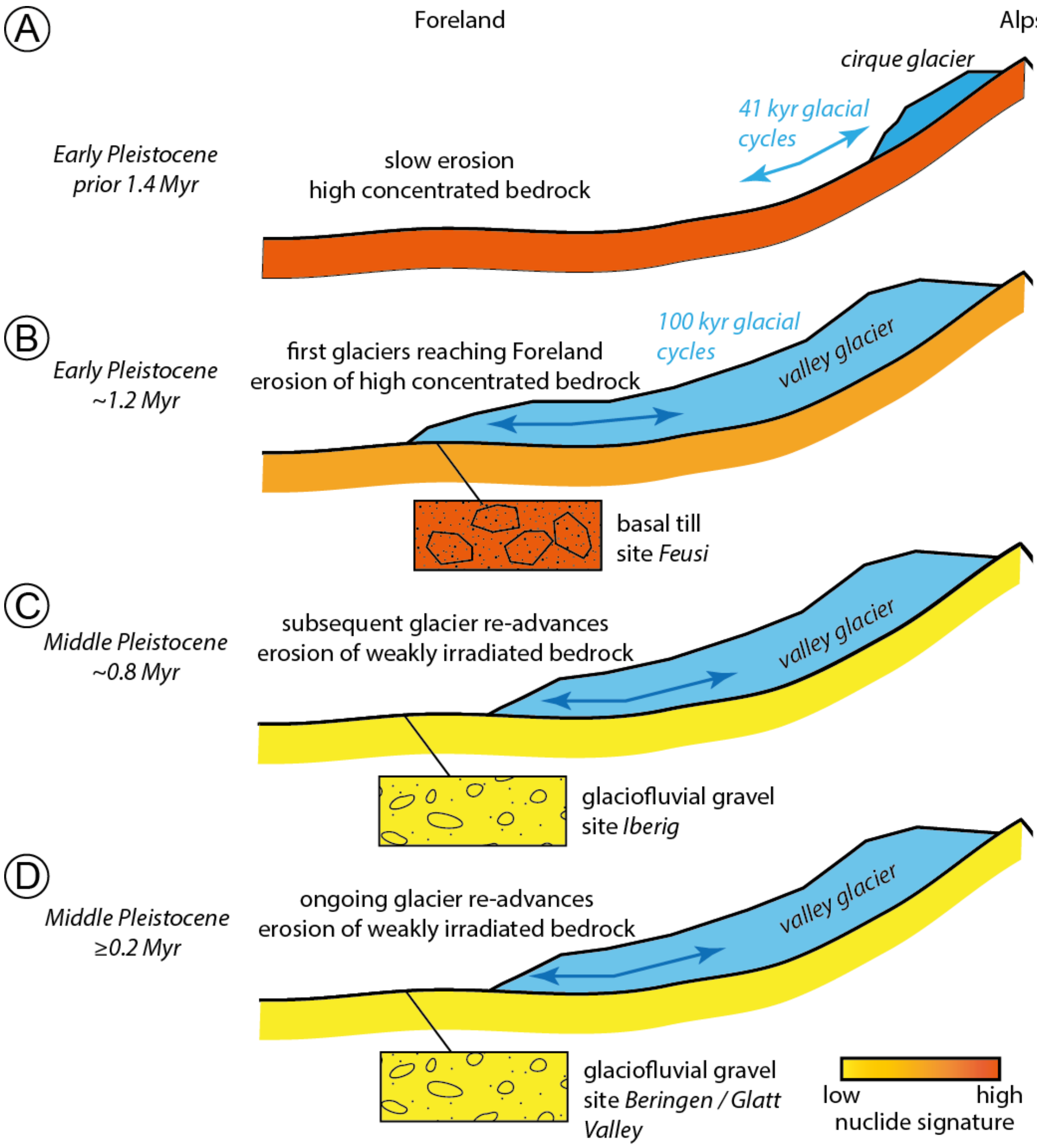

Fig. 60: Landscape evolution model based on the cosmogenic nuclide data from all five sites

Assumptions and simplifications: very simplified geometries of Alpine topography and glaciers, elevation dependence of cosmogenic production not considered, direct transport source to sink assumed (no storage/reworking).

(2) Around 1.2 Myr, as visible from the increasing amplitudes in the $\delta^{18}O$ records, the glacial cycles increased their cyclicity from 41 kyr to 100 kyr within the Mid-Pleistocene Transition (Fig. 60B). As a result, colder conditions form larger ice masses and the first glaciers reach the Alpine foreland. On its way to the foreland, bedrock with high levels of accumulated nuclide concentrations are eroded and deposited as till as observed at the Feusi site.

(3) Towards the end of the Mid-Pleistocene Transition around 0.8 Myr (Fig. 60C), several glaciations reaching the foreland must have occurred as revealed by morphostratigraphy (e.g. Graf 1993). The continuous erosion of bedrock and at least partial shielding by ice and sediments likely led to a reduced accumulation of cosmogenic nuclides. Consequently, the nuclide signature of the eroded gravels and sands measured at the Tromsberg (assumed here that the real age is much younger than the preliminary age of 1.4 Myr) and Iberig sites are low.

Later in the Middle Pleistocene (between 0.8 to 0.2 Myr), repeated glaciations caused a further drop to very low nuclide concentrations as is indicated in Beringen and the Glatt Valley. Note that both sites are likely not overprinted by post-burial production due to their assumed complete shielding. Therefore, the nuclide signature from these deposits might reflect a true signal induced by glacial processes.

7 Conclusion

7.1 Achievements

In this project, the two most relevant dating methods based on cosmogenic nuclides, depth profile and (isochron) burial dating, were thoroughly assessed and discussed. In the following, the main achievements are summarised.

Assessment of ^{10}Be depth profile dating:

- Synthetic models and different tested approaches revealed that ^{10}Be depth profiles applied to river terraces in Middle Europe quickly (~ 0.2 Myr) achieve steady state due to rather high profile erosion rates (> 1 cm/kyr) and are therefore not suitable for dating terraces of presumably Middle Pleistocene age or older.
- Particularly, it has been shown in this work that the ^{10}Be depth profile of Stadlerberg (Claude et al. 2017) cannot be used to determine a depositional age with any degree of confidence.

^{26}Al/^{10}Be burial dating:

- Systematic testing of different cleaning routines to achieve pure quartz low in ^{27}Al (< 100 ppm) revealed that Al found inside the quartz lattice – in contrast to Al present in non-quartz minerals – cannot be removed by continued etching and separation.
- The sampling sites for isochron burial dating were selected based on classification criteria applied to the established outcrop catalogue of potential sites in the Swiss foreland.
- Two sites from the Höhere and one from the Tiefere Deckenschotter were selected: Feusi (Egg) and Tromsberg (Dürn-Gländ) as well as Iberig. For the Hochterrasse unit, the valley filling at the Beringen site and Glatt Valley (a drill core) were selected. Due to a sufficient burial depth and negligible post-burial production, both sites were investigated using the true/simple burial dating method.
- A ^{26}Al/^{10}Be dataset of 41 samples is presented for all five sites. With the dataset for the Feusi site (HDS), a reliable and robust age range of 0.95 – 1.3 Myr can be constrained. The other Deckenschotter sites Tromsberg (HDS) and Iberig (TDS) are within the 1.25 –1.55 Myr and 0.65 – 0.95 Myr range. Due to the regression analysis being driven by a point cloud and a single outlier, the age constraints are potentially less reliable and raise the need for further measured samples. For the datasets for the Hochterrasse sites Beringen and Glatt Valley, age data scatter prevented age determination.
- A systematic error propagation of all systematic errors such as production and decay parameters was applied to the calculated mean ages.
- The observed pattern of ^{26}Al/^{10}Be concentrations was successfully interpreted in terms of a landscape evolution model based on cosmogenic nuclide data. The relatively higher ^{26}Al/^{10}Be concentrations at the Feusi site found within till can be explained by one of the first glacier advances to the Alpine foreland, scraping off bedrock enriched in nuclide concentrations possibly due to low erosion rates. The relatively lower ^{26}Al/^{10}Be concentrations found at the Iberig and Tromsberg sites are explained as a result of ongoing glaciations since the Mid-Pleistocene Transition which likely occurred within 1 – 1.3 Myr.

7.2 Incomplete knowledge, uncertainties

In this section, the most relevant uncertainties for this study and knowledge deficits to better constrain the accumulation ages of the Deckenschotter are briefly discussed.

Methodological aspects:

- Fundamental assumption of the same initial production ratio for all samples might have to be rejected (decreasing $^{26}Al/^{10}Be$ ratios for very low erosion rates, towards the right, plunging side of the banana plot).
- Fundamental assumption of negligible intermediate storage of samples leading to samples with lower $^{26}Al/^{10}Be$ ratios, but this could be detected. But what if all samples are reworked?
- Too high $^{26}Al/^{10}Be$ ratios particularly for low concentrations. AMS interferences and unknown systematic errors for ICP-MS measurements might be the cause for an excess of ^{26}Al. However, excessive ^{26}Al is predominant for very low concentrations (below 10^5 ^{26}Al at/g) and probably within the measurement uncertainties for higher nuclide concentrations.

Chronological aspects:

- First estimates of depositional ages of the Deckenschotter sites could be established for three sites: Feusi and Tromsberg (HDS) and Iberig (TDS).
- Age constraint for Hochterrasse samples measured in Beringen and Glatt Valley was not possible due to data scatter.

In terms of extracting and measuring the nuclides, there is always a certain potential to improve the extraction routine and preparation of the AMS targets. A significant improvement has been made between the first sample batch and the following one using the described modifications appropriate for low nuclide concentrations (see Section 4.1.1). Despite these initial improvements, there are $^{26}Al/^{10}Be$ ratios that are unphysically high and irreproducible. Nevertheless, working in such a rapidly eroding Alpine environment with such low initial $^{26}Al/^{10}Be$ concentrations and long burial times is not as straightforward as in other settings. Therefore, modifications to improve the final AMS/ICP measurements in the laboratory are an ongoing process and the sum of all the small modifications will result in better measurement precision and accuracy.

7.3 Recommendations for further sampling sites

Based on the landscape evolution model (Fig. 60), some recommendations can be made for further sampling sites. Ideally, the quartz of the sampled pebbles has low ^{27}Al content but simultaneously rather high ^{26}Al concentration to have a rather high $^{26/27}Al$ ratio measured by the AMS. Given this, and following the landscape evolution model, the aim should be to date the highest and presumably oldest Deckenschotter sites with ^{26}Al-^{10}Be isochron burial as their likelihood of high ^{26}Al-^{10}Be concentrations is higher. Therefore, to achieve a high precision of analytical data and thus well-constrained isochron regressions, the topographically highest terraces related to the Höhere Deckenschotter units should be preferred and prioritised. Besides the already dated Feusi and Irchel sites, the Uetliberg site might be an option. The base of the Deckenschotter at Uetliberg lies at an elevation of 850 m and is described as a sequence of glaciofluvial gravels with underlying tills (Buechi et al. 2018).

For further sites, the reader is referred to the outcrop catalogue (Appendix C). However, the outcrop catalogue was based on this newest evidence as presented in the landscape model, and it is not exhaustive as many available sites remain. However, most of them are either poorly described or overgrown by vegetation and thus their potential for carrying out sedimentological and geochronological work is rather low.

As the sediment layer at the Feusi site was a till, it would be interesting to date additional tills in Höhere or Tiefere Deckenschotter. For example, the Stammerberg site located southwest of the village Stein am Rhein is built up of gravels and an intercalated layer of glacial sediments with scratched pebbles (Graf 2009 and references therein). Dating this till and comparing the nuclide concentrations with those of the Feusi site would further constrain the landscape model and give geochronological evidence for glaciers in the foreland during the time of accumulation of the Tiefere Deckenschotter.

Besides searching for and selecting new sites, it is strongly recommended to measure a few further samples for the Tromsberg and Iberig sites to enhance the reliability of the linear regression and thus the calculated accumulation age of the sediment deposit.

7.4 Open questions

The presented accumulation ages of the Deckenschotter and the related landscape evolution model raise several further questions. According to the landscape evolution model, it is proposed that no glaciation reached the Alpine foreland prior to 1.2 Myr. This assumption has to be justified with further research, e.g. at the more highly elevated Irchel site. There, the glaciofluvial gravels that are stratigraphically lower than the age estimate of the Hasli Formation in the MN17 zone (1.8 – 2.6 Myr, Bolliger et al. (1996) indicate a nearby glacier. No evidence for till at the Irchel site has been found so far (Graf 1993 and references therein). Ultimately, the question remains whether the age estimate for the Hasli Formation is correct or not.

A further question is whether the rather simple classification of the Deckenschotter (Graf 1993 and references therein) with more highly elevated sites equalling older ages and vice-versa is still valid. Currently, the presented ages of Höhere Deckenschotter being older than 1 Myr and Tiefere Deckenschotter being younger than 1 Myr apparently do not challenge the classical chronostratigraphy. However, the age discrepancy between Höhere Deckenschotter at the Irchel site with a biostratigraphic age of ~ 2 Myr (altitude of 670 m for the Hasli Formation) and the Feusi site (altitude of ~ 600 m) with an age of ~ 1.1 Myr indicate that at least the Höhere Deckenschotter could be divided into two different chronostratigraphic units, similarly to an earlier proposal by Graf & Müller (1999).

This work presents cosmogenic $^{26}Al/^{10}Be$ data from three sites of Deckenschotter deposits in the Swiss foreland. Adding a modelling component to the measured data would be of high importance to further solve open questions such as the "right" initial production ratio, intermediate storage of sediment, credibility of modelled ages, etc. This would require an Alpine perspective tracking the $^{26}Al/^{10}Be$ signatures of particles from the source to the sink with adapted boundary conditions and parameters. In this modelling environment, for example, a wide range of erosion rates at the source (glacial and non-glacial erosion processes) and different erosion rates at the sink and related production contributions could be tested. Ideally, comparing measured data with modelled data will yield a complete and integrated understanding of timing and geological processes of Deckenschotter formation. A modelling study is currently ongoing under the lead of Prof. M. Knudsen of the University of Aarhus. The reader is referred to reports and papers published by them for further information.

8 References

Akçar, N., Ivy-Ochs, S., Alfimov, V., Claude, A., Graf, H.R., Dehnert, A., Kubik, P.W., Rahn, M., Kuhlemann, J. & Schlüchter, C. (2014): The first major incision of the Swiss Deckenschotter landscape: Swiss journal of geosciences, v. 107, no. 2-3, p. 337-347.

Akçar, N., Ivy-Ochs, S., Alfimov, V., Schlunegger, F., Claude, A., Reber, R., Christl, M., Vockenhuber, C., Dehnert, A., Rahn, M. & Schluchter, C. (2017): Isochron-burial dating of glaciofluvial deposits: First results from the Swiss Alps: Earth Surface Processes and Landforms, v. 42, no. 14, p. 2414-2425.

Anderson, R.S., Repka, J.L. & Dick, G.S. (1996): Explicit treatment of inheritance in dating depositional surfaces using in situ Be-10 and Al-26: Geology, v. 24, no. 1, p. 47-51.

Argento, D.C., Reedy, R.C. & Stone, J.O. (2013): Modeling the earth's cosmic radiation: Nuclear Instruments & Methods in Physics Research Section B-Beam Interactions with Materials and Atoms, v. 294, p. 464-469.

Balco, G. & Rovey, C.W. (2008): An Isochron Method for Cosmogenic-Nuclide Dating of Buried Soils and Sediments: American Journal of Science, v. 308, no. 10, p. 1083-1114.

Balco, G., Finnegan, N., Gendaszek, A., Stone, J.O.H. & Thompson, N. (2013): Erosional Response to Northward-Propagating Crustal Thickening in the Coastal Ranges of the Us Pacific Northwest: American Journal of Science, v. 313, no. 8, p. 790-806.

Bender, A.M., Amos, C.B., Bierman, P.R., Rood, D., Staisch, L.M., Kelsey, H.M. & Sherrod, B. (2016): Differential uplift and incision of the Yakima River terraces, central Washington State: Journal of Geophysical Research, v. 121, no. 1, p. 365-384.

Bolliger, T., Fejfar, O., Graf, H. & Kälin, D. (1996): Vorläufige Mitteilung über Funde von pliozänen Kleinsäugern aus den höheren Deckenschottern des Irchels (Kt. Zürich): Eclogae Geologicae Helvetiae, v. 89, no. 3, p. 1043-1048.

Braucher, R., Bourles, D., Merchel, S., Romani, J.V., Fernadez-Mosquera, D., Marti, K., Leanni, L., Chauvet, F., Arnold, M., Aumaitre, G. & Keddadouche, K. (2013): Determination of muon attenuation lengths in depth profiles from in situ produced cosmogenic nuclides: Nuclear Instruments & Methods in Physics Research Section B-Beam Interactions with Materials and Atoms, v. 294, p. 484-490.

Braucher, R., Brown, E.T., Bourles, D.L. & Colin, F. (2003): In situ produced Be-10 measurements at great depths: implications for production rates by fast muons: Earth and Planetary Science Letters, v. 211, no. 3-4, p. 251-258.

Braucher, R., Del Castillo, P., Siame, L., Hidy, A.J. & Bourles, D.L. (2009): Determination of both exposure time and denudation rate from an in situ-produced Be-10 depth profile: A mathematical proof of uniqueness. Model sensitivity and applications to natural cases: Quaternary Geochronology, v. 4, no. 1, p. 56-67.

Braucher, R., Merchel, S., Borgomano, J. & Bourles, D.L. (2011): Production of cosmogenic radionuclides at great depth: A multi element approach: Earth and Planetary Science Letters, v. 309, no. 1-2, p. 1-9.

Braumann, S.M., Neuhuber, S., Fiebig, M., Schaefer, J. M., Hintersberger, E. & Lüthgens, C. (2018): Challenges in constraining ages of fluvial terraces in the Vienna Basin (Austria) using combined isochron burial and pIRIR225 luminescence dating: Quaternary International.

Brown, E.T., Brook, E.J., Raisbeck, G.M., Yiou, F. & Kurz, M.D. (1992): Effective Attenuation Lengths of Cosmic-Rays Producing Be-10 and Al-26 in Quartz - Implications for Exposure Age Dating: Geophysical Research Letters, v. 19, no. 4, p. 369-372.

Buechi, M.W., Deplazes, G. & Anselmetti, F.S. (2018): Sedimentology of the glacial facies within the Deckenschotter of Northern Switzerland: Poster presentation at Swiss Geoscience Meeting in Bern.

Buechi, M.W., Frank, S.M., Graf, H.R., Menzies, J. & Anselmetti, F.S. (2017a): Subglacial emplacement of tills and meltwater deposits at the base of overdeepened bedrock troughs: Sedimentology, v. 64, no. 3, p. 658-685.

Buechi, M.W., Lowick, S.E. & Anselmetti, F.S. (2017b):, Luminescence dating of glaciolacustrine silt in overdeepened basin fills beyond the last interglacial: Quaternary Geochronology, v. 37, p. 55-67.

Cerling, T.E. & Craig, H. (1994): Geomorphology and in-Situ Cosmogenic Isotopes: Annual Review of Earth and Planetary Sciences, v. 22, p. 273-317.

Chmeleff, J., von Blanckenburg, F., Kossert, K. & Jakob, D. (2010): Determination of the Be-10 half-life by multicollector ICP-MS and liquid scintillation counting: Nuclear Instruments & Methods in Physics Research Section B-Beam Interactions with Materials and Atoms, v. 268, no. 2, p. 192-199.

Christl, M., Vockenhuber, C., Kubik, P.W., Wacker, L., Lachner, J., Alfimov, V. & Synal, H.A. (2013): The ETH Zurich AMS facilities: Performance parameters and reference materials: Nuclear Instruments and Methods in Physics Research Section B: Beam Interactions with Materials and Atoms, v. 294, p. 29-38.

Çiner, A., Doğan, U., Yıldırım, C., Akçar, N., Ivy-Ochs, S., Alfimov, V., Kubik, P.W. & Schlüchter, C. (2015): Quaternary uplift rates of the Central Anatolian Plateau, Turkey: insights from cosmogenic isochron-burial nuclide dating of the Kızılırmak River terraces: Quaternary Science Reviews, v. 107, p. 81-97.

Claude, A., Akçar, N., Ivy-Ochs, S., Schlunegger, F., Kubik, P.W., Dehnert, A., Kuhlemann, J., Rahn, M. & Schlüchter, C. (2017): Timing of early Quaternary gravel accumulation in the Swiss Alpine Foreland: Geomorphology, v. 276, p. 71-85.

Claude, A., Akçar, N., Ivy-Ochs, S., Schlunegger, F., Kubik, P.W., Christl, M., Vockenhuber, C., Kuhlemann, J., Rahn, M. & Schlüchter, C. (2019): Changes in landscape evolution patterns in the Northern Swiss Alpine Foreland during the mid-Pleistocene revolution: GSA Bulletin.

Corbett, L.B., Bierman, P.R., Rood, D.H., Caffee, M.W., Lifton, N.A. & Woodruff, T.E. (2017): Cosmogenic 26Al/10Be surface production ratio in Greenland: Geophysical Research Letters, v. 44, no. 3, p. 1350-1359.

Darling, A.L., Karlstrom, K.E., Granger, D.E., Aslan, A., Cole, R.D., Kirby, E., Ouimet, W.B., Lazear, G.D. & Coblentz, D.D. (2012): New incision rates along the Colorado River system based on cosmogenic burial dating of terraces: Implications for regional controls on Quaternary incision: Geosphere, v. 8, no. 5, p. 1020-1041.

Dehnert, A. & Schlüchter, C., 2008, Sediment burial dating using terrestrial cosmogenic nuclides: Eiszeitalter und Gegenwart (Quaternary Science Journal), v. 57, p. 210-225.

Delmas, M., Braucher, R., Gunnell, Y., Guillou, V., Calvet, M., Bourles, D. & Team, A. (2015): Constraints on Pleistocene glaciofluvial terrace age and related soil chronosequence features from vertical Be-10 profiles in the Ariege River catchment (Pyrenees, France): Global and Planetary Change, v. 132, p. 39-53.

Delmas, M., Calvet, M., Gunnell, Y., Voinchet, P., Manel, C., Braucher, R., Tissoux, H., Bahain, J.J., Perrenoud, C., Saos, T. & Team, A. (2018): Terrestrial Be-10 and electron spin resonance dating of fluvial terraces quantifies quaternary tectonic uplift gradients in the eastern Pyrenees: Quaternary Science Reviews, v. 193, p. 188-211.

Doppler, G., Kroemer, E., Rögner, K., Wallner, J., Jerz, H. & Grottenthaler, W. (2011): Quaternary stratigraphy of southern Bavaria: E&G–Quaternary Science Journal, v. 60, no. 2-3, p. 329-365.

Dunai, T.J. (2010): Cosmogenic Nuclides: Principles, Concepts and Applications in the Earth Surface Sciences, Cambridge: Cambridge University Press.

Ellwanger, D., Wielandt-Schuster, U., Franz, M. & Simon, T. (2011): the Quaternary of the southwest German Alpine Foreland (bodensee-oberschwaben, baden-Württemberg, southwest Germany): Quaternary Science Journal, v. 60, no. 2-3, p. 306-328.

Erlanger, E.D., Granger, D.E. & Gibbon, R.J. (2012): Rock uplift rates in South Africa from isochron burial dating of fluvial and marine terraces: Geology, v. 40, no. 11, p. 1019-1022.

Gosse, J.C. & Phillips, F.M. (2001): Terrestrial in situ cosmogenic nuclides: theory and application: Quaternary Science Reviews, v. 20, no. 14, p. 1475-1560.

Graf, H. & Müller, B. (1999): Das Quartär: Die Epoche der Eiszeiten: Geologie des Kantons Zürich. Ott Verlag, Thun, p. 71-95.

Graf, H.R. (1993): Die Deckenschotter der zentralen Nordschweiz: Zürich.

Graf, H.R. (2009): Stratigraphie und Morphogenese von frühpleistozänen Ablagerungen zwischen Bodensee und Klettgau: E&G Quaternary Sci. J., v. 58, no. 1, p. 12-54.

Graf, H.R., Bitterli-Dreher, P., Burger, H., Bitterli, T., Diebold, P. & Naef, H. (2006): Geologischer Atlas der Schweiz. 1070 Baden (Atlasblatt 120). Karte 1:25000.: Bundesamt für Landestopografie, swisstopo, Wabern.

Granger, D. (2014): Cosmogenic nuclide burial dating in archaeology and paleoanthropology.

Granger, D.E. (2006): A review of burial dating methods using (26) Al and (10) Be: In Situ-Produced Cosmogenic Nuclides and Quantification of Geological Processes, v. 415, p. 1-16.

Granger, D.E. & Muzikar, P.F. (2001): Dating sediment burial with in situ-produced cosmogenic nuclides: theory, techniques, and limitations: Earth and Planetary Science Letters, v. 188, no. 1-2, p. 269-281.

Granger, D.E. & Smith, A.L. (2000): Dating buried sediments using radioactive decay and muogenic production of Al-26 and Be-10: Nuclear Instruments & Methods in Physics Research Section B-Beam Interactions with Materials and Atoms, v. 172, p. 822-826.

Haldimann, P., Graf, H.R. & Jost, J. (2017): Geologischer Atlas der Schweiz. 1071 Bülach (Atlasblatt 151). Erläuterungen: Bundesamt für Landestopografie, swisstopo, Wabern.

Häuselmann, P., Fiebig, M., Kubik, P. & Adrian, H. (2007): A first attempt to date the original "Deckenschotter" of Penck and Brückner with cosmogenic nuclides: Quaternary International, v. 164, p. 33-42.

Heisinger, B., Lal, D., Jull, A.J.T., Kubik, P., Ivy-Ochs, S., Knie, K. & Nolte, E. (2002a): Production of selected cosmogenic radionuclides by muons: 2. Capture of negative muons: Earth and Planetary Science Letters, v. 200, no. 3-4, p. 357-369.

Heisinger, B., Lal, D., Jull, A.J.T., Kubik, P., Ivy-Ochs, S., Neumaier, S., Knie, K., Lazarev, V. & Nolte, E. (2002b): Production of selected cosmogenic radionuclides by muons 1. Fast muons: Earth and Planetary Science Letters, v. 200, no. 3-4, p. 345-355.

Heisinger, B., Lal, D., Jull, A.J.T., Kubik, P.W., Ivy-Ochs, S., Neumaier, S., Knie, K., Lazarev, V. & Nolte, E. (2002c): Production of selected cosmogenic radionuclides by muons: Geochimica Et Cosmochimica Acta, v. 66, no. 15a, p. A558-A558.

Hidy, A.J., Gosse, J.C., Pederson, J.L., Mattern, J.P. & Finkel, R.C. (2010): A geologically constrained Monte Carlo approach to modeling exposure ages from profiles of cosmogenic nuclides: An example from Lees Ferry, Arizona: Geochemistry Geophysics Geosystems, v. 11.

Hidy, A.J., Pederson, J.L., Cragun, W. S. & Gosse, J. (2005): Cosmogenic 10Be exposure dating of Colorado river terraces at Lees Ferry, Arizona, *in* Proceedings Geological Society of America Annual Meeting 2005.

Ivy-Ochs, S. (2015): Glacier variations in the European Alps at the end of the last glaciation: Cuadernos de investigación geográfica/Geographical Research Letters, no. 41, p. 295-315.

Ivy-Ochs, S., Kerschner, H., Reuther, A., Preusser, F., Heine, K., Maisch, M., Kubik, P.W. & Schluchter, C. (2008): Chronology of the last glacial cycle in the European Alps: Journal of Quaternary Science, v. 23, no. 6-7, p. 559-573.

Ivy-Ochs, S., Schäfer, J., Kubik, P. W., Synal, H.-A. & Schlüchter, C. (2004): Timing of deglaciation on the Northern Alpine foreland (Switzerland): Eclogae Geologicae Helvetiae, v. 97, no. 1, p. 47-55.

Jordan, P. (2010): Analysis of overdeepened valleys using the digital elevation model of the bedrock surface of Northern Switzerland: Swiss Journal of Geosciences, v. 103, no. 3, p. 375-384.

Keller, B. (1996): Lithofazies-Codes für die Klassifikation von Lockergesteinen: Mitteilungen der Schweizerischen Gesellschaft für Boden- und Felsmechanik, v. 4, p. 5-12.

Klein, J., Giegengack, R., Middleton, R., Sharma, P., Underwood, J. & Weeks, R. (1986): Revealing histories of exposure using in situ produced 26 Al and 10 Be in Libyan desert glass: Radiocarbon, v. 28, no. 2A, p. 547-555.

Kong, P., Granger, D.E., Wu, F.Y., Caffee, M.W., Wang, Y.J., Zhao, X.T. & Zheng, Y. (2009): Cosmogenic nuclide burial ages and provenance of the Xigeda paleo-lake: Implications for evolution of the Middle Yangtze River: Earth and Planetary Science Letters, v. 278, no. 1-2, p. 131-141.

Korschinek, G., Bergmaier, A., Faestermann, T., Gerstmann, U.C., Knie, K., Rugel, G., Wallner, A., Dillmann, I., Dollinger, G., von Gostomski, C.L., Kossert, K., Maiti, M., Poutivtsev, M. & Remmert, A. (2010): A new value for the half-life of Be-10 by Heavy-Ion Elastic Recoil Detection and liquid scintillation counting: Nuclear Instruments & Methods in Physics Research Section B-Beam Interactions with Materials and Atoms, v. 268, no. 2, p. 187-191.

Kubik, P.W., Ivy-Ochs, S., Masarik, J., Frank, M. & Schluchter, C. (1998): Be-10 and Al-26 production rates deduced from an instantaneous event within the dendro-calibration curve, the landslide of Kofels, Otz Valley, Austria: Earth and Planetary Science Letters, v. 161, no. 1-4, p. 231-241.

Kuhlemann, J. & Rahn, M. (2013): Plio-Pleistocene landscape evolution in Northern Switzerland: Swiss Journal of Geosciences, v. 106, no. 3, p. 451-467.

Lal, D. (1991): Cosmic ray labeling of erosion surfaces: in situ nuclide production rates and erosion models: Earth and Planetary Science Letters, v. 104, no. 2-4, p. 424-439.

Lal, D., Barg, E. & Pavich, M. (1991): Development of Cosmogenic Nuclear Methods for the Study of Soil-Erosion and Formation Rates: Current Science, v. 61, no. 9-10, p. 636-640.

Laloy, E., Beerten, K., Vanacker, V., Christl, M., Rogiers, B. & Wouters, L. (2017): Bayesian inversion of a CRN depth profile to infer Quaternary erosion of the northwestern Campine Plateau (NE Belgium): Earth Surface Dynamics, v. 5, no. 3, p. 331-345.

Lifton, N., Sato, T. & Dunai, T. J. (2014): Scaling in situ cosmogenic nuclide production rates using analytical approximations to atmospheric cosmic-ray fluxes: Earth and Planetary Science Letters, v. 386, p. 149-160.

Lisiecki, L.E. & Raymo, M.E. (2005): A Pliocene-Pleistocene stack of 57 globally distributed benthic δ18O records: Paleoceanography, v. 20, no. 1.

Litty, C., Schlunegger, F., Akçar, N., Delunel, R., Christl, M. & Vockenhuber, C. (2018): Chronology of alluvial terrace sediment accumulation and incision in the Pativilca Valley, western Peruvian Andes: Geomorphology, v. 315, p. 45-56.

Lowick, S.E., Buechi, M.W., Gaar, D., Graf, H.R. & Preusser, F. (2015): Luminescence dating of Middle Pleistocene proglacial deposits from Northern Switzerland: methodological aspects and stratigraphical conclusions: Boreas, v. 44, no. 3, p. 459-482.

Lupker, M., Blard, P.H., Lave, J., France-Lanord, C., Leanni, L., Puchol, N., Charreau, J. & Bourles, D. (2012): Be-10-derived Himalayan denudation rates and sediment budgets in the Ganga basin: Earth and Planetary Science Letters, v. 333, p. 146-156.

Mifsud, C., Fujioka, T. & Fink, D. (2013): Extraction and purification of quartz in rock using hot phosphoric acid for in situ cosmogenic exposure dating: Nuclear Instruments and Methods in Physics Research Section B: Beam Interactions with Materials and Atoms, v. 294, p. 203-207.

Molliex, S., Siame, L.L., Bourles, D.L., Bellier, O., Braucher, R. & Clauzon, G. (2013): Quaternary evolution of a large alluvial fan in a periglacial setting (Crau Plain, SE France) constrained by terrestrial cosmogenic nuclide (Be-10): Geomorphology, v. 195, p. 45-52.

Müller, A.M., Christl, M., Lachner, J., Synal, H.-A., Vockenhuber, C. & Zanella, C. (2015): 26Al measurements below 500kV in charge state 2+: Nuclear Instruments and Methods in Physics Research Section B: Beam Interactions with Materials and Atoms, v. 361, p. 257-262.

Nagra (2014): Etappe 2: Vorschlag weiter zu untersuchender geologischer Standortgebiete mit zugehörigen Standortarealen für die Oberflächenanlage: Geologische Grundlagen Dossier III Geologische Langzeitentwicklung.: Nagra Technischer Bericht NTB 14-02 Dossier III.

Nishiizumi, K. (2004): Preparation of 26Al AMS standards: Nuclear Instruments and Methods in Physics Research Section B: Beam Interactions with Materials and Atoms, v. 223-224, p. 388-392.

Nishiizumi, K., Imamura, M., Caffee, M.W., Southon, J.R., Finkel, R.C. & McAninch, J. (2007): Absolute calibration of Be-10 AMS standards: Nuclear Instruments & Methods in Physics Research Section B-Beam Interactions with Materials and Atoms, v. 258, no. 2, p. 403-413.

Nishiizumi, K., Lal, D., Klein, J., Middleton, R. & Arnold, J. (1986): Production of 10Be and 26Al by cosmic rays in terrestrial quartz in situ and implications for erosion rates: Nature, v. 319, no. 6049, p. 134.

Nishiizumi, K., Winterer, E.L., Kohl, C.P., Klein, J., Middleton, R., Lal, D. & Arnold, J.R. (1989): Cosmic-Ray Production-Rates of Be-10 and Al-26 in Quartz from Glacially Polished Rocks: Journal of Geophysical Research-Solid Earth and Planets, v. 94, no. B12, p. 17907-17915.

Norton, K.P., von Blanckenburg, F., Schlunegger, F., Schwab, M. & Kubik, P.W. (2008): Cosmogenic nuclide-based investigation of spatial erosion and hillslope channel coupling in the transient foreland of the Swiss Alps: Geomorphology, v. 95, no. 3-4, p. 474-486.

Penck, A. & Brückner, E. (1909): Die alpen im Eiszeitalter, CH Tauchnitz.

Phillips, F.M., Argento, D.C., Balco, G., Caffee, M.W., Clem, J., Dunai, T. J., Finkel, R., Goehring, B., Gosse, J.C. & Hudson, A.M. (2016): The CRONUS-Earth project: a synthesis: Quaternary Geochronology, v. 31, p. 119-154.

Portenga, E.W. & Bierman, P.R. (2011): Understanding earth's eroding surface with 10Be: GSA Today, v. 21, no. 8, p. 4-10.

Preusser, F. & Schlüchter, C. (2004): Dates from an important early Late Pleistocene ice advance in the Aare Valley, Switzerland: Eclogae Geologicae Helvetiae, v. 97, no. 2, p. 245-253.

Preusser, F., Reitner, J.M. & Schlüchter, C. (2010): Distribution, geometry, age and origin of overdeepened valleys and basins in the Alps and their foreland: Swiss Journal of Geosciences, v. 103, no. 3, p. 407-426.

Preusser, F., Rudolf Graf, H., Keller, O., Krayss, E. & Schlüchter, C. (2011): Quaternary glaciation history of Northern Switzerland: E&G Quaternary Sci. J., v. 60, no. 2/3, p. 282-305.

Puchol, N., Lave, J., Lupker, M., Blard, P. H., Gallo, F., France-Lanord, C. & Team, A. (2014): Grain-size dependent concentration of cosmogenic Be-10 and erosion dynamics in a landslide-dominated Himalayan watershed: Geomorphology, v. 224, p. 55-68.

Repka, J.L., Anderson, R.S. & Finkel, R.C. (1997): Cosmogenic dating of fluvial terraces, Fremont River, Utah: Earth and Planetary Science Letters, v. 152, no. 1-4, p. 59-73.

Rixhon, G., Bourles, D.L., Braucher, R., Siame, L., Cordy, J. M. & Demoulin, A. (2014): Be-10 dating of the Main Terrace level in the Ambleve valley (Ardennes, Belgium): new age constraint on the archaeological and palaeontological filling of the Belle-Roche palaeokarst: Boreas, v. 43, no. 2, p. 528-542.

Ruddiman, W.F., Raymo, M.E., Martinson, D.G., Clement, B.M. & Backman, J. (1989): Pleistocene evolution: Northern hemisphere ice sheets and North Atlantic Ocean: Paleoceanography, v. 4, no. 4, p. 353-412.

Ruszkiczay-Rüdiger, Z., Braucher, R., Novothny, Á., Csillag, G., Fodor, L., Molnár, G. & Madarász, B. (2016): Tectonic and climatic control on terrace formation: Coupling in situ produced 10Be depth profiles and luminescence approach, Danube River, Hungary, Central Europe: Quaternary Science Reviews, v. 131, p. 127-147.

Ruszkiczay-Rudiger, Z., Csillag, G., Fodor, L., Braucher, R., Novothny, A., Thamo-Bozso, E., Virag, A., Pazonyi, P., Timar, G. & Team, A. (2018): Integration of new and revised chronological data to constrain the terrace evolution of the Danube River (Gerecse Hills, Pannonian Basin): Quaternary Geochronology, v. 48, p. 148-170.

Schlüchter, C. (1989): A non-classical summary of the Quaternary stratigraphy in the Northern Alpine Foreland of Switzerland: Bulletin de la Société neuchâteloise de Géographie, v. 23, p. 143-157.

Schnellmann, M., Fischer, U., Heuberger, S. & Kober, F. (2014): Erosion und Landschaftsentwicklung Nordschweiz – Zusammenfassung der Grundlagen im Hinblick auf die Beurteilung der Langzeitstabilität eines geologischen Tiefenlagers (SGT Etappe 2). Nagra Arbeitsbericht NAB.

Sharma, P. & Middleton, R. (1989): Radiogenic production of 10Be and 26Al in uranium and thorium ores: Implications for studying terrestrial samples containing low levels of 10Be and 26Al: Geochimica et Cosmochimica Acta, v. 53, no. 3, p. 709-716.

Siame, L., Bellier, O., Braucher, R., Sebrier, M., Cushing, M., Bourles, D., Hamelin, B., Baroux, E., de Voogd, B., Raisbeck, G. & Yiou, F. (2004): Local erosion rates versus active tectonics: cosmic ray exposure modelling in Provence (south-east France): Earth and Planetary Science Letters, v. 220, no. 3-4, p. 345-364.

Stone, J.O. (2000): Air pressure and cosmogenic isotope production: Journal of Geophysical Research-Solid Earth, v. 105, no. B10, p. 23753-23759.

Viveen, W., Braucher, R., Bourlès, D., Schoorl, J. M., Veldkamp, A., van Balen, R.T., Wallinga, J., Fernandez-Mosquera, D., Vidal-Romani, J.R. & Sanjurjo-Sanchez, J. (2012): A 0.65Ma chronology and incision rate assessment of the NW Iberian Miño River terraces based on 10Be and luminescence dating: Global and Planetary Change, v. 94-95, p. 82-100.

von Blanckenburg, F., Belshaw, N.S. & O'Nions, R.K. (1996): Separation of Be-9 and cosmogenic Be-10 from environmental materials and SIMS isotope dilution analysis: Chemical Geology, v. 129, no. 1-2, p. 93-99.

Wittmann, H., von Blanckenburg, F., Kruesmann, T., Norton, K.P. & Kubik, P.W. (2007): Relation between rock uplift and denudation from cosmogenic nuclides in river sediment in the Central Alps of Switzerland: Journal of Geophysical Research-Earth Surface, v. 112, no. F4.

York, D. (1968): Least squares fitting of a straight line with correlated errors: Earth and Planetary Science Letters, v. 5, p. 320-324.

Zhao, Z., Granger, D., Zhang, M., Kong, X., Yang, S., Chen, Y. & Hu, E. (2016): A test of the isochron burial dating method on fluvial gravels within the Pulu volcanic sequence, West Kunlun Mountains, China: Quaternary Geochronology, v. 34, p. 75-80.

Zhao, Z., Granger, D.E., Chen, Y., Shu, Q., Liu, G., Zhang, M., Hu, X., Wu, Q., Hu, E., Li, Y., Yan, Y. & Qiao, L. (2017): Cosmogenic nuclide burial dating of an alluvial conglomerate sequence: An example from the Hexi Corridor, NE Tibetan Plateau: Quaternary Geochronology, v. 39, p. 68-78.

Appendix A: Systematic tests for quartz purification for cosmogenic nuclide analysis

A.1 Appropriate quartz purification procedure to achieve low ^{27}Al contents

In the following, two different cleaning procedures and the results of systematic comparisons are presented. Common quartz purification for classical exposure dating is performed using HCl treatment at the beginning to remove carbonates and oxides, followed by several (6 – 8) HF washing cycles until the sample is clean (method "A", Fig. A-1). However, there is the tendency for samples treated with this procedure to not achieve low ^{27}Al content, which is why Akçar et al. (2017) incorporated 1 – 2 applications of Hot Phosphoric Acid (HPA) and NaOH treatments (explained below, Fig. A-1). The advantage of this HPA treatment (outlined in Mifsud et al. 2013) is that the phosphoric acid only attacks feldspars and other Al-bearing mineral phases but not quartz. Therefore, the sample volume is not continuously reduced as with ongoing HF treatments where the partial dissolution of quartz is typical (Mifsud et al. 2013). The other method, method B (Fig. 1), is the original description from Mifsud et al. (2013). The authors suggest completely avoiding HF treatments from the beginning because the mineral grains are coated by fluoride ions that appear to make the grains inert for the later HPA treatments. Therefore, they prefer to use aqua regia instead ($HCl:HNO_3$ in a mixture ratio of 3:1) to dissolve carbonates and oxides. The HPA treatments are performed in glass flasks, and 100 % concentrated phosphoric acid is heated up to 240 – 250 °C in heating mantles. After conversion to pyrophosphoric acid and the digestion of the feldspars and other non-quartz mineral phases, a gel consisting of silicic aluminous hydroxides is formed. This gel is then washed out together with the dissolved minerals. The phosphoric acid remaining in the quartz is neutralised with hot NaOH, which reacts with any residual silicic aluminous materials.

At the end of the final HF cycles in method A and before the final HF cycles in method B, a sub-sample of 1 g quartz is analysed for its ^{27}Al-content using an inductively coupled plasma mass spectrometer (ICP-MS). This rather fast check for ^{27}Al represents a standard sample bracketing method (the so-called "Al Quick Test", Fig. A-2). As the ICP-MS measurements are a sequence of sample1-standard-blank-sample2-standard-blank, etc., only a measurement uncertainty of ~ 30 % can be given, which is sufficient for a first check of the ^{27}Al content. However, for later Al measurements of the aliquot, the more precise measurement technique of the standard-addition is used which yields a very low measurement uncertainty of 3 % (see Section 2.3.3, C. Maden, pers. comm.). The Al Quick Test takes a 1 g sub-sample out of the 80 or 100 g full sample, which could be not fully representative. Therefore, to dissolve 1 g in the beaker, repeated sub-samples are combined to increase representativity.

Systematic tests of the two parallel aliquots of six samples treated by both purification methods A and B show that none of the methods achieve consistently better results i.e. lower ^{27}Al contents (Fig. A-3). In two cases, samples treated by method B showed a two to three times higher content. Another set of nine samples treated by method A was repeatedly treated by two to three further HPA applications. In almost all of the samples, no further reduction was achieved, thus suggesting that the mineral grains might be coated by fluoride ions from previous HF treatments and therefore inert to the phosphoric acid (as suggested by Mifsud et al. 2013). Another likely explanation is that the aluminium is inside the quartz lattice and any further etching leads to a reduction of aluminium content.

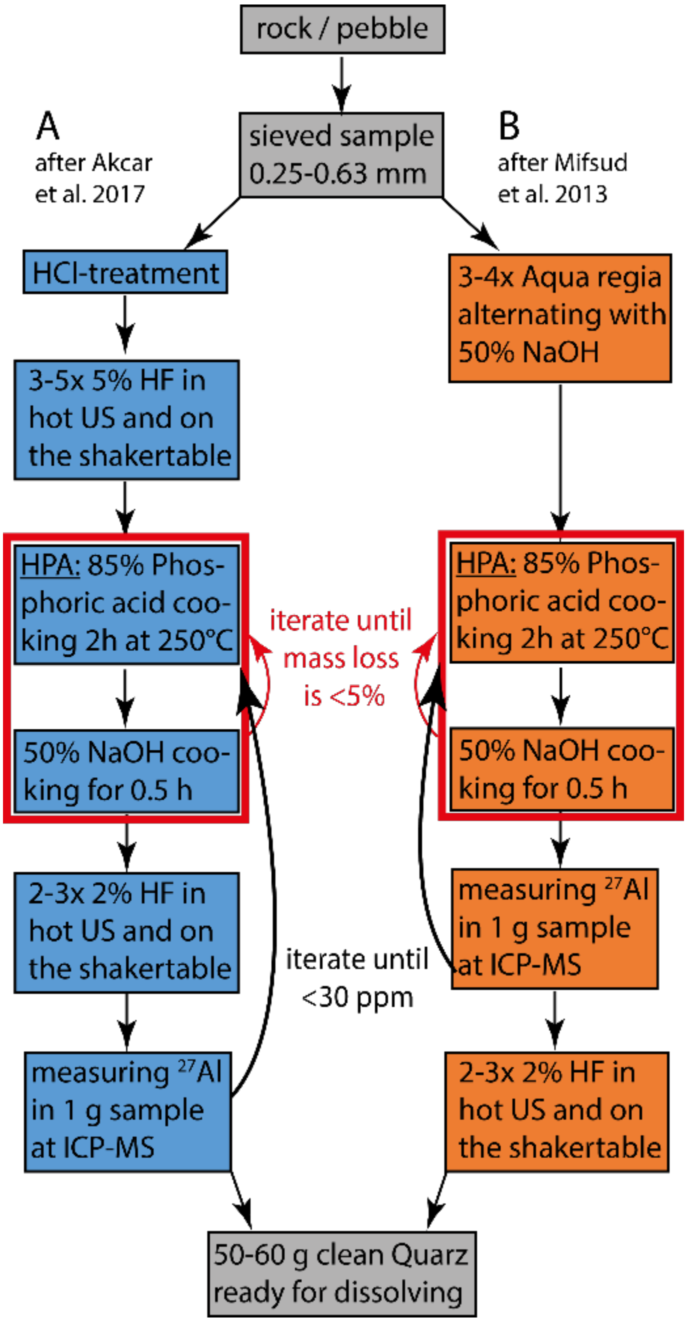

Fig. A-1: Illustration of two procedures for quartz purification aiming for a low ^{27}Al content in clean quartz

In contrast to the traditional method of only using HF, method A includes the application of Hot Phosphoric Acid (HPA) after several HF washing cycles. After such a cycle, 1 g of quartz is analysed, and iteration continues until ^{27}Al is lower than 30 ppm. Method B avoids the treatment with HF at the beginning and prefers to work with aqua regia and HPA thereafter. The sample cleaning iteration for a desired low ^{27}Al content of < 30 ppm takes place before the final few HF washing cycles.

US = ultrasonic

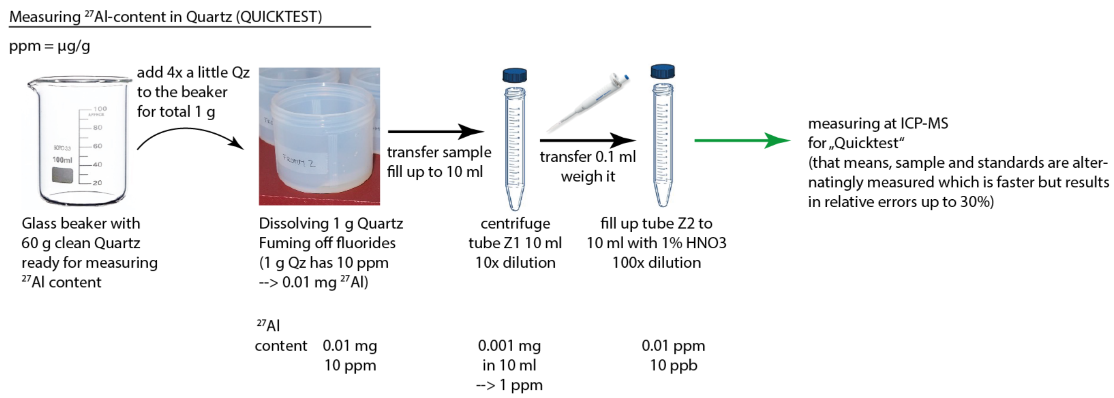

Fig. A-2: Illustration of the procedure for the "Al Quick Test", a fast estimate of the ^{27}Al content in clean quartz samples for later measurement by ICP-MS

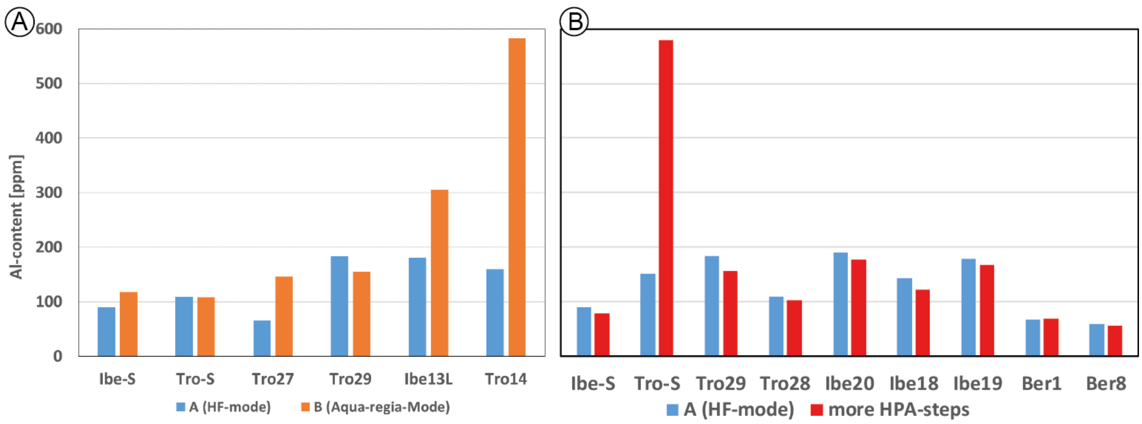

Fig. A-3: Systematic tests of the two parallel aliquots of six samples treated by both purification methods A and B and respective ^{27}Al contents

Quartz samples treated only by aqua regia and several HPA steps show a tendency to only a weak efficiency in terms of ^{27}Al reduction as indicated by several samples with very high ^{27}Al contents (Fig. A-4). The ^{27}Al contents, however, significantly drop when several HF treatments were applied (red bars in Fig. A-5). Comparisons of the ^{27}Al content of samples treated only by HF (before the ICP test in December 2017) and by 2 to 5 HPA steps (before the ICP test in April 2018) and again following HF applications (before the ICP test in June 2018) produce similar results (see the lower half of Fig. A-5). Therefore, whether a sample is treated either by method A, B or a combination of both does not have a significant effect on the final ^{27}Al content. Apparently, the ^{27}Al content reaches a plateau and does not drop below it (R. Braucher pers. comm, AMS14 proceedings Ottawa).

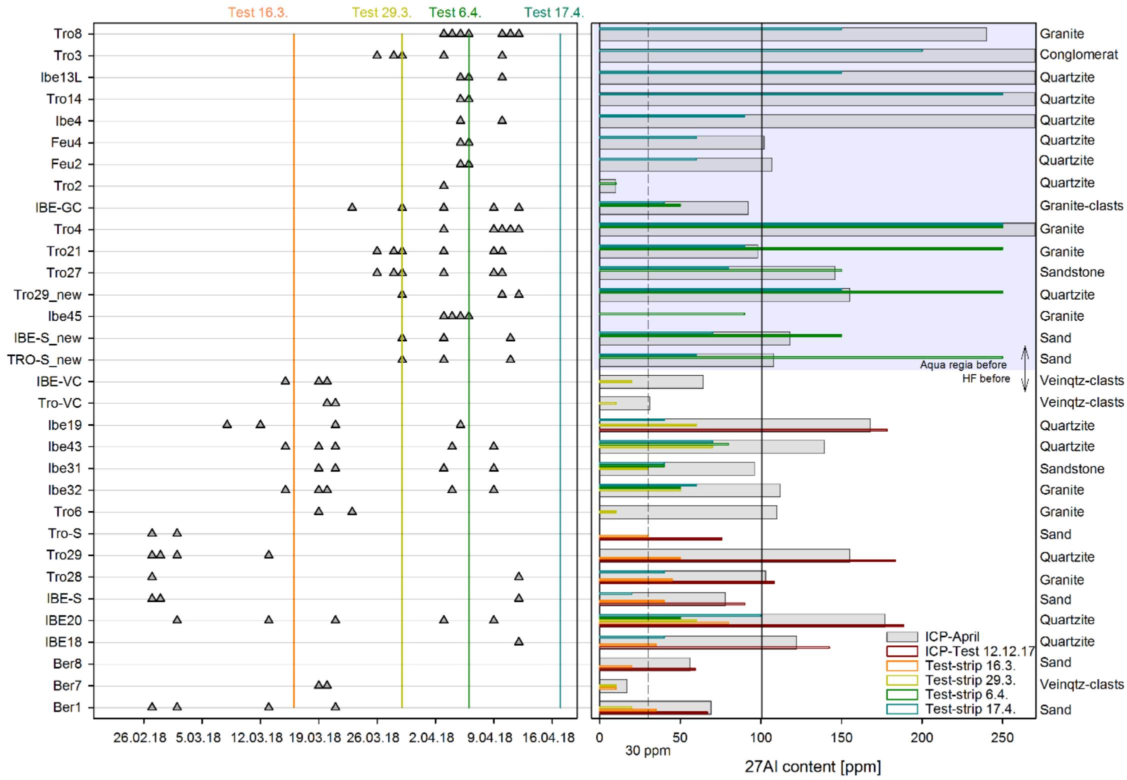

Fig. A-4: Table of samples processed over several months throughout 2017 and 2018 with the ^{27}Al content verified using the Quick Test procedure of the ICP-MS

The left table indicates when HPA treatments (triangles) were performed, and the right table indicates the corresponding measurements from ICP-MS (Al Quick Tests) supplemented by the sample-specific lithology. Samples with the suffix "_new" were prepared with a new separate aliquot from the raw sample. Note, the samples plotted in the upper/lower half of the table were prepared by method B/A, respectively. Once the HPA treatments were completed, all samples were tested for their ^{27}Al content (end of April 2018). Between the ICP measurements of the same sample in April and June 2018, several HF treatments were applied to the sample. Sampling names with the prefix Ibe, Tro, Feu and Ber refer to samples taken at the outcrops Iberig, Tromsberg, Feusi and Beringen (see Chapter 3 for sampling sites).

As shown above, the quartz purification method does not seem to be crucial for obtaining a sufficiently low ^{27}Al content. The results of 55 processed samples for the three key lithologies vein quartz, quartzite and granite measured for their ^{27}Al content in six Quick Test campaigns for ICP-MS allow a simple statistic to be developed demonstrating the relative abundancy of low ^{27}Al contents (Fig. A-5). The statistic considers only these key lithologies as they represent lithologies which are both abundant in the Alpine Deckenschotter units and contain enough quartz for processing in the laboratory. Samples from other lithologies such as sand, sandstone, conglomerates and gneisses were also treated but did not successfully result in achieving a low ^{27}Al content. Apparently, the most successful lithology is vein quartz, where pebbles or amalgamated casts consisting of vein quartz yield quite a high success chance of 67 % to reach a low ^{27}Al content (< 30 ppm). The rate is much worse for quartzite (19 %) and granites (11 %). The high success rate for vein quartz is not surprising as vein quartz found in outcrop usually appears quite clean, consisting of 99.9 % pure quartz without any aluminium-silicate phases such as feldspars. The low hit rate for quartzite can be reasonably explained by the classification scheme for quartzite which takes into account quite a wide and genetically diverse range of clast lithologies. A quartzite found in outcrop can originate from a meta-sandstone/-breccia/ conglomerate (recrystallised as a result of Alpine metamorphosis), quartz-rich meta-pelites (with little mica incorporated), radiolarites and massive meta-granites (without a texture). Quartzites appear to have ~ 98 % quartz but can contain feldspars, micas, amphiboles and other rare minerals. Particularly quartzites from meta-sandstones with a former grain size of fine-sand or silt may contain impurities between the former grains. Fragmentation in the SelFrag then creates a new, larger pseudo grain size of 250 to 600 µm and thus the impurities remain within the former grain framework. Finally, granites have the lowest chance of obtaining a pure quartz with a ^{27}Al content of less than 30 ppm, possibly because of their lower quartz content. Typical quartz contents are within 20 – 60 % and therefore a lot of feldspars and micas have to be removed before a clean quartz remains. Nonetheless, repeated cleaning does not lower the ^{27}Al content of quartz in a granite sample.

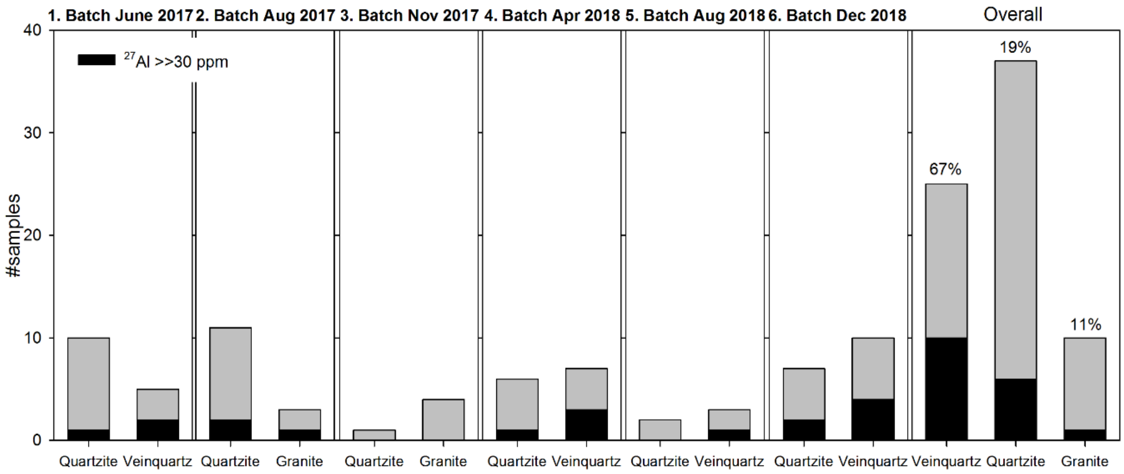

Fig. A-5: Overview of all six Quick Test campaigns of the ICP-MS for the three main lithologies quartzite, vein quartz and granite indicating the number of samples yielding less than ~ 30 ppm ^{27}Al content

Note, in some of the test batches there were e.g. granites incorporated that did not yield a low ^{27}Al content but did count for the overall rating (figure on far right). The overall rating clearly shows that the vein quartz lithology yields by far the most samples with a low ^{27}Al content. Proportionally much fewer samples with a sufficiently low ^{27}Al content are found for quartzite and granite lithologies.

Obviously, the lithology itself dictates the ^{27}Al content. However, focusing only on the vein quartz lithology would reduce the workload for the cycle cleaning-testing-rejecting, but is also not straightforward for several reasons: First, the vein quartz samples commonly have quite low nuclide concentrations (see also Akçar et al. 2017) and thus do not contribute to a large spread in the isochron plot which is required for a meaningful data regression. Second, samples consisting of only one lithology might bring the risk of a certain but unknown lithology-dependent bias to the dataset.

Whereas the lithology has a strong impact on low ^{27}Al content, the effect of the grain size on quartz purification is unclear. As outlined in the last section, sieving a fragmented pebble to a grain size bigger than the natural grain size found in the sedimentary or crystalline texture can create a problem. A short assessment deals with the assumed effect of grain size and measured ^{27}Al contents (Fig. A-6). Six samples were sieved into two grain-size fractions of 250 – 400 µm (as performed by Akçar et al. 2017) and 250 – 810 µm (Grischott et al. 2016, 2017) and cleaned with method A (HF treatments only). None of the samples yielded an ^{27}Al content lower than 60 ppm. Therefore, the samples for this study were sieved to a compromise grain size of 250 – 610 µm in order to get the most out of the limited volume from a fragmented sample such as a small clast. Again, the sample lithology is much more decisive than the purification method or the chosen grain-size fraction. Ultimately, the sample itself controls the ^{27}Al content.

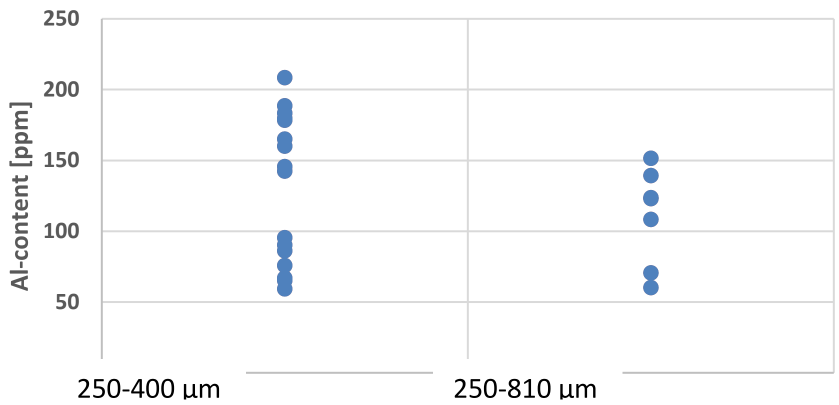

Fig. A-6: Comparison of the ^{27}Al contents of aliquots from six samples sieved to the two different grain size fractions of 250 – 400 µm and 250 – 810 µm

For the lower grain-size fraction, the results of a few more samples were added showing that even higher ^{27}Al contents are possible. However, this simple comparison also justifies the main finding that the ^{27}Al content is lithology-driven and, to an even greater degree, sample-specific. Therefore, the effects of grain size are suggested to be minimal.

A.2 Attempt to visually inspect samples for their ^{27}Al content

Measuring the ^{27}Al content in quartz was established by the Al Quick Test for ICP-MS. This procedure is quite time-consuming as 1 g of quartz of the dry sample has to be dissolved (full-day workload), remaining fluorides fumed (another full-day workload) and the sample has to be prepared for the ICP-MS measurements by establishing the appropriate dilution series (another full-day workload). In total, 3 – 4 days of work for 1 – 2 batches of samples (9 – 18 samples) are required. Accordingly, if visual inspection could help to identify aluminium-bearing mineral phases such as feldspars or micas in the sample and also to estimate the ^{27}Al content, then a lot of laboratory time could be saved.

For each sampling site, a sample was selected for a visual check under the microscope (Fig. A-7): Ber11 (quartzite, 9 ppm), Tro27 (sandstone, 90 ppm) and Ibe1 (quartzite, 85 ppm). Potential contaminants containing a sufficient amount of ^{27}Al included feldspar grains and aggregated quartz grains (such as those from the sandstone Tro27). The photograph of the Ber11 sample shows that only a few grains can be clearly identified as pure, greyish and transparent quartz grains. All other grains are not transparent and may have been bleached as a result of the intense HF leaching process. Based only on the photograph, it is difficult to estimate a ^{27}Al content as low as 9 ppm as measured for Ber11. In the Tro27 sample, a few grains could be feldspars as they have the typical milky-white appearance, and in one case even the cleavage is visible. Feldspar grains etched by HF form some finger-like ramifications as observed in Tro27. Aggregated sand grains could be affected by aluminium-rich contaminations and thus contribute to the rather high ^{27}Al content of 90 ppm in the Tro27 sample. For the Ibe1 quartzite sample, the rather high content of 85 ppm seems to be reasonable but remains very difficult to estimate.

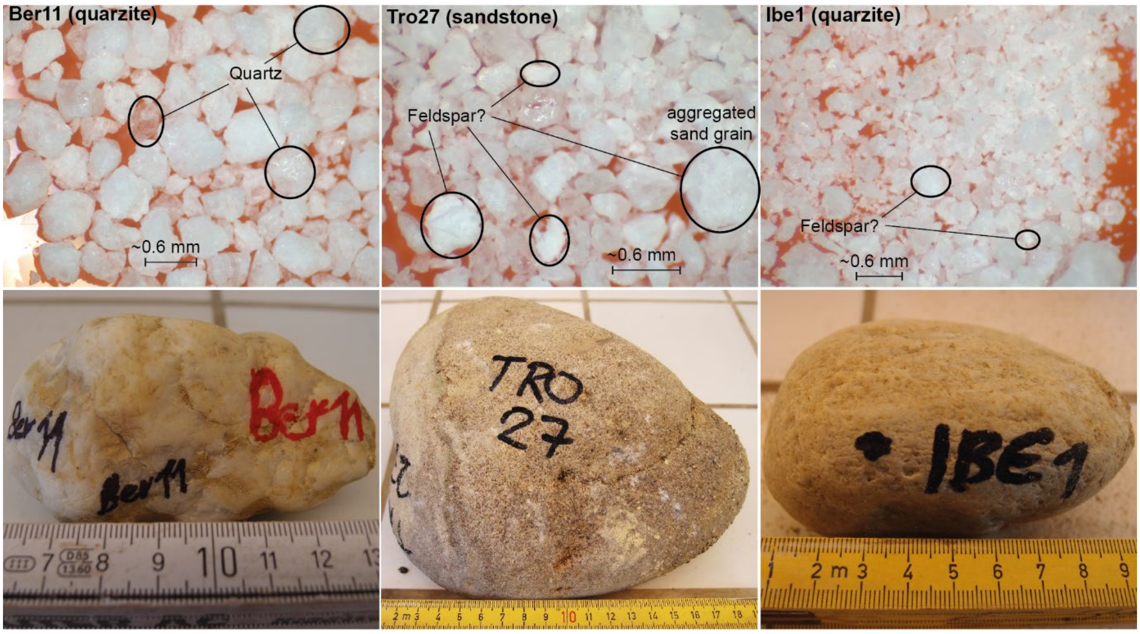

Fig. A-7: Visual check under the microscope for aluminium-bearing grains such as feldspars and aggregated sand grains

The ^{27}Al contents for Ber11, Tro27 and Ibe1 are 9, 90 and 85 ppm, respectively.

The visual check by microscope in a small sample aliquot stimulated simple calculations of how many contaminated grains containing aluminium can be expected for a typical ^{27}Al content in a sample (Tab. A-1). For this purpose, the amount of grains in a typical 1 g sample size – as used in the Quick Test – is calculated first. Assuming different mean grain sizes of 0.5, 0.4 and 0.3 mm, it is possible to determine the subsequent volumes and weights of a single grain. A typical sample was assumed to consist of 20 % of grains with a 0.5 mm size and 40 %, respectively, with a 0.4 and 0.3 mm grainsize. Empirical evidence from quartz purification (mechanical and chemical destruction of grains) led to the assumption that the lower grain-size fractions of 0.3 and 0.4 mm are significantly more abundant than the larger grain size fraction of 0.5 mm. 1 g of a sample could have roughly 16'000 grains with a scatter of assumed ± 2'000 grains (equal to 12.5 %). Different contamination scenarios or ^{27}Al contents of the samples of 300, 150 and 30 ppm are assumed. If the aluminium is assumed to be caused by the existence of feldspar grains, a volumetric content of 20 % was assumed to be pure aluminium. The division of the total Al content in a 1 g sample (0.3, 0.15 and 0.03 mg Al) by the specific weight of a single grain (0.5, 0.4 and 0.3 mm in diameter) yields the total number of feldspar grains. The number of grains considered to be feldspar is highest for the 300 ppm scenario. Between 10 and 30 grains can be expected if the grain sizes are between 0.3 and 0.5 mm. For the lowest contamination scenario of 30 ppm, only very few grains containing aluminium, i.e. just 1 – 4, can be expected. By comparison, for the Tro14 sample bearing 583 ppm ^{27}Al, the second-highest ^{27}Al content measured in the dataset for this project, ~ 80 grains of the smallest and 17 of the largest grain size can be expected. These low contamination numbers could lead to the expectation that these grains could be handpicked and manually removed from the sample. However, these numbers are estimated for a 1 g sample. Usually, 60 – 70 g of sample is required and since it is not fully clear how to sort out the contaminating grains and how to distinguish them from the equally bleached mass of quartz grains, hand-picking is not a promising alternative.

Tab. A-1: Table for a simple and fast estimate of the number of grains in a 1 g sample depending on the grain size classes 0.5, 0.4 and 0.3 mm in a sample previously treated with HF (resulting in reduced grain-size classes due to leaching)

Depending on the contamination scenarios of 300, 150 and 30 ppm, the total number of contaminated grains are calculated, assuming the contaminated grains occur in a single grain size fraction.

Estimate #grains for specific diameters

mean size of a grain	0.5	mm	0.4	mm	0.3	mm		
Radius	0.25	mm	0.2	mm	0.15	mm		
Volume	0.065	mm3	0.034	mm3	0.014	mm3		
	0.000	cm3	0.000	cm3	0.000	cm3		
Density	2.650	g/cm3	2.650	g/cm3	2.650	g/cm3		
Weight	0.00017	g	0.00009	g	0.00004	g		
	0.173	mg	0.090	mg	0.037	mg		
1 g sample	1	g	1	g	1	g		
total grains	5'766	grains	11'099	grains	26'693	grains		
Assumed abundancy	20 %		40%		40 %			
#grains	1'153		4'400		10'677			
#grains in 1 g sample	**16'270**	**grains**	**±2000**				Sample Tro14	
Contamination scenarios	300	ppm	150	ppm	30	ppm	583	ppm
Al-content in 1 g sample	0.3	mg Al	0.15	mg Al	0.03	mg Al	0.583	
Al-content in a Fsp-grain	20 %		20%		20 %		20 %	
#grains if only 0.5 mm Ø	9		4		1		17	
#grains if only 0.4 mm Ø	17		8		2		32	
#grains if only 0.3 mm Ø	40		20		4		78	

Al = Aluminium, Fsp = Feldspar

A.3 Recommendations for a reasonable quartz purification process

The systematic tests for two different quartz purification methods and the statistics on achieving low ^{27}Al contents (< 30 ppm) in sample numbers suggest that the lithology has a strong impact on the ^{27}Al level that can be reached. Even for samples within the same lithology class, the samples themselves show a significant scatter within the measured ^{27}Al range. Therefore, it seems possible to predict the ^{27}Al content for a specific sample with sufficient reliability. In other words, the user is obliged to purify quartz and determine the Al content by conducting the Quick Test for ICP-MS. There is no time-saving shortcut. This fragmentation process for a batch of 8 – 9 samples until conducting the Quick Test requires several weeks.

As a method of choice for treating the fragmented raw samples, method A is preferred as HF is quite efficient in removing non-quartz mineral phases and, despite its hazardous potential, less difficult to use as no hood is needed against gas formation. In detail, at least six treatments with 5 % (partially also 10 %) HF are applied to the carbonate-free sample (previously removed with HCl). Then, two steps with Hot Phosphoric Acid (HPA) alternating with sodium hydroxide (NaOH) are applied (following the procedure described by Mifsud et al. 2013). Before drying the samples, again two (mostly) weak HF treatments are performed. Commonly, the sample bottles filled with HF are in a heated ultrasonic bath during the day and on the shaking table overnight.

Once the samples have been tested for the ^{27}Al content with the Quick Test and the values are above 100 pm ^{27}Al, the sample should not be treated again. Experience with the enormous number of samples processed and measured for ^{27}Al content (> 80 in total) indicates that only one single sample, the Feu2 sample, showed a lower ^{27}Al content (drop from 102 to 16 ppm after several further HF treatments). Therefore, repeated sample treatments are inefficient and thus not recommended (reaching the plateau).

Obtaining samples with a sufficiently low ^{27}Al content of ~ 30 ppm is a labour-intensive and time-consuming challenge. The overview figure (Fig. A-4, see above) indicates that only a low proportion of the samples reach this goal. More samples, however, achieve ^{27}Al contents between 70 and 100 ppm. Therefore, samples which visually appear clean and full of pure quartz and have an ^{27}Al content below 100 ppm can also be used for further processing.

Similarly, samples with a ^{27}Al content above 30 ppm can yield acceptable results (low 1σ uncertainties of < 8 %) if the ^{26}Al in the sample is higher too. For example, for the Feu2 sample (^{27}Al content of 103 ppm), rather high ^{10}Be concentrations of 25'000 at/g and ^{26}Al concentrations of 100'000 at/g were measured. If the ^{26}Al concentrations are high, i.e. usually a $^{26/27}Al$ AMS ratio of 10^{-13} could be feasible. However, the user does not know this until the measurements are completed, and therefore selecting samples with a higher ^{27}Al content always bears a certain risk for higher uncertainties when the ^{26}Al concentrations are very low.

Not only should samples with a too high ^{27}Al content be avoided but also the opposite case of samples with a too low ^{27}Al content should be taken into account. Samples with ^{27}Al contents below ~ 10 ppm might not provide enough particle currents at the AMS. The particle currents are established by the ^{27}Al atoms sputtered by the Cs source of the AMS at ETHZ. For a sample with 60 g of dissolved quartz and a ^{27}Al content of 10 ppm, the total sample after ion-exchange chromatography only contains 0.6 mg Al, which is at the lower limit for stable currents in AMS facilities (e.g. TANDY). A minimum of 1 mg Al is required to achieve good currents, although the latter also depends on the mixing ratio of the AlO and niobium. Larger sample amounts (e.g. 70 instead of 60 g of dissolved quartz) do not yield absolutely higher currents, but rather currents over a longer measuring period. With a longer measuring period, it is possible to extend the time to count ^{26}Al hits in the AMS detector. Exactly this relationship of large samples providing stable currents for a longer time period might be the key to good measurement results. Indeed, ^{26}Al

measurements on each single sample were performed for almost 4 hours, which is much longer than the conventionally performed measurement time for ^{26}Al concentrations 10 to 100 times higher (e.g. Hippe et al. 2012). Long measurement times also provide ideal conditions for increasing the time during which ^{26}Al counts can be accumulated. The measurement uncertainty provided by the AMS for each sample is strongly dependent on the absolute number of counts (relative error = 1/square root (total counts). However, the downside of long measurement times is that the background correction for the AMS measurement goes up, leading to potentially higher measurement errors.

Appendix B: Assessment of the outcrop potential for isochron burial dating

The following Figure B-1 displays the chosen decision tree giving points for the existence of a certain criterion based on geomorphology and profile characteristics. Tab. B-1 lists the assigned points considering the assessed criterion which, in sum, finally yield the total point number. The total point number is interpreted in terms of a simple classification into outcrops with high or low dating potential.

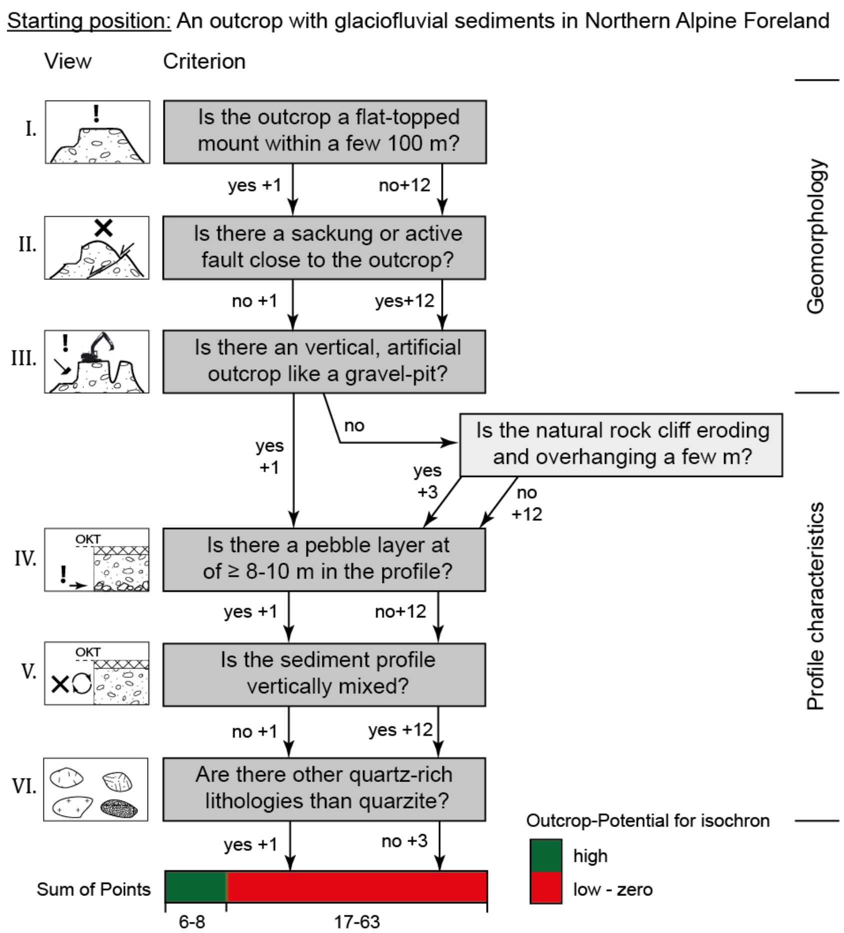

Fig. B-1: Decision tree based on six criteria

i) geometry and topography of the outcrop, ii) active displacements or movements around the outcrop, iii) recently opened, artificial outcrop, iv) existence of pebbles in the sediment, v) post-diagenetic changes in the profile, vi) availability of quartz. The specific values for each criterion were selected to be either 1 or 12 to obtain a clear distinction in the final sum. The lower the sum, the better the outcrop potential.

Tab. B-1: Assessment table for sites belonging to the Tiefere and Höhere Deckenschotter (upper and lower half of the table)

The sites are in the order of Nagra's three siting regions: Jura Ost (blue), Nördlich Lägern (green) and Zürich Nordost (purple).

			#criterion	I	II	III	IV	V	VI	Potential categories				
			Point range	1, 12	1, 12	1, 3, 12	1, 12	1, 12	1, 3			neotectonics		
Unit	Name	Locality	characteristicum Coordinates	*flat hilltop*	*neotectonic*	*artifical outcrop*	*pebbles*	*vertical mixing*	*Qz lithologies*	Sum	Classified	neglectable		methodological speciality
HDS	KG Tromsberg	Dürn-Gländ	663'749 261'512	1	1	1	1	1	1	6	High	6	High	grainsize (sand-pebble)
HDS	KG Stutz-Usserberg	Dürn-Gländ	664'180 264'066	1	12	1	1	1	1	17	Low	6	High	grainsize (sand-pebble)
HDS	KG Hüsliberg	Dürn-Gländ	665'697 262'730	1	12	1	1	1	1	17	Low	6	High	grainsize (sand-pebble)
HDS	Chüebodentobel	Lengnau	668'809 265'932	1	12	1	1	1	1	17	Low	6	High	
HDS	KG Schüliberg	Schneisingen	670'701 264'916	1	12	1	1	1	1	17	Low	6	High	
HDS	KG Feusi	Oberweningen	672'951 262'502	1	12	1	1	1	1	17	Low	6	High	grainsize (sand-pebble)
HDS	KG Waldhausen	Fisibach	672'460 265'750	1	12	1	1	1	1	17	Low	17	Low	slumped outcrop
HDS	Sünikon	Steinmaur	674'190 262'980	1	12	1	1	1	1	17	Low	6	High	badly exposed
TDS	KG Iberig	Würenlingen	661'188 263'896	1	12	1	1	1	1	17	Low	6	High	true burial, rock wall >40 m
TDS	KG Mülibuck	Würenlingen	661'999 264'131	1	12	1	12	1	1	28	Low	28	Low	slumped outcrop
TDS	Bruggerberg	Brugg	658'652 260'785	1	1	3	1	1	1	8	High	8	High	true burial, rock wall >40 m
TDS	KG Chirchhölzli	Uhwiesen	690'286 280'862	1	1	1	1	1	3	8	High	8	High	grain size fractions
TDS	KG Vorder Hörnli	Benken	691'650 280'000	1	12	1	1	1	3	19	Low	8	High	isochron burial
TDS	KG Kratzern	Trüllikon	693'190 279'298	1	12	1	1	1	3	19	Low	8	High	grain size fractions
TDS?	Buechbüel_North	Neuhausen	687'115 282'470	1	12	1	12	1	1	28	Low	28	Low	badly exposed
TDS?	Buechbüel_South	Neuhausen	687'055 282'280	1	12	1	1	1	1	17	Low	17	Low	outcrop too small, slumped
TDS	KG Oberbelche-West	Fisibach	672'060 267'865	1	12	1	12	1	1	28	Low	17	Low	outcrop is too low in height
TDS	KG Oberbelche-East	Fisibach	672'060 267'865	1	12	1	1	1	1	17	Low	6	High	isochron burial
TDS	KG Ischlag	Fisibach	672'550 267'535	1	12	1	1	1	1	17	Low	6	High	isochron burial
TDS	KG Schwändihalden	Weiach	674'060 267'255	1	1	1	1	1	1	6	High	6	High	isochron burial
TDS	Ämperg	Weiach	676'100 267'905	1	12	1	1	1	1	17	Low	17	Low	slumped outcrop

Appendix C: Pilot study availability of quartz samples at the Cholfirst site (TDS)

The Cholfirst site is located south of Schaffhausen in the Laufen-Uhwiesen village. It was identified as Tiefere Deckenschotter – TDS (Graf 2009 and references therein). Its situation is of high importance regarding the location of a potential deep geological repository, especially in the Zürich Nordost siting region. The investigated outcrop is located at around 540 m a.s.l. on a south-facing slope.

Two field reconnaissance campaigns of the Cholfirst site were performed in 2018. An estimation of possible sampling locations within the outcrop carried out on 03.05.2018 showed that it would be very difficult to find quartz clasts within the potential clast horizon (Fig. C-1A-B). On 21.08.2018, three persons using climbing equipment were involved in an examination of the upper parts of the outcrop (Fig. C-1C). This was no more successful than the first campaign with regard to the number of quartz-rich clasts found due to the predominance of East Alpine material consisting mainly of carbonates.

After approximately 2.5 hours, only a few small quartzites and 1 – 2 Verrucano clasts had been found. This sampling result is very poor compared to other sampling sites. Alternatively, a western part of the outcrop was checked using ropes but also there, barely 5 % of quartz clasts were found. Similar results were obtained while investigating a fallen block at the bottom of the outcrop (Fig. C-1B). Clasts in general are covered with patina, which mimics quartz-rich content. Moreover, the sediments are strongly cemented; therefore, extracting samples would have to involve heavier equipment than just hand-held hammers. From a technical perspective, sampling would also have to include the use of ropes and climbing gear as well as some pneumatic hammers or even a mini-excavator. Another aspect of this site is its legal status, as it is currently protected under nature reserve status (Naturschutzgebiet Chirchhölzli), which makes it even more complicated to organise an extensive sampling campaign.

All these facts suggest that certain difficulties exceed possible benefits. Even though the location of the site is favourable, the geological quality of the sediment as well as the problematic accessibility prevail, leading to the conclusion that the Cholfirst outcrop is not recommended for further sampling investigations.

Fig. C-1: Photo documentation of the Cholfirst outcrop, Chirchhölzli

A) shows the middle wall with a B) block now at the bottom of the outcrop. C) shows the western part checked for suitable layers.

Appendix D: Documentation of all samples with final ^{26}Al-^{10}Be results

Stratigraphic unit	Sampling site	Name	Size [cm]	Lithology
HT	Beringen	Ber1	Bag of sand	Sand sample
HT	Beringen	Ber4	10 × 13 × 7	Granite
HT	Beringen	Ber6	6 × 6 × 7	Quartzite
HT	Beringen	Ber7	Bag of clasts	Vein quartz clasts amalgamated
HT	Beringen	Ber11	9 × 5 × 7	Quartzite
HT	Beringen	Ber17	Bag of clasts	Vein quartz clasts amalgamated
HT	Beringen	Ber35	16 × 12 × 11	Gneiss (large crystals quartz rich)
HT	Beringen	Ber36	13 × 9 × 7	Vein quartz (large crystals)
HDS	Feusi	Feu2	8 × 7 × 7	Quartzite
HDS	Feusi	Feu4	12 × 6 × 8	Quartzite
HDS	Feusi	Feu16	11 × 9 × 10	Granite
HDS	Feusi	Feu21	8 × 5 × 5	Quartzite
HDS	Feusi	Feu26	21 × 16 × 9	Quartzite
HDS	Feusi	Feu37	13 × 8 × 3	Vein quartz (pegmatitic)
HDS	Feusi	Feu-VC	Bag of clasts	Vein quartz clasts amalgamated
HT	Glatt Valley	Gla1	Bag of sand	Sand sample (drill core)
HT	Glatt Valley	Gla3	Bag of sand	Sand sample (drill core)
TDS	Iberig	IBE1	8 × 6 × 5	Quartzite
TDS	Iberig	IBE3	8 × 6 × 6	Granite
TDS	Iberig	IBE22	7 × 8 × 7	Quartzite
TDS	Iberig	IBE23	10 × 8 × 6	Quartzite
TDS	Iberig	IBE 53	9 × 9 × 6	Quartzite
TDS	Iberig	Ibe-GC	Bag of clasts	Granite clasts amalgamated
TDS	Iberig	Ibe-S	Bag of sand	Sand sample
TDS	Iberig	Ibe-VC	Bag of clasts	Vein quartz clasts amalgamated
TDS	Iberig	Ibe-VC2	Bag of clasts	Vein quartz clasts amalgamated
HDS	Tromsberg	Tro2	16 × 13 × 10	Quartzite
HDS	Tromsberg	Tro8	15 × 11 × 7	Granite
HDS	Tromsberg	Tro16	17 × 11 × 8	Quartzite
HDS	Tromsberg	Tro20	22 × 18 × 9	Granite
HDS	Tromsberg	Tro25	7 × 7 × 5	Vein quartz
HDS	Tromsberg	Tro27	21 × 7 × 15	Sandstone
HDS	Tromsberg	Tro33	14 × 14 × 9	Granite (Aarmassiv)

Stratigraphic unit	Sampling site	Name	Size [cm]	Lithology
HDS	Tromsberg	Tro40	13 × 8 × 8	Quartzite (conglomeratic)
HDS	Tromsberg	Tro45	15 × 12 × 6	Quartzite (brecc. pegm.)
HDS	Tromsberg	Tro-S	Bag of sand	Sand sample
HDS	Tromsberg	TRO-VC	4 × 4 × 4	Vein quartz amalgamate
HDS	Tromsberg	TRO-VC2	5 × 4 × 4	Vein quartz amalgamate

^{26}Al AMS measurement details

The following constant background rates were subtracted:

For batch no. 1: 0.003 cts/s, no. 2: 0.001 cts/s, no. 3: 0.002 cts/s and no. 4: 0.005 cts/s

Note that several samples were measured as two separate targets (e.g. Feu2_1 and Feu2_2). Both measurements were calculated to a final result later.

Batch no.	Name	Counts ^{26}Al	Runtime [s]	Fraction of background correction	Corrected ^{26}Al counts
1	BER11	96	8'854	28 %	69
1	IBE22	264	7'244	8 %	242
1	Ber4	160	14'757	28 %	116
1	IBE3	995	15'562	5 %	948
1	IBE23	209	15'562	22 %	162
1	IBE1	83	15'562	56 %	36
1	TRO16	111	15'293	41 %	65
1	TRO25	224	14'690	20 %	180
1	TRO-VC	288	15'294	16 %	242
1	BER6	169	14'489	26 %	126
1	IBE-VC	141	14'489	31 %	98
2	BER7	173	4'836	3 %	168
2	Feu2_1	133	13'432	10 %	120
2	Feu2_2	88	13'074	15 %	75
2	Ibe-VC2_1	42	12'716	30 %	29
2	Ibe-VC2_2	36	12'715	35 %	23
2	Tro-VC2	160	12'715	8 %	147
2	Tro2	112	4'477	4 %	108
2	Ibe-S_1	34	12'357	36 %	22
2	Ibe-S_2	46	12'717	28 %	33

Batch no.	**Name**	**Counts ^{26}Al**	**Runtime** [s]	**Fraction of background correction**	**Corrected ^{26}Al counts**
2	Ber1_1	36	12'716	35 %	23
2	Ber1_2	51	13'074	26 %	38
2	Tro8_1	44	12'716	29 %	31
2	Tro8_2	29	12'716	44 %	16
3	Gla3	111	21'815	39 %	67
3	Ibe-GC	185	22'084	24 %	141
3	Tro-S	162	21'905	27 %	118
3	Tro20	271	21'906	16 %	227
3	Tro33	716	8'494	2 %	699
3	Tro45	286	21'905	15 %	242
3	Feu4	5'132	7'332	0.3 %	5'117
3	Gla3_2	71	15'736	44 %	40
3	Ibe-GC_2	168	22'185	26 %	124
3	Tro20_2	292	22'352	15 %	247
3	Tro45_2	293	22'352	15 %	248
3	Tro-S_2	126	18'061	29 %	90
4	Ber 17	440	8325	9 %	398
4	Ber 35	212	8327	20 %	170
4	Ber 36	220	8594	20 %	177
4	IBE 53	82	8326	51 %	40
4	IBE 55	55	8057	73 %	15
4	Feu 16	269	8594	16 %	226
4	Feu 21	268	8594	16 %	225
4	Feu 26	266	8326	16 %	224
4	Feu 37	2'322	8325	2 %	2280
4	Feu VC	617	8328	7 %	575
4	GLA 1	65	8057	62 %	25
4	TRO 16	84	8057	48 %	44
4	TRO 25	141	8057	29 %	101
4	TRO 27	65	7251	56 %	29
4	TRO 40	65	7253	56 %	29

Photo documentation – Beringen

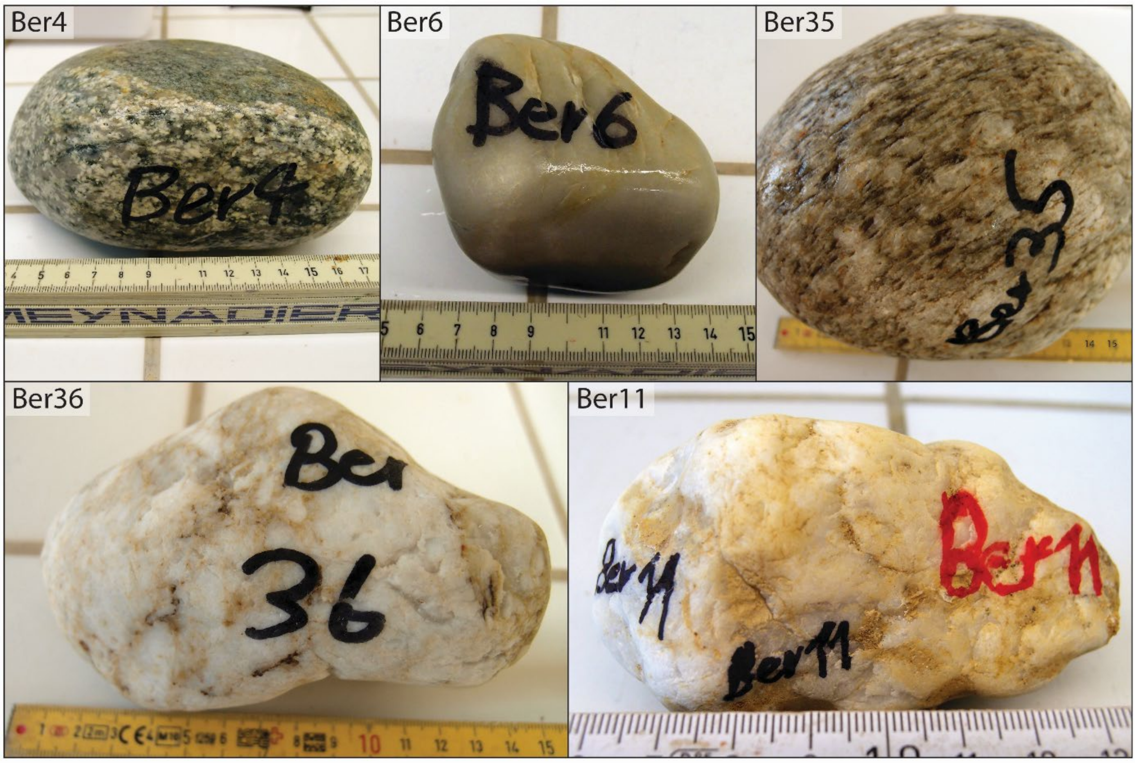

Photo documentation – Feusi

Photo documentation – Glatt Valley

Photo documentation – Iberig

Photo documentation – Tromsberg

Appendix E: Non-cosmogenic ^{26}Al produced in quartz – a pilot study

^{10}Be and ^{26}Al are produced in-situ by spallation in rocks exposed to cosmic rays. Production of ^{10}Be and ^{26}AI in the lithosphere by natural radiogenic nuclear reactions has usually been regarded to be negligible and has not been considered in most studies. However, Sharma & Middleton (1989) show experimentally that these two isotopes can also be produced by radiation from uranium and thorium decay-chain radionuclides contained within the host rock. In the following, the knowledge and quantitative data presented are based on Sharma and Middleton (1989). All the rock samples used for their study contained uranium and thorium and their daughter nuclides in radioactive equilibrium. The U-Th series radionuclides can produce ^{10}Be and ^{26}Al by three different direct nuclear processes: (a) exotic decay, (b) fission and (c) alpha-induced nuclear reactions. Only process c) will be considered further. It is the most important one because nearly all geological samples contain a few ppm of U-Th and 0.5 to 3 % of the target element sodium (Sharma and Middleton, 1989). In rocks, ^{10}Be and ^{26}Al can be produced by the secondary reactions ^{7}Li(α,p) ^{10}Be and ^{23}Na(α,n) ^{26}Al, respectively. In other words, ^{10}Be can be produced from ^{7}Li being hit by an alpha particle (release of a proton) and ^{26}Al is produced from ^{23}Na being hit by an alpha particle (release of a neutron). The ^{238}U and ^{232}Th decay series are the dominant alpha sources in the natural environment.

For the ^{7}Li(α,p) ^{10}Be reaction to be effective, the lithium atoms must be in the vicinity of uranium- or thorium-bearing minerals, and the size of these minerals should be in the order of about 10 microns. For the ^{23}Na(α,n) ^{26}Al reaction, the calculated cross-sections are close to two orders of magnitude larger than those for the ^{10}Be reaction. Therefore, the non-cosmogenic production of ^{10}Be is considered to be much less important than that of ^{26}Al, which will be considered in detail. According to the calculation of Sharma and Middleton (1989), however, both sodium and a source of alpha emitters such as U-Th-containing mineral phases in close vicinity are required for a potential non-cosmogenic production of ^{26}Al. To evaluate this production pathway, a simple, semi-quantitative pilot study was performed. The samples were selected based on the occurrence of elevated ^{26}Al/^{10}Be ratios, i.e. where a possible excess of ^{26}Al could have been the cause (Tro16, Tro25, Ber17, Ber36, Gla1). By chance, samples with generally high nuclide concentrations such as Feu37 but a normal ^{26}Al/^{10}Be ratio (thus below today's production ratio of 6.8) were also included in the dataset.

The measurements of the samples for uranium, thorium, and sodium were performed on the same sample solutions as for the total Al concentration measurement by ICP-MS using the standard-bracketing method (Tab. E-1). As the samples were prepared and diluted for an ideal determination of ^{27}Al, the determination of uranium and sodium content might have been less appropriate due to matrix effects of the solution liquid, etc. However, the aim was to generally identify whether there was any significantly elevated content of uranium and sodium compared to other samples without elevated ^{26}Al/^{10}Be ratios. The standard solution for the measurement was a 10 ppb uranium solution. It was assumed that uranium and thorium would have the same sensitivity for the ICP-MS measurement (signal intensity per unit concentration in the analysed solution), which is correct to within an order of magnitude. The measurements revealed that uranium and thorium are at least two orders of magnitude less abundant than Al. When total Al was determined to be within 10 to 100 ppm, then the uranium and thorium content was measured to be lower than < 0.2 and < 0.6 ppm, respectively. Therefore, the source of alpha emitters is not abundant at all. The sodium content could not be measured due to the high ^{23}Na background of the blank solution. From four samples, three were already below the Na detection limit, which was the reason why the measurements were not continued, and the Na concentrations could not be determined. In addition, the chemical treatment of the samples may have affected the uranium, thorium and sodium in the samples. To what extent – if at all – is still a matter of investigation.

In Tab. E-1, the resulting non-cosmogenic ^{26}Al concentrations are calculated for the two scenarios of 1'000 ppm (0.01 %) and 100'000 ppm ^{23}Na (1 %) in a quartz sample, using the reference values presented by Sharma & Middleton (1989).

For the very optimistic scenario of having 0.01 % (1'000 ppm) sodium in the quartz grain, specific non-cosmogenically produced ^{26}Al concentrations in the range of a maximum of several 1'000 at/g are calculated. At the most, the calculated values account for half of the lowest 1σ uncertainties of 10'000 at/g measured for the samples (e.g. Tro40) and are therefore considered to be negligible. In contrast, the non-cosmogenic ^{26}Al concentrations for a hundred times higher sodium concentration of 100'000 ppm (1 %) are significant with maximum values of ~ 500'000 at/g non-cosmogenic ^{26}Al. These values are calculated only for samples that do not show an elevated ratio. For the Ber17 and Ber36 samples, a non-cosmogenic ^{26}Al concentration was calculated in the order of a few 1'000 at/g ^{26}Al. For the Gla1 sample, the calculated non-cosmogenic ^{26}Al concentration is twice as high as the measured one. Obviously, despite missing sodium measurements, it can be argued that the non-cosmogenic production of ^{26}Al does not play a significant role due to the missing alpha sources.

According to D. Granger (pers. comm.), non-cosmogenic production does not seem to be a problem for quartz but rather more, for example, for volcanic ash, where the glass could contain disseminated U and Na. Intensive cleaning of samples might help to get rid of superficially adsorbed ^{26}Al coming from a uranium-bearing mineral phase in case leaching occurred during weathering.

In summary, non-cosmogenic ^{26}Al is most likely not a problem for Alpine samples, which are mostly vein quartzes and quartzites, and consist only to a lesser degree of granite with U-Th-bearing mineral phases.

Tab. E-1: Measurements for uranium and thorium of specific samples where previously elevated $^{26}Al/^{10}Be$ ratios were measured (e.g. Tro16 and Tro25)

The measured concentrations were back-calculated through the two major dilution steps (compare with the Std-addition method for Al determination above). Obviously, the required alpha sources uranium and thorium are very rare. Two scenarios for ^{23}Na were considered to either have 100 or 100'000 ppm incorporated to serve as target nuclei for the alpha particles.

Sample name	**$^{26}Al/^{10}Be$ ratio** [-]	**U content (ppb) ICP**	**Th content (ppb) ICP**	**Content in quartz sample**		**Non-cosmogenic ^{26}Al** [at/g]	
				U [ppm]	**Th** [ppm]	**^{23}Na 100 ppm**	**^{23}Na 10'000 ppm**
Ber17	31.7	0.001	0.007	0.000	0.005	48	4'782
Ber35	6.3	0.054	0.062	0.174	0.201	3'439	343'903
Ber36	16.9	0.000	0.001	0.000	0.003	25	2'486
Ibe53	7.0	0.008	0.010	0.042	0.052	857	85'734
Tro16	5.4	0.006	0.009	0.020	0.032	467	46'671
Tro25	5.3	0.000	0.000	0.000	0.000	-1	-50
Tro27	5.3	0.008	0.012	0.020	0.031	463	46'265
Tro40	4.3	0.012	0.139	0.048	0.543	5'149	514'932
Feu16	5.8	0.113	0.242	0.206	0.442	5'830	582'963
Feu21	9.1	0.009	0.039	0.007	0.031	339	33'888
Feu26	6.8	0.000	0.001	0.000	0.001	8	831
Feu37	4.2	0.002	0.004	0.007	0.017	218	21'847
FeuVC	4.1	0.002	0.010	0.001	0.006	59	5'873
Gla1	14.8	0.015	0.044	0.061	0.176	2'117	211'698